ABSTRACT

Title of Dissertation:	EXPLORING MOLECULES IN EXTREME ENERGY STATES: COLLISIONAL RELAXATION AND PHOTODISSOCIATION OF ACTIVATED MOLECULES
	Paul Brandon Diss, Doctor of Philosophy, 2020
Dissertation directed by:	Professor Amy S. Mullin, Department of Chemistry and Biochemistry

This dissertation presents studies that explore how molecules behave when prepared in extreme energy states. A new state-resolved high-resolution transient IR absorption spectrometer paired with a tunable UV excitation source was constructed for the majority of the work.

In the first study, collisional deactivation of pyrazine (E_{vib}=37900 cm^{-1}) with NH$_3$ is characterized with a full state distribution of NH$_3$(0000) products. NH$_3$-pyrazine collisions are found to have modest energy gains with T_{trans}=400–650 K and T_{rot}=480±80 K. There is a limit on V-RT energy gain with T_{trans} decreasing as E_{rot} of the NH$_3$ product increases which suggests impulsive collisions for the V-RT energy pathway. The total appearance rate constant of NH$_3$(0000) is half the collision rate constant showing that there is significant contribution from the V-V energy pathway.

The second study investigates strong CO$_2$-collidine (E_{vib}=39100 cm^{-1}) collisions. The distribution of CO$_2$(J =58-78) are reported and compared to other

methylpyridines. While the state density of 2,6-lutidine is three orders of magnitude lower than 2,4,6-collidine, they have similar J-dependent translational temperatures and the rotational temperatures are within error. Integrated rate constants for $CO_2(J=60\text{-}78)$ increase as a function of donor molecule size. The integrated rate constant more than doubles from 2,6-lutidine to 2,4,6-collidine. Donor size decreases the energy transferred per collision but increases the probability of collisional energy transfer.

For last study, tunable UV excitation ($\lambda=212\text{-}220$ nm) is used to investigate the photodissociation mechanism of SO_2 from the $\widetilde{C}$ state. Measurement of the SO products yield rotational distributions, energy partitioning, quantum yields, and action spectra. $SO(v=0)$ products show an average 4 times more translation than rotation. $SO(v=1)$ product branching ratio was 2% of the total SO products and showed a similar preference for translation. There are equal populations of the three F manifolds across the entire range of UV excitation. Preference for translational energy in the $SO(v=0)$ and $SO(v=1)$ products, low $SO(v=1)$ population, and equal F manifold population indicate SO_2 dissociates via coupling to a repulsive triplet state near threshold.

EXPLORING MOLECULES IN EXTREME ENERGY STATES: COLLISIONAL
RELAXATION AND PHOTODISSOCIATION OF ACTIVATED MOLECULES

by

Paul Brandon Diss

Dissertation submitted to the Faculty of the Graduate School of the
University of Maryland, College Park, in partial fulfillment
of the requirements for the degree of
Doctor of Philosophy
2020

Advisory Committee:
  Professor Amy S. Mullin, Chair
  Professor Millard H. Alexander
  Professor Leah G. Dodson
  Professor John T. Fourkas
  Professor Steven L. Rolston

Acknowledgements

I want to start by thanking my advisor, Dr. Amy Mullin. She has been an invaluable resource and has always pushed me to be a better scientist. Her energy and passion for research are contagious. Her guidance throughout has prepared me to be a scientist and educator moving forward. I would also like to the thank the members of my committee Dr. John Fourkas, Dr. Millard Alexander, Dr. Leah Dodson, and Dr. Steven Rolston for their time in providing me insight and feedback on my thesis.

I would like to thank my first mentor in graduate school, Dr. Alice Mignerey. She has supported me throughout and has helped me become a better teacher. Dr. Joseph Houck and Dr. Elizabeth Griffith were both wonderful in mentoring and fostering my instructional abilities.

My friends and coworkers have been an invaluable resource over the course of my graduate career. Dr. Hannah Ogden and I started graduate school together and we faced the challenges and milestones of the program at the same time. From the first week of classes until the conclusion of our time in the program, she has been a source of steadiness and support that is hard to put into words. Christopher Bognar and Henry Danchi were with me as I started research, and I am grateful to them for the knowledge they imparted to me. Tara Michael has helped me with thoughtful feedback and discussions throughout our time together in the Mullin group. Christopher Lukowski has been an incredible lab partner and supported me through the final projects of my work. From his first year, he has been instrumental in the accomplishments presented in this thesis. I would also like to thank former Mullin group members Dr. Matthew

Murray and Andrew Pommersheim for their thoughtful discussions and help during my first research years.

Lastly, I would like to thank my family. Their love, understanding, and support throughout have enabled my success.

Table of Contents

List of Tables

List of Figures

light (λ = 212 to 220 nm). The IR diode laser probed nascent SO states with IR overtone absorption.

List of Abbreviations

IR	Infrared
UV	Ultraviolet
V-V	Vibration to vibration
V-RT	Vibration to rotation/translation
Nd:YAG	Neodymium-doped yttrium-aluminum garnet
CW	Continuous wave
OPO	Optical parametric oscillator
BBO	β-barium borate
FWHM	Full width at half maximum
PPLN	Periodically poled lithium niobate
COM	Center-of-mass
LJ	Lennard-Jones
REMPI	Resonance-enhanced multiphoton ionization
LIF	Laser-induced fluorescence
UVA	Ultraviolet Absorption
KCSI	Kinetically controlled selective ionization
MIF	Mass-independent fractionation
PES	Potential energy surface
MRCI	Multireference configuration interactions

Chapter 1: Introduction

Molecules with enough internal energy to break chemical bonds are at the heart of how chemistry occurs. These "activated" molecules may either go on to do chemistry, break apart, or lose their energy through collisional deactivation. High energy molecules are found in many environments such as combustion engines, plasmas, reactors, and some exoplanet atmospheres. The three studies presented here are designed to describe where a molecule's energy goes after it is prepared in an extreme energy state. The state-resolved high-resolution transient IR absorption spectroscopy technique used for the studies presented in this thesis enables one to determine how internal energy evolves into vibration, rotation, and translation of the products.

Chapters 3 and 4 investigate how energy is transferred through collisions from vibrationally hot molecules to smaller thermal molecules. Molecules with extreme amounts of vibrational energy are prepared with pulsed UV light and the nascent product distributions of the scattered molecules are measured with transient IR absorption spectroscopy. These studies explore how energy is transferred from vibrationally hot molecules to smaller thermal molecules.

In Chapter 5, the energy-dependent UV photodissociation of sulfur dioxide (SO_2) is investigated. Product state distributions of SO are measured to determine how the excited state energy was used to break a chemical bond. Tunable UV excitation allows the opportunity to probe different areas on the parent molecule potential energy surface and determine how this surface affects photoproduct branching ratios and energy distributions.

1.1 Collision Dynamics

The only way chemistry may occur between two species in a system is through collision. However, many molecular collisions result in no reaction and instead involve a transfer of energy. Even when molecules are activated and have enough energy to break chemical bonds, they may lose energy through deactivating collisions. This thesis describes two collisional energy transfer studies to investigate how collisional deactivation occurs. The first study examines how the identity of the deactivating molecule, or quencher, affects the efficiency of deactivation and the nature of the energy transfer. The second study examines how different donor molecules with approximately the same vibrational energy affect strong collisions and how structure and state density of the donor molecules affect the distribution of scattered quencher molecules.

The Lindemann-Hinshelwood mechanism breaks a unimolecular reaction into two elementary steps.[1] In the first step, two molecules collide, and energy is transferred thereby activating one of them. In the second step, the activated molecule forms products. The first process, collisional energy transfer, is reversible and therefore the deactivation of the excited molecule competes with the formation of chemical products. There are two limits in how collisions can deactivate an excited molecule: "strong" collisions completely deactivate the excited molecule and "weak" collisions have low amounts of energy transfer per collision.[2,3] Experimental studies show these to be an incomplete description of collision dynamics and that in reality, the deactivation process is best described by an energy transfer distribution function.[4–8]

Aromatic molecules are used for the collision studies in this thesis because they can be excited to energies need to break chemical bonds with pulsed UV light. For these

studies, pyrazine ($C_4H_4N_2$) and methylated pyridines ($C_5H_{5-x}N(CH_3)_x$) are electronically excited with λ=266 nm light. The molecules then undergo radiationless decay to the electronic ground where they have E_{vib}= 37900–39100 cm^{-1} of energy. The nonradiative relaxation to the vibrationally hot electronic ground state occurs with quantum yields that are near unity and the lifetimes of the vibrationally excited states are 1-2 orders of magnitude larger than the collisional relaxation and IR probe timescales.[9,10]

1.1.2 Effects of Changing the Identity of the Energy Acceptor

Broadly, collisional energy transfer studies fit into two categories; they either study the energy lost by the vibrationally hot species or they determine how much energy the acceptor molecule has gained. From the first category, it is found that the average energy lost by the donor generally increases as the acceptor molecule size increases. This property has been measured by multiple methods that characterize the overall energy loss process including trajectory calculations, master equation methods, IR fluorescence measurements, and UV absorption.[4,11–15]

Many experimental techniques are not able to capture both the vibration-vibration (V-V) and the vibration-rotation/translation (V-RT) pathways or cannot characterize the distributions strong and weak collisions. The state-resolved transient IR absorption probe technique used in this work allows for the determination of the full state distribution of the scattered molecules in the single collision regime. In Chapter 3, studies are reported that investigate how ammonia (NH_3) deactivates highly vibrationally excited pyrazine (E_{vib}= 37900 cm^{-1}) are reported. The results are compared to measurements from other techniques and from previous state-resolved studies with CO_2 and DCl as the quencher molecules.[7]

1.1.3 Effects of Changing the Identity of the Energy Donor

Intermolecular attractions during collisions are key to understanding how vibrational energy is transferred. Pyridine and methylated pyridines have been observed to form van der Waals complexes with CO_2, with the carbon (C) from CO_2 interacting the nitrogen (N) on the ring of the pyridine.[16,17] Changes in the donor molecule will affect the resulting distribution of CO_2 molecule. Many factors will influence how energy is transferred through collisions. With the same internal energy, adding methyl groups will increase the state density and decrease the average energy per mode. However, the addition of methyl groups also changes the intermolecular interactions because of steric hinderance.[18]

Several previous state-revolved IR probe experiments have examined the effects of state density and donor structure have on the CO_2 collision product distributions. A comparison study of vibrationally hot ($E_{vib} \sim 38000$ cm^{-1}) pyridine, 2-picoline, and 2,6-lutidine found successive methylation reduces the amount of translational and rotational energy imparted to the CO_2. Despite this, the overall cross section of high-J molecules increases with successive methylation, meaning strong collisions are more likely but less energy is transferred per collision.[19,20] Tunable UV excitation studies of CO_2-pyrazine (E_{vib}=37200-40140 cm^{-1}) collisions show little difference in translational or rotational energy gained, but an order of magnitude increase in the cross section of high-J CO_2 products.[21] Chapter 4 will present results of CO_2 products scattered from collisions with vibrationally hot 2,4,6-trimethylpyridine (collidine) to investigate how structure and state density affect strong molecular collisions.

1.2 Photodissociation

The UV photodissociation of sulfur dioxide (SO_2) has been the subject of many studies for decades due to its highly structured UV absorption bands and the unusual nature of its electronic $\widetilde{C}$ state. Recently, the discovery of unusual sulfur isotope amounts in the early earth rock record has led to a renewed interest in the photodissociation of SO_2. It has been proposed that SO_2 photodissociation has contributed to the anomalous isotope fractionation.

The $SO_2(\widetilde{C})$ state absorption is observed at λ=165-240 nm with discrete vibronic bands and the predissociation threshold near λ=220 nm is characterized by a sharp drop in fluorescence relaxation.[22–25] Predissociation of the $SO_2(\widetilde{C})$ state occurs via long-lived metastable state with wavelength-dependent lifetimes. Near threshold it is reported as 45 ns. The products of the predissociation have energy distributions reflective of the vibrational structure of the metastable state and anisotropy on the potential energy surface. It is clear from previous studies that the SO_2 dissociation mechanism evolves with photoexcitation wavelength. Recent theoretical studies have been done to more accurately map the predissociative $SO_2(\widetilde{C})$ state using modern computation techniques.[26–29]

In Chapter 5, state-resolved high-resolution transient IR absorption spectroscopy is used to probe the nascent SO product photofragments as a function of UV photolysis wavelength. The full distribution of photofragment product energies are measured near the photodissociation threshold (E_{prod}<1900 cm^{-1}) to help elucidate the dynamics of the predissociative $SO_2(\widetilde{C})$ state.

5

1.3 Outline

The thesis is arranged in the following order:

- Chapter 2: This chapter describes both the instrumental and IR absorption spectroscopy aspects of the experiments presented here. A a new state-resolved high-resolution transient IR absorption spectrometer was constructed and used for the majority of the work in this thesis.

- Chapter 3: This chapter investigates how NH_3 deactivates highly vibrationally excited pyrazine (E_{vib}=37900 cm^{-1}). These results are compared to previous work to determine how symmetry, mass, and dipole of the quench molecule affect collisional energy transfer. NH_3 shows J-dependent translational energy gaines and moderate rotational energy gains. Comparison of absolute rates show a significant portion of NH_3 scattered into vibrationally excited states.

- Chapter 4: This chapter studies how state density and structure of vibrationally hot molecules affect energy transfer in strong collisions. Vibrationally hot 2,4,6-collidine is deactivated by collisions with CO_2. The resulting $CO_2(J \geq 58)$ rotational state distributions are compared to results with other donor molecules. Increased methylation around the interaction site lowers the translational and rotational energy gain and increased state density of the donor raises the total high-J collision cross section.

- Chapter 5: This chapter presents work that explores the energy-dependence of SO_2 photodissociation near threshold using tunable UV photoexcitation. Nascent product distributions, branching ratios, and the SO(v=1) onset are reported. The fraction of SO product energy in rotation was generally independent of excitation energy except one photolysis wavelength where there was a marked increase in translational energy of the SO diradical photoproducts.

- Chapter 6: This chapter presents conclusions and summarizes the main results found in this thesis in addition to possible future studies.

- Appendix A: This appendix details how Lennard-Jones collision rate constants used in Chapters 3 and 4 were calculated and the parameters for the molecules discussed.

- Appendix B: This appendix describes how the thermal vibrational energy for selected aromatic molecules were calculated. The vibrational energies of the excited molecules and the mode frequencies were used to calculate the average energy per vibrational mode for pyridine, lutidine, picoline, and collidine.

- Appendix C: This appendix contains supporting information for Chapter 5. Calculation details for the SO(2←0) spectral line intensities and Einstein A coefficients are given. Transitions frequencies for SO(2←0) are reported up to N=40.

Chapter 2: Experimental Methods

This chapter describes the instrumentation used to conduct the studies presented in this thesis. A major component of the research involved the construction a new high-resolution transient IR absorption spectrometer for the experiments in Chapters 4 and 5. The research spans two categories of investigation of molecular processes in the gas phase: the collisional energy transfer dynamics of vibrationally hot molecules and the photodissociation dynamics of molecules excited to metastable states. The experiments use a type of pump-probe spectroscopy to initiate the processes under investigation and detect the nascent product state distributions. Pulsed UV light is used to electronically excite molecules and prepare them in either extreme vibrational states or predissociative states. In Chapters 3 and 4, aromatic molecules are prepared in vibrationally hot states and the energy is transferred via collisions to a quenching molecule. The work in Chapter 5 explores how molecules dissociate after vibronic excitation to metastable states. State-resolved high-resolution transient IR absorption spectroscopy is used to probe the products of collisions or dissociation.

The studies in this thesis share a common experimental approach that is shown schematically in Figure 2.1. The UV light pulse in each study is generated from a manipulated Nd:YAG laser pulse. The continuous-wave (CW) IR light sources are high-resolution and tunable with IR wavelength controlled with active feedback. The UV and IR beams are overlapped spatially with a dichroic mirror and guided through a 3 m Pyrex sample cell with CaF_2 windows. The UV light is removed after the cell with a second dichroic mirror and the transmitted IR light is collected for detection and signal analysis.
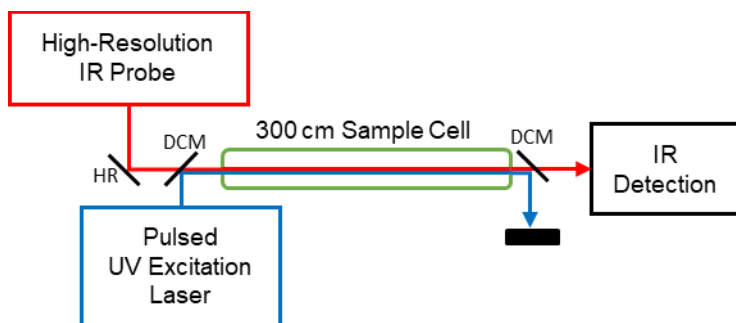
Figure 2.1 A schematic diagram of the pump-probe technique used in these studies. A pulsed UV excitation beam and high-resolution CW IR probe beam are propagated collinearly through a 3 m flowing gas cell. The transmitted IR light is collected for transient absorption measurements.

2.1 Generation of UV Excitation Pulses

Two methods were used to generate the requisite light for the experiments described here. Both methods use pulsed Nd:YAG lasers (Continuum Lasers) with a repetition rate of 10 Hz. For the first method, 1064 nm light is frequency-doubled twice to generate output at 266 nm. The fourth-harmonic light was used to prepare highly vibrationally excited pyrazine molecules to investigate collisional energy transfer dynamics with ammonia. This process is summarized in Fig. 2.2a.
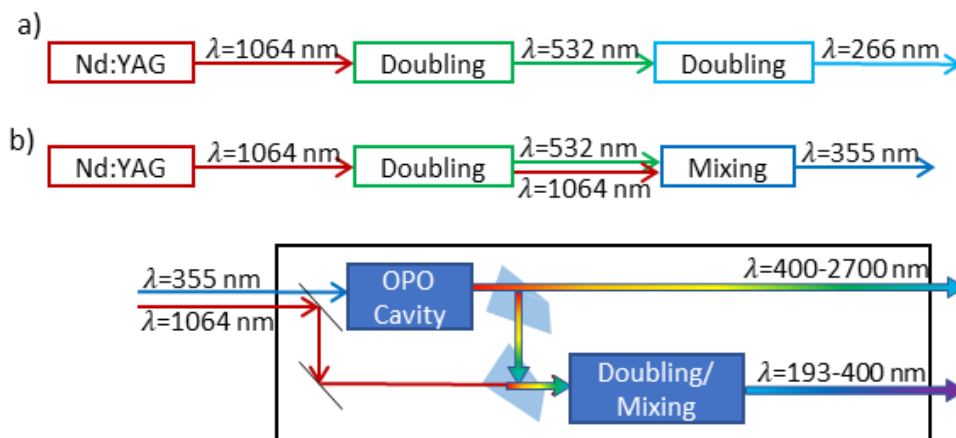
Figure 2.2 (a) $\lambda = 266$ nm light is generated by frequency-doubling the output of an Nd:YAG laser twice. (b) Tunable UV light is generated with the third harmonic of an Nd:YAG, which pumps an OPO and a set of frequency-doubling/mixing crystals.

9

For the $\lambda = 266$ nm and $\lambda = 212$ to 224 nm light used for Chapters 4 and 5 respectively, the Nd:YAG laser was used to pump a pulsed optical parametric oscillator (OPO) (Horizon, Continuum Lasers). A schematic diagram of the pulsed UV OPO is presented in Fig. 2.2b. The 1064 nm light from the Nd:YAG laser is doubled to $\lambda = 532$ nm. Residual 1064 nm is mixed with 532 nm photons to give $\lambda = 355$ nm. The $\lambda = 355$ nm photons are guided into the OPO cavity where they are converted to two lower-energy photons by a pair of β-barium borate (BBO) crystals to maximize conversion efficiency and output spatial stability. The output of the OPO is tunable and comprised of a visible beam and a near-IR beam. UV light is generated by doubling the visible OPO output and mixing the doubled light with the residual 1064 nm light from the Nd:YAG laser. The output of the Nd:YAG-pumped OPO is linearly polarized with an energy resolution of 10 cm^{-1} and a time resolution of 10 ns for the wavelengths used.

The wavelength of the OPO output was calibrated using an Ocean Optics spectrometer and known absorption spectra of gas-phase molecules. Benzene absorption was used for $\lambda{\sim}266$ nm calibration and SO_2 absorption was used for $\lambda = 212$ to 224 nm calibration.

2.2 High-Resolution IR Probe Sources

Two types of IR light sources were used to probe rovibrational transitions of the gas molecules studied: a fiber laser pumped CW mid-IR OPO and a Pb-salt diode laser. Both IR sources have a spectral resolution that is at least 10 times narrower than the full width at half maximum (FWHM) of IR spectral lines at 296 K for the molecules probed in these studies, such that $\delta \nu_{IR} \leq 0.1 \Delta \nu_{296\,K}$. In Chapter 3, ammonia (NH_3) is probed with

the mid-IR OPO (Lockheed-Martin). In Chapters 4 and 5, carbon dioxide (CO_2) and sulfur

monoxide diradicals (SO) are probed using the liquid nitrogen cooled Pb-salt diode laser

(Laser Components). The characteristics of the two light sources are summarized in Table

2.1. Both sources are wavelength modulated to allow for fine wavelength control through

active feedback locking.

Table 2.1 A Comparison of the IR Probe Sources

	Mid-IR OPO	IR Diode Laser
Modulation Frequency	100 Hz	1 kHz
Modulation Source	External	Internal
Output Wavelength	2.5-3.2 μm	4.3-4.5 μm
Output Power	1-5 W	200 μW
Spectral Resolution	$3 \cdot 10^{-5}$ cm^{-1}	$3 \cdot 10^{-4}$ cm^{-1}

The mid-IR CW light from the OPO is generated by a fiber amplifier pumping a

periodically poled lithium niobate (PPLN) crystal. The output has tunable wavelength of

2.5-3.2 μm and a spectral resolution of $\delta\nu_{IR} = 3 \cdot 10^{-5}$ cm^{-1}. The mid-IR OPO wavelength

is modulated externally at 100 Hz. The Pb-salt diode laser is a semi-conductor laser with

tunable output of 4.3-4.5 μm and a spectral resolution of $\delta\nu_{IR} = 3 \cdot 10^{-4}$ cm^{-1}. The diode

laser wavelength is internally modulated at 1 kHz.

The firing of the Nd:YAG laser is synchronized to the IR modulation so that

transient IR absorption measurements are collected at the center of the modulation cycle.

The synchronization is accomplished by triggering the Nd:YAG Q-switch with a 10 Hz

pulse train derived from the IR modulation. A variable time-delay is used to center the UV

pulse with respect to the IR modulation. A timing diagram is shown in Fig. 2.3.
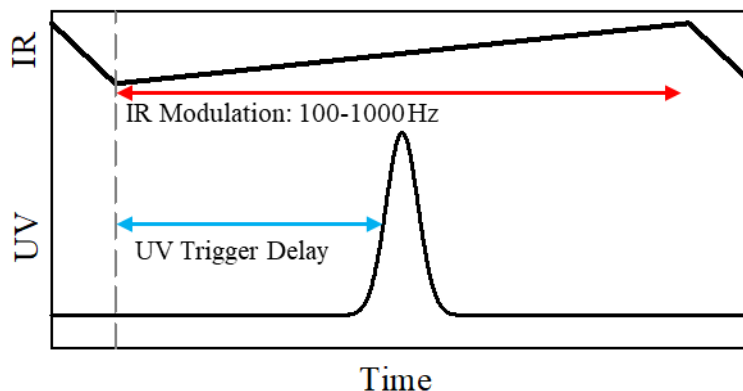
Figure 2.3 The Nd:YAG Q-switch firing at 10 Hz is synchronized to the IR modulation. A time delay is used to center the UV pulse in the IR modulation cycle.

2.3 Infrared Detection Scheme

High-resolution transient IR absorption spectroscopy is used to detect the outcome of collisions or photodissociation. The IR light is guided to three paths, each ending with an indium-antimonide (InSb) detector. Before the sample cell, approximately ~5% of the light is used for a reference cell and an addition ~5% is used for a tunable Fabry-Perot etalon. The majority of the IR light passes through the sample cell collinearly with the UV pump beam. A pair of dichroic mirrors is used to spatially overlap the UV and IR beams through the cell and then separate the two beams after the cell. The InSb detectors (Teledyne-Judson) operate with a p-n junction and have linear response for mid-IR light. Each detector is paired with a matched amplifier (Perry Amplifier). The combined gives a response time between 100 and 300 ns.

After the sample cell, the UV light is deflected and the IR beam passes through a monochromator (Laser Photonics) and onto a sample detector. The monochromator is used

to ensure that a single IR wavelength reaches the sample detector and that stray UV light is removed. A saturation cell is also used to ensure wavelength purity of the IR probe light.

Fine IR wavelength control is attained through an active feedback loop. Light transmitted through the reference gas cell or the tunable Fabray-Perot etalon is collected with an InSb detector and the output voltage is the input to a lock-in amplifier. The IR modulation frequency is the reference source for the lock-in amplifier. The error signal is fed back to the IR light source to maintain a constant IR wavelength. This setup allows the spectrometer to have a stable IR probe wavelength over the course of the experiment.
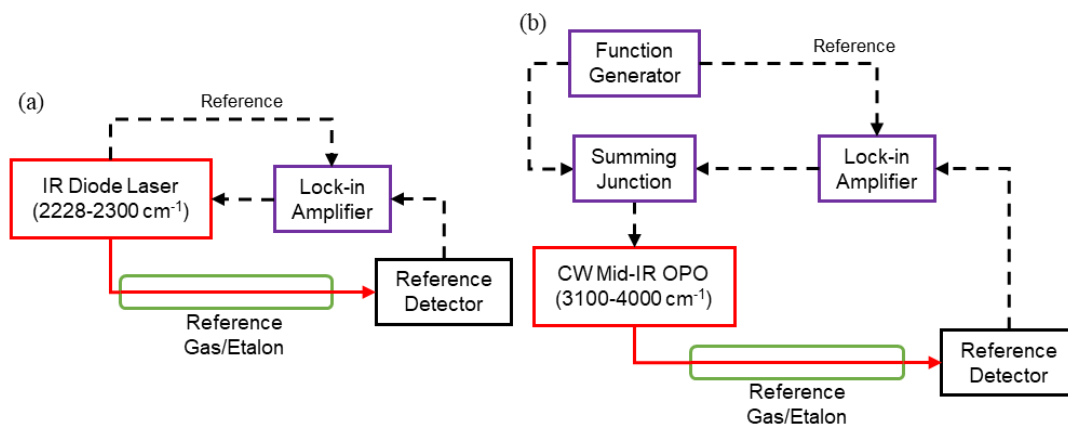
Figure 2.4 Active feedback locking schemes for (a) the Pb-salt diode laser and (b) the mid-IR OPO.

For controlled scanning, the IR wavelength is locked to the fringe of a tunable Fabry-Perot etalon. The length of the etalon cavity is varied by tuning the angle of a CaF_2 window inside the cavity. As the pathlength changes, the IR light is adjusted by the error signal from the lock-in amplifier to maintain the integral wavelength requirement of the etalon cavity. Transient Doppler-broadened line profiles are measured by collecting transient absorption signals at discrete IR wavelengths across a spectral absorption transition feature.

2.4 Flowing Gas System

A flowing-gas vacuum system was constructed as part of the transient IR absorption spectrometer. The flowing-gas system was built to accommodate one or two gases, depending on the type of experiment performed. For collisional energy transfer experiments, the partial pressures of the input gases were maintained with electronic flow controllers (MKS). The bath gases (Matheson: NH_3 99.99%, CO_2 99.99%, SO_2 99.98%) were introduced to the electronic flow controllers from lecture bottles. Pyrazine (Aldrich) and 2,4,6-trimethylpyridine (collidine) (Acros) samples were placed in Pyrex round-bottom flasks and degassed with several freeze-pump-thaw cycles before use. The two input gas lines were combined prior to entering the 3 m Pyrex sample cell. Partial pressures of each gas were maintained at 5 to 10 mTorr.

The SO_2 photodissociation study used a single gas as input and the flow controllers were not used. Instead, a needle valve was used to control the pressure from the lecture bottle of SO_2 to the sample cell. Most of the data for Chapter 5 were collected at a pressure of 20 mTorr.

2.5 Rovibrational Spectroscopy

Nascent population measurements were performed with high-resolution transient IR absorption spectroscopy. The IR probes have sub-Doppler resolution that allows for the measurement of line profiles of individual product states. Table 2.2 lists the 296 K Doppler line widths (FWHM) and the spectral resolution of the IR probe.

Table 2.2 Doppler-Broadened Line Widths at 296 K

Molecule	$\Delta v_{296\,K}$	Probe Resolution
NH_3	$1.0 \cdot 10^{-2}$ cm^{-1}	$3 \cdot 10^{-5}$ cm^{-1}
CO_2	$4.2 \cdot 10^{-3}$ cm^{-1}	$3 \cdot 10^{-4}$ cm^{-1}
SO	$4.0 \cdot 10^{-3}$ cm^{-1}	$3 \cdot 10^{-4}$ cm^{-1}

Rovibrational transitions occur when IR light is resonant with the energy gap between pairs of rovibrational states. Absorption spectroscopy is governed by a selection rule that limits change of angular momentum to $\Delta J = 0, \pm 1$. More detailed descriptions of the probe spectroscopy will be given in the specific chapters. For the work in this thesis, transitions with $\Delta J = -1$ (P-branch) and $\Delta J = +1$ (R-branch) are used. Figure 2.5 shows an example of these transitions for a $CO_2(00^01\leftarrow00^00)$ transition originating in the $J =74$ state.
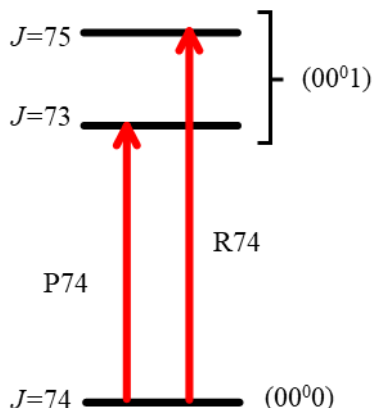
Figure 2.5 Two example P- and R- branch transitions are shown for the $CO_2(00^00, J=74)$ state.

IR transitions are used to probe the nascent populations of individual rovibrational states using the Beer-Lambert Law,

$$I_t = I_0 \, exp(-\alpha p\ell) \qquad\qquad (2.1)$$

Here, I_t is the intensity of transmitted IR light, I_0 is the incident intensity, p is the pressure, ℓ is the path length, and α is the absorption coefficient. The absorption coefficient is a product of the line intensity S_H, line shape factor $f(0)$, and the pressure-independent number density, $N \equiv \frac{n}{VP} = 1/RT$ of the gas under reference conditions of 296 K in units of cm^{-3} Torr^{-1}.

$$\alpha = S_H f(0)N = S_H f(0)/RT \tag{2.2}$$

The line shape factor includes information about the transition width and is important for determining the absolute population in a given state. The Beer-Lambert Law combined with the definition of α gives

$$I_t = I_0 \, exp\left(-S_H f(0)\frac{1}{RT}p\ell\right) \tag{2.3}$$

The units of S_H are cm^2 molec^{-1} cm^{-1} as it is the cross section integrated over the frequency.

For the NH$_3$ and CO$_2$ studies, the S_H values are taken from the HITRAN database.[30,31] Using S_H values in the Beer-Lambert Law for individual IR transitions yields the pressure of the total sample. For state-specific number densities and partial pressures, S_H is divided by the fractional equilibrium population at 296 K for the rotation and vibrational state of interest. Here, the line intensities from HITRAN are denoted by S_H and the state-specific line intensities are denoted as S_J.

$$S_J = \frac{S_H}{f_J \cdot f_v} \tag{2.4}$$

For the SO studies, the values of S_H were determined from the Einstein A coefficients using

$$S_H = I_a \frac{A_{21}}{8\pi c v^2}\frac{g_2}{g_1} \cdot f_J \cdot f_v \cdot \left(1 - exp(-v/k_B T)\right) \tag{2.5}$$

Here, I_a is the isotopic abundance, A_{21} is the Einstein coefficient from state $|1\rangle$ to state $|2\rangle$, c is the speed of light, ν is the frequency of light, g_2 and g_1 are the degeneracies of the upper and lower states, respectively, $f_J \cdot f_v$ is the fraction of molecules in the given ro-vibration state, k_B is the Boltzmann constant, and T is the 296 K reference temperature. The line center intensities are used in conjunction with the Doppler-broadened line profiles to determine absolute number densities for individual quantum states.

2.6 Doppler-Broadened Line Profiles

The translational energy distributions from collisional energy transfer and photodissociation were determined by measuring Doppler-broadened line profiles of individual product states.

Molecules in motion relative to a light source absorb light at a slightly different frequencies based on the Doppler effect. This effect is described by

$$\nu = \nu_0 \left(1 \pm \frac{v}{c} \right) \tag{2.6}$$

where ν is the IR frequency, ν_0 is the IR frequency at line center, v is the velocity component parallel to the IR propagation vector, and c is the speed of light. Molecules with a higher relative speed absorb light further from the line-center transition frequency.

The integrated line intensity, and therefore the total population, must account for the velocity distribution at a given temperature, T. The term $f(0)$ accounts for this area and for Gaussian profiles

$$f(0) = \frac{2}{\Delta \nu_{Dop}} \sqrt{\frac{\ln 2}{\pi}} \tag{2.7}$$

17

Here Δv_{Dop} is the line profile at the FWHM. Two methods are used to determine Doppler widths in this thesis, depending on the process that generates the product states under investigation.

2.6.1 Doppler Profiles from Collisional Energy Transfer

For isotopic distributions of molecular velocities, IR transitions are broadened and have Gaussian line profiles. An equilibrium sample of molecules has a Boltzmann energy distribution

$$P(E)\, dE = A \cdot exp\left(-\frac{E}{k_B T}\right) dE \tag{2.8}$$

Here A is a normalization constant, E is the translational energy, k_B is the Boltzmann constant, and T is the temperature. The corresponding velocity distribution is rewritten in terms of the molecular velocity of the given molecule v is given

$$P_v(v)dv = \sqrt{\frac{m}{2\pi k_B T}}\, e^{\left(\frac{-mv^2}{2k_B T}\right)} dv \tag{2.9}$$

Here m is the mass. The velocity distribution in Equation 2.9 leads to an absorption frequency distribution for a transition. This distribution is

$$P_v(v)dv = \sqrt{\frac{mc^2}{2\pi k_B T v_0^2}} \cdot exp\left(\frac{-mc^2(v-v_0)^2}{2v_0^2\, k_B T}\right) dv \tag{2.10}$$

Here v is the frequency of light and v_0 is the line center IR frequency. Equation 2.10 has the form of a Gaussian with the FWHM line width given

$$\Delta v_{Dop} = \sqrt{\frac{8 ln\, 2\, k_B T}{mc^2}}\, v_0 \tag{2.11}$$

Equation 2.11 is rearranged to yield the translational temperature that describes the translational energy distribution

$$T = \frac{mc^2}{8 \ln\ln 2\, k_B} \left(\frac{\Delta v}{v_0}\right)^2 \qquad\qquad (2.12)$$

2.6.2 Doppler Profiles for Photodissociation Products

In photodissociation, the angular distribution of photofragments and angular velocities in the center-of-mass (COM) frame are often anisotropic which affects the observed line shapes. The analysis of these observed line shapes is based on the work of Zare and Herschbach.[32] For linearly polarized photolysis light, the angular distribution of the fragments in the COM frame is given by

$$W(\theta) = \frac{1}{4\pi}\{1 + \beta P_2(\cos \theta') P_2(\cos \theta)\} \qquad\qquad (2.13)$$

Here θ is the angle between the photolysis polarization and the fragment recoil, θ' is angle between the UV photolysis polarization and the IR probe propagation, β is the anisotropy parameter, and P_2 is the second Legendre polynomial, $P_2(x) = \frac{1}{2}(3x^2 - 1)$. For colinear pump and probe beams, $(\cos \theta')$ reduces to 1 and Equation 2.13 becomes

$$W(\theta) = \frac{1}{4\pi}\{1 + \beta P_2(\cos \theta)\} \qquad\qquad (2.14)$$

The anisotropy parameter has limiting values of β= -1 to 2 corresponding to complete transverse and axial recoil, respectively. An anisotropy value of β=0 is the case for an isotropic distribution.

The angular distribution of photodissociation products have the Doppler profiles in the form of

$$\begin{aligned} F(\xi, \eta) = &\left[1 + \tfrac{1}{2}\left(\tfrac{\beta}{\eta^2}\right)\left(3\xi^2 - \eta^2 + \tfrac{3}{2}\right)\right] \cdot [erf(\xi + \eta) - erf(\xi - \eta)] \\ &+ \tfrac{3}{4}\left(\tfrac{\beta}{\eta^2}\right)\left[(\xi - \eta)\tfrac{2}{\sqrt{\pi}}e^{-(\xi+\eta)^2} - (\xi + \eta)\tfrac{2}{\sqrt{\pi}}e^{-(\xi-\eta)^2}\right] \end{aligned} \qquad (2.15)$$

19

The dimensionless quantities ξ and η are the recoil and laboratory velocities, respectively, divided by the most probable velocity of the parent molecule. For an isotropic distribution, $\beta=0$ and Equation 2.15 reduces to

$$F(\xi,\eta) = A' \cdot [erf(\xi + \eta) - erf(\xi - \eta)] \tag{2.16}$$

Here A' is an intensity scaling parameter at linecenter. The value of η is determined from energy conservation, discussed further in Chapter 5.

2.7 State-specific Number Densities

Static absorption measurements are used to determine the pressure in the collision/photolysis cell. The Beer-Lambert Law is rearranged to

$$p = \frac{-ln\left(I_t/I_0\right)}{\alpha\, l} = \frac{-ln\left(I_t/I_0\right)}{S_H f(0) N \ell} \tag{2.17}$$

State-specific pressures, p_J, are determined using known line intensities, line shape factors, and fractional populations at 296 K.

$$p_J = \frac{-ln\left(I_t/I_0\right)}{S_J f(0) N \ell} = \frac{-ln\left(I_t/I_0\right)}{S_H f(0) N \ell} \cdot f_J \cdot f_v \tag{2.18}$$

State-specific number densities are determined from the ideal gas law such that

$$\frac{N_{Jv}}{V} = \frac{p_J}{RT} = \frac{-ln\left(I_t/I_0\right)}{S_H f(0)\ell} \cdot f_J \cdot f_v \tag{2.19}$$

Here N_{Jv} is the number of molecules in a particular rovibrational state and V is the volume of the sample probed. Equation 2.19 is valid when the sample is at the 296 K reference temperature. To account for line shape factors at other temperatures, Equation 2.19 is multiplied by the ratio of the observed line-width to the Doppler-width. Population

changes that result from collisional energy transfer or photodissociation are determined using fractional transient absorption signals and

$$\frac{N_{Jv}}{V} = \frac{-ln\left(\Delta I/I_0\right)}{S_H f(0)\ell} f_J f_v \frac{\Delta v_{obs}}{\Delta v_{Dop}} \tag{2.20}$$

Chapter 3: Collision Dynamics of Highly Vibrationally Excited Pyrazine(E_{vib}=37900 cm^{-1}) and Ammonia: State-resolved Energy Profiles of NH$_3$(0000, J_K)

3.1 Introduction

Collisional energy transfer and deactivation of hot molecules is ubiquitous in gas-phase chemistry and it impacts overall reaction rates, branching ratios, and energy redistribution. At the heart of energy transfer from an excited molecule is the intermolecular potential energy. Long- and short-range interactions between the collision partners have an effect on how the energy is ultimately distributed in the collision products, depending on the energy transfer mechanism. The structure, energy content, vibrational frequencies, and overall size of the collision partners have major influences on the energy redistribution process.

The Lindeman-Hinshelwood mechanism describes the activation and deactivation of molecules. Historically, the strong collision assumption has been invoked in the absence of detailed information about molecular collisional energy transfer. The strong collision assumption entails that every quenching collision deactivates the excited molecule to a non-reactive state.[1] Collisions classified as "strong" involve large amounts of energy transfer and those that are "weak" transfer small amounts of energy.[2,33] Beyond these limiting cases, energy transfer distribution functions P(ΔE) are better descriptions of the relaxation process, and are now accessible with experiment and theory.

Collision dynamics studies generally fall into one of two categories: measurement of energy lost from the vibrationally hot molecule or measurement of the energy gained by the bath molecule. Donor relaxation methods such as IR fluorescence (IRF) and UV

absorption (UVA) provide information about the average energy transfer and in some cases the energy transfer distribution function. In the second type of study, energy gain in the bath molecule is measured using state- and time-resolved techniques.[6,7,34] The research in this chapter falls in the second category and uses transient IR absorption spectroscopy to investigate the state-resolved energy gain distributions in NH_3 in order to identify the mechanisms by which it shows enhanced quenching efficiencies with vibrationally excited pyrazine.

Investigations into energy lost from activated molecules show that for a given donor, the energy transfer efficiency generally increases as a function of the size and complexity of the energy-accepting bath molecule.[14,15,35] In some cases, enhanced energy transfer efficiencies are observed for polar bath molecules such as H_2O and NH_3. Miller and Barker, using IRF in combination with master-equation analysis, found that NH_3 deactivates pyrazine($E_{vib} = 24000$ cm^{-1}) with average energy transfer values that are almost a factor of three larger than similarly sized bath molecules, such as CH_4 and CO_2.[4] UVA measurements from Hippler et al[36] have shown similar enhancement for H_2O compared to N_2O and CO_2 as collision partners with hot toluene ($E_{vib} = 52000$ cm^{-1}). However, Hippler et al[3] also find this enhancement is not as pronounced for hot azulene ($E_{vib} = 30600$ cm^{-1}) with NH_3, CO_2, and H_2O, which all show moderate average energy transfer values.

The collisional deactivation of pyrazine has been studied for several energy-accepting bath molecules with state-resolved measurements of the nascent energy distributions of the acceptor molecules.[6–8,34,37,38] Carbon dioxide deactivates vibrationally hot pyrazine ($E_{vib} = 32700$-37900 cm^{-1}) and a bimodal CO_2 rotational distribution is observed with temperatures of $T_{rot} = 1145$ K and $T_{rot} = 437$ K associated with strong and

23

weak collision pathways, respectively.[7] For the case of the strong collisions, the product translational energy increases sharply as a function of the CO_2 rotation quantum number. Simulations show that the strong collision pathway involves chattering collisions wherein there are multiple, sequential contacts between the two molecules during the collision. For DCl, scattered molecules are rotationally hot (T_{rot}=880 K), with recoil velocities that also increase with rotational state.[34] When water (HOD) is the bath molecule, collisions with hot pyrazine result in scattered water molecules with moderate rotational energy gain (T_{rot}=430 K) and recoil energies that are relatively small and independent of rotational state.[6] For CO_2, DCl, and HOD as pyrazine quenching molecules, the primary relaxation pathway involves vibration-to-rotation/translation (V-RT) energy transfer and collisions leading to vibrational excitation of the bath molecule through vibration-to-vibration (V-V) energy transfer account for approximately 10-15% of all collisions.

From studies of van der Waals complexes we get information about interaction potentials and geometries of pyrazine with other molecules. Complexes of CO_2 with pyrazine have a T-shaped structure, with the C atom of CO_2 interacting with the N on pyrazine and the CO_2 molecular axis perpendicular to the aromatic ring.[16,39] In the case of ammonia and pyrazine, the H atom on NH_3 interacts with the N on pyrazine through hydrogen bonding interactions.[40,41]

With our state-resolved IR probe, we determine the energy distributions of the bath molecule scattered from collisions with vibrationally hot pyrazine. Measuring multiple states, we determine the total probability of energy transfer over all rotational states. This approach gives us the ability to compare our results from probing the bath molecules with measurements of energy lost by the donor. Here, we detail how pyrazine is deactivated

through collisions with NH_3 through V-RT energy transfer. We probe the nascent rotational states with $J = 0$ to 11 of the ground vibrationless state of $NH_3(0000)$ to determine the energy gain profiles using high-resolution transient IR absorption spectroscopy. The collection of the nascent population distribution allows us to quantify the rotational and translational energy gained by NH_3 from single collisions with pyrazine and the probability distribution of the energy transferred.

3.2 Experimental

A mid-IR optical parametric oscillator (OPO) was used for transient IR measurements of scattered NH_3 molecules at λ=2.9 μm following collisions with highly vibrationally excited pyrazine. The OPO-based high-resolution transient IR absorption spectrometer is described in detail in Chapter 2 and previous studies;[42] the key features are presented here. Figure 3.1 shows a schematic diagram of the high-resolution transient IR absorption spectrometer.

A 2:3 mixture of pyrazine:NH_3 vapors at a total pressure of 25 mTorr was maintained in a 3 m flowing-gas cell. Anhydrous NH_3 (Matheson, 99.99%) was used directly and pyrazine (Aldrich, 99%+) was degassed by several freeze-pump-thaw cycles prior to use.
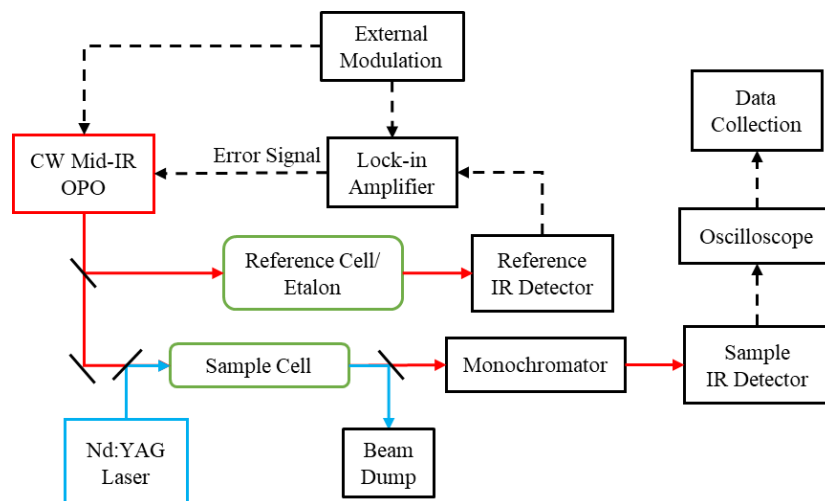
Figure 3.1. A schematic diagram of the transient absorption spectrometer. Part of the IR probe beam is passed through a reference gas cell of Fabry-Perot scanning etalon to provide wavelength stabilization through active feedback control. The UV and IR beams are overlapped spatially through the sample cell and transmitted IR light is collected on a digital oscilloscope as function of time following the UV pulse.

Highly vibrationally excited pyrazine was prepared using the fourth harmonic of a pulsed Nd:YAG laser ($\lambda = 266$ nm) with a pulse FWHM of 7 ns.

$$Pyr(296 \text{ K}) + h\nu(266 \text{ nm}) \rightarrow Pyr(E_{vib}=37900 \text{ cm}^{-1}) \qquad (3.1)$$
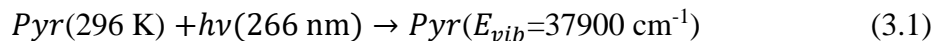
After excitation to the S_2 electronic state, pyrazine undergoes radiationless decay to high vibrational states ($E_{vib}=37900$ cm^{-1}) of the S_0 ground electronic state with a radiationless decay time constant of 50 ns. The UV pulse energy was monitored with a power-meter (Coherent, Inc.) and the power density was kept below 2.5 MW/cm^2 to minimize multiphoton. Approximately 10% of the pyrazine sample was excited under these conditions.

The mid-IR OPO output is high resolution ($\Delta\nu_{OPO} = 3 \cdot 10^{-5}$ cm^{-1} ~1 MHz) compared to Doppler-broadened line profiles of NH$_3$ at 296 K ($\Delta\nu_{Dop} \sim 1 \cdot 10^{-2}$ cm^{-1}) and is broadly tunable around $\lambda = 2.9$ μm, enabling measurements of transient line profiles for

individual rotational states of scattered NH_3.[42] Transmitted IR light is passed through a diffraction grating monochromator and collected with a liquid-nitrogen cooled InSb detector as a function of time following the UV pulse that excited pyrazine.

Active feedback was used to control the wavelength of the IR probe light. The IR optical frequency was modulated at 100 Hz using a piezo-mounted cavity mirror. A portion of the IR light was used as a reference beam that passed through either a 0.3 m NH_3 gas cell or a Fabry-Perot scanning etalon. The transmitted intensity was collected with a second InSb detector and used as input to a lock-in amplifier. The error signal from the lock-in amplifier was fed back to the IR OPO to correct for drifts in IR wavelength. Line-center transient measurements were collected by locking the IR light to the peak of a rovibrational transition using the reference gas cell. Transient line profiles were measured by locking the IR light to the fringe of the scanning etalon and collecting transient IR signals in discrete steps of $\delta v \leq 0.001$ cm^{-1} across the Doppler broadened transition.

The UV pump and IR probe beams were spatially overlapped and propagated collinearly through the sample cell using a pair of dichroic mirrors. Nascent NH_3(0000, J_K) populations were measured at 1 µs following the UV pulse. At 25 mTorr, the average time between collisions is approximately 4 µs.

The rotational states of NH_3 are characterized by the total rotational quantum number J and the projection of J onto the principal rotational axis K. The projection quantum number K is an integer value with $K=0-J$. There are two symmetry-based rotational sublevels. When $K/3$ is an integer, the states are designated as "A"; when $K/3$ is not an integer, they are designated as "E". Rotational states in the A sublevel have twice the degeneracy than those in E.

Quenching collisions of vibrationally hot pyrazine with NH_3 that produce NH_3 in the vibrationless ground state via

$$Pyr(E_{vib}=37900 \text{ cm}^{-1}) + NH_3(296 \text{ K}) \xrightarrow{k_{app}^J} Pyr(E'_{vib}) + NH_3(0000, J_K, vel) \qquad (3.2)$$
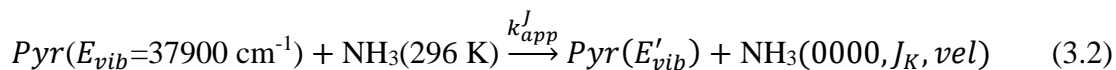
Here, E_{vib} is the pyrazine vibrational energy, k_{app}^J is the product-state-specific rate constant, vel is the NH_3 recoil velocity, $NH_3(0000, J_K, vel)$ is the specific rotational state and Doppler component that is probed, and $Pyz(E'_{vib})$ is the vibrationally excited pyrazine post-collision.

3.3 Results & Discussion

3.3.1 Doppler-Broadened Line Profiles of Scattered NH_3 Molecules

Nascent NH_3 populations of the ground vibrational state following collisions with highly vibrationally excited pyrazine were measured with state-resolved IR probing of NH_3 rotational states $J = 0$ to 11 using one-quantum absorption to either the ν_1 or ν_3 stretching modes near $\lambda = 2.9$ µm:

$$NH_3(0000, J_K, vel) + h\nu(IR) \rightarrow NH_3(1000, J'_K, vel) \text{ or } NH_3(0010, J'_K, vel) \qquad (3.3)$$
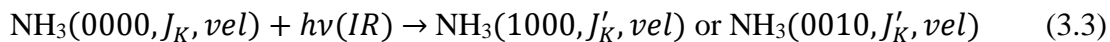
Figure 3.2a shows the transient IR absorption signal for the $J_K=0_0$ state and Figure 3.2b shows the transient IR absorption signal for the $J_K=11_9$ state. Low energy rotational states (J=0-4) of NH_3 have transient line profiles that show population-depletion caused by collisions with vibrationally hot pyrazine. Rotational states with $J = 5$ to 8 have line profiles comprised of both appearance and depletion components. Rotational states with $J = 9$ to 11 have low thermal populations and show transient signals that are only for

28

population appearance, with the exception of the $J_K = 9_9$ state, that has a low enough energy to show a depletion component.
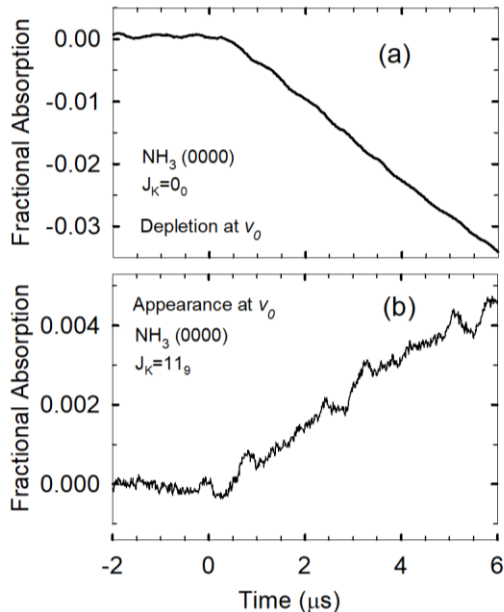
Figure 3.2 Line-center transient IR absorption measurements for $NH_3(0000)$ in two product states. (a) The $J_K = 0_0$ state is depleted upon collisions with vibrationally hot pyrazine. (b) The $J_K = 11_9$ state is populated by collisions with hot pyrazine.

Time-resolved fractional IR absorption signals were fit with a linear regression from $t = 0$ to 4 μs after the UV pulse; the fit value at $t = 1$ μs was used to determine the nascent Doppler-broadened line profiles of individual product states. Line profiles with pure state appearance or depletion were fit to Gaussian functions and states with both components were fit to a sum of two Gaussians. The fit equation is

$$F(v) = I_{app} \exp\left[-4\ln(2)\left(\frac{(v-v_0)}{\Delta v_{app}}\right)^2\right] - I_{dep} exp\left[-4\ln(2)\left(\frac{v-v_0}{\Delta v_{dep}}\right)^2\right] \qquad (3.4)$$

Here v_0 is the line-center frequency, I_{app} and I_{dep} are the appearance and depletion intensities at v_0, and Δv is the full width half maximum (FWHM) of the individual

29

components. Figure 3 shows the nascent Doppler profile of the $J_K = 5_3$ state of NH_3, which has both appearance and depletion components. The distribution of recoil velocities for individual states is characterized by a Doppler width and translational temperature T_{trans}. Translational temperatures are measured for appearance (T_{app}) and depletion (T_{dep}) based on the Gaussian fitting.
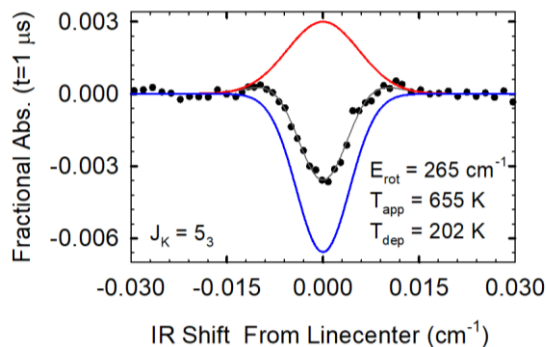
Figure 3.3 Representative appearance (red) and depletion (blue) profiles of the $J_K = 5_3$ transient absorption line profile determined from the double Gaussian fit (gray). The appearance and depletion curves give translational temperatures of $T_{app} = 655$ K and $T_{dep} = 202$ K, respectively.

Figure 3.4 shows selected profiles across the range of states probed. The lower J states show pure depletion of population. As the scattered NH_3 rotational energy increases, the signals evolve to pure appearance for states that are solely populated through collisions with vibrationally hot pyrazine.
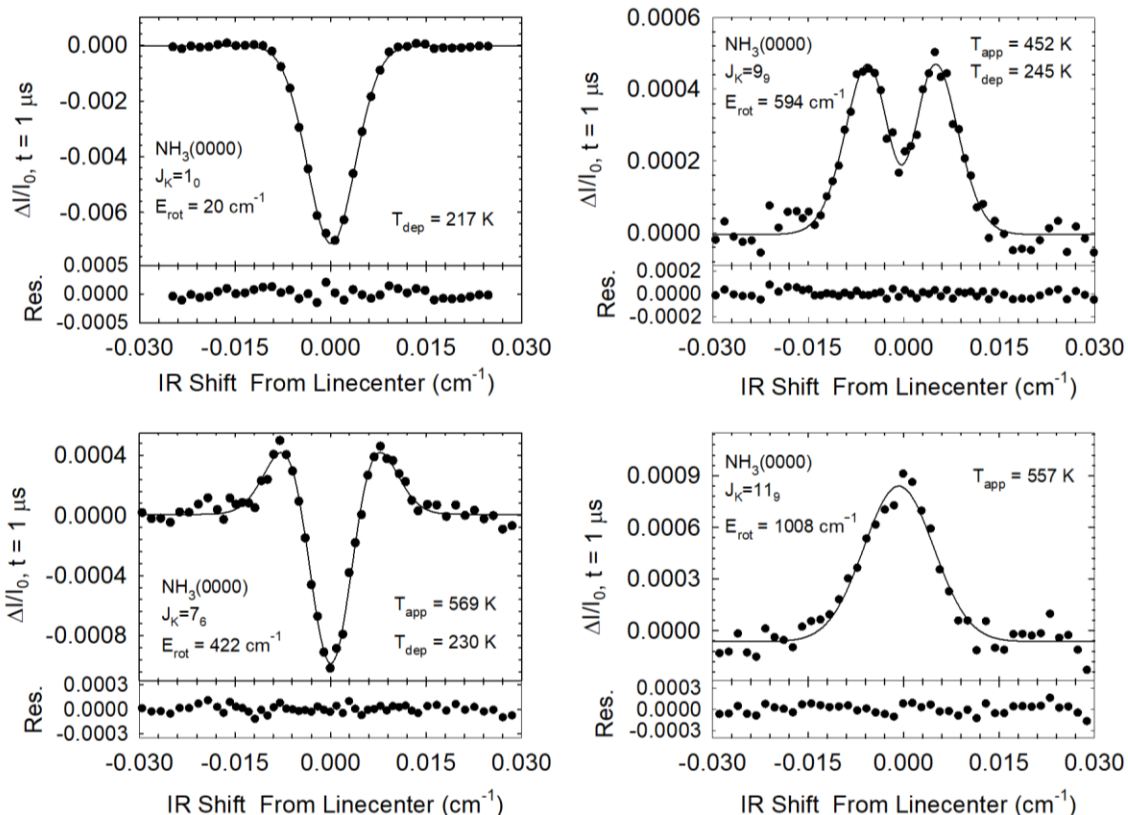
Figure 3.4. Nascent Doppler-broadened line profiles at $t = 1$ μs for a range of $NH_3(0000)$ rotational states following collisions with vibrationally hot pyrazine. Experimental transient IR data, collected at 0.01 intervals across a line, are fit to Gaussian or double-Gaussian curves, shown in solid black lines.

3.3.2 Translational and Rotational Energy Distributions of Scattered NH_3 Molecules

Table 3.1 contains the list of NH_3 states probed, their rotational energies, IR transition frequencies, and the translation temperatures for appearance and depletion. Lab-frame (T_{app} and T_{dep}) and center-of-mass (COM) frame (T_{rel}) translational temperatures for appearance signals are also shown in Table 3.1. The equations for determination of the lab and the COM frame translational temperatures are given in the notes to Table 3.1.

31

Table 3.1. Nascent FWHM line widths and translational temperatures (K) of NH_3 following collisions with pyrazine ($E_{vib} = 37900$ cm^{-1})

J_K	E_{rot} (cm^{-1}) [a]	ν (cm^{-1}) [a]	$\Delta\nu_{dep}$ (cm^{-1})	T_{dep} (K)	$\Delta\nu_{app}$ (cm^{-1})	T_{app} (K)	T_{rel} (K)
0_0	0.7934	3458.61439	0.0091	230 ± 63	—	—	—
1_1	16.173	3376.32579	0.0085	208 ± 57	—	—	—
1_0	19.8899	3376.26961	0.0086	217 ± 62	—	—	—
3_3	86.6578	3334.59825	0.0083	200 ± 55	—	—	—
5_5	205.2691	3379.41095	0.0086	213 ± 59	—	—	—
5_3	264.5166	3452.7752	0.0084	202 ± 57	0.0152	655 ± 201	731 ± 224
6_3	383.3184	3471.70323	0.0101	286 ± 81	0.0149	615 ± 188	683 ± 209
7_6	422.4582	3345.6209	0.0088	230 ± 65	0.0138	569 ± 174	627 ± 192
9_9	593.5033	3329.24938	0.0090	245 ± 72	0.0123	452 ± 129	485 ± 138
8_3	679.8367	3295.96476	—	—	0.0135	558 ± 153	613 ± 168
9_0	888.5007	3424.15428	—	—	0.0132	496 ± 136	539 ± 148
10_9	790.6807	3309.53855	—	—	0.0129	503 ± 139	547 ± 151
10_3	1052.5498	3527.76971	—	—	0.0149	587 ± 161	649 ± 178
11_9	1007.8085	3327.45158	—	—	0.0136	557 ± 152	612 ± 167
11_3	1267.2889	3230.67713	—	—	0.0112	399 ± 120	421 ± 127

a. Energies for NH_3 states and line-center transition frequencies ν_0 are from the HITRAN database.

b. Full-width half-maximum line widths for NH_3 depletion ($\Delta\nu_{dep}$) and appearance ($\Delta\nu_{app}$) from pyrazine-NH_3 collisions are determined by fitting transient line profiles at $t=1$ µs to double Gaussian functions.

c. Translational temperatures for individual rotational states are determined from the full-width half maximum line widths using $\Delta\nu_{Dop} = 2\nu_0\sqrt{\frac{2k_B T_{trans}ln(2)}{mc^2}}$ where line-center transition frequencies ν_0 is the line-center transition frequency, k_B is the Boltzmann constant, T_{trans} is lab frame translational the temperature, m is the mass of NH_3, and c is the speed of light.

d. The center-of-mass appearance translation temperatures were calculated using $T_{rel} = T_{app} + \left(m_{NH_3}/m_{pyz}\right)\left(T_{app} - T_0\right)$, where m_{pyz} is the mass of pyrazine and $T_0 = 296$ K is the initial ambient temperature.

The rotational energy dependence of the lab-frame translational appearance temperature is shown in Figure 3.5. Depletion translational temperatures are in blue and appearance translational temperatures are in red. The starting thermal temperature (296 K) is shown in a grey dashed line.
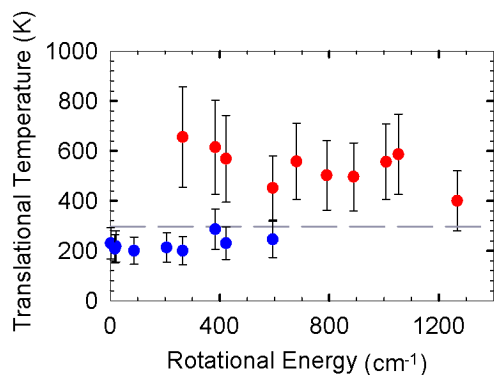
Figure 3.5. Nascent lab-frame translational energy gains of $NH_3(0000)$ following collisions with pyrazine. The depletion temperatures are J-independent and lower than the average thermal temperature ($T = 296$ K) with $\langle T_{dep} \rangle = 225\pm60$ K. The appearance temperature lower with increasing energy of the rotational state.

The data in Figure 3.5 reveal a number of interesting features about NH_3-pyrazine collisions. The depletion temperatures have values that are consistently below the ambient 296 K sample temperature. This observation shows that a slower subset of molecules is preferentially involved in quenching collisions with pyrazine and scattered out of thermally populated states while the faster subset of molecules is less involved. This result highlights the role of intermolecular attractive interactions in collisions that quench highly vibrationally excited pyrazine, wherein molecules with large initial kinetic energies in the initial 296 K NH_3 population moves too quickly to feel the influence of intermolecular attraction. The scattered NH_3 molecules have translational temperatures that are larger than their initial 296 K values, showing translational energy gained in collisions with pyrazine. In addition, translational temperatures decrease somewhat as the NH_3 rotational energy increases. It appears that a limited amount of pyrazine vibrational energy is available to be exchanged in collisions with ammonia. The constraint on the total energy imparted through collision is quite different from CO_2, for which the higher J states show

33

a large increase in the translational energy imparted. This result indicates that NH_3-pyrazine collisions are shorter-lived than CO_2-pyrazine collisions. Strong CO_2-pyrazine collisions involve chattering with multiple contacts between the molecule over a collision event. The data in Figure 3.5 show that NH_3 likely either has one or at most a few contacts during a collision.

The nascent rotational distribution of scattered $NH_3(0000)$ molecules was determined by measuring fractional IR absorption intensities at line-center of individual states relative to a reference state. The population in each state measured was determined using the FWHM of the Doppler-broadened line profiles and the absorption line-center intensity. The semi-log plot of the nascent rotational populations is shown in Figure 3.6 The rotational temperature of the scattered molecules was determined to be $T_{rot} = 480 \pm 80$ K, showing that NH_3 gains only modest amounts of rotational energy in collisions with vibrationally excited pyrazine.
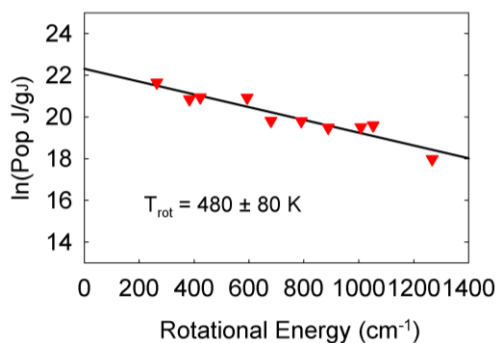
Figure 3.6. The rotational distribution for $NH_3(0000)$ at $t = 1$ μs resulting from collisions with pyrazine (E_{vib}=37900 cm^{-1}). The nascent distribution is fit to a Boltzmann distribution with $T_{rot} = 480 \pm 80$ K.

3.3.3 State-Specific Appearance Rate Constants

State-specific appearance rate constants (k_{app}^J) were determined by the method of

initial rates based using Equation 3.5 and the collisions described in Equation 3.2.

$$\frac{\Delta[NH_3(J)]_{app}}{\Delta t} = k_{app}^J[\text{NH}_3]_0[Pyr(E_{vib})]_0 \tag{3.5}$$

Here $\Delta[NH_3(J)]_{app}$ is the population of ammonia scattered into the probe state at $t = 1\,\mu s$,

$[\text{NH}_3]_0$ is the bulk ammonia number density, and $[Pyr(E_{vib})]_0$ is the number density of

excited pyrazine.

Absolute appearance rates were measured for the $J_K = 10_9$ state and used to

determine rate constants for the other rotational states based on the nascent rotational

temperature $T_{rot} = 480$ K.   The state-specific rate constants are shown in Figure 3.7. The

A and E sublevels are shown in red circles and blue triangles, respectively.
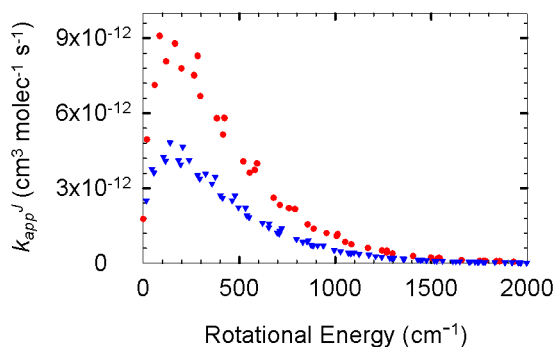
Figure 3.7. Appearance rate constants for NH$_3$(0000) from collisions with highly vibrationally excited pyrazine. An absolute rate constant was measured for the $J_K = 10_9$ state. Rate constants for the other states were determined from the $J_K = 10_9$ rate and the nascent rotational temperature $T_{rot} = 480$ K. The two curves correspond to the A and E rotational sublevels shown in red circles and blue triangles, respectively.

Summing the appearance rates of all $NH_3(0000)$ rotational states yields a total V-RT collision rate of $k_{app} = 4.0 \cdot 10^{-10}$ cm^3 molec^{-1} s^{-1}. The Lennard-Jones (LJ) rate constant for NH_3-pyrazine collisions was calculated the method from Appendix A

$$k_{LJ} = \pi \left(\frac{1}{2} \left(\sigma_{pyr} + \sigma_{NH_3} \right) \xi^{-1/8} \right)^2 \sqrt{\frac{8 k_B T}{\pi \mu}} \left(\frac{2 \xi^2 \left(\varepsilon_{pyr} \varepsilon_{NH_3} \right)}{k_B T} \right)^{1/3} \Gamma(2/3) \qquad (3.6)$$

Here μ is the reduced mass and σ, ε, and ξ are LJ parameters ($\sigma_{pyr} = 0.535$ nm, $\sigma_{NH_3} = 0.290$ nm, $\varepsilon_{pyr} = 435.5$ K/J, $\varepsilon_{NH_3} = 558$ K/J, $\xi = 1$). The resulting collision rate constant is $k_{LJ} = 7.2 \cdot 10^{-10}$ cm^3 molec^{-1} s^{-1}.

The observed value of k_{app} is approximately half that of the Lennard-Jones collision rate constant. Depletion rate constants for $J_K = 0_0, 4_3, 3_3$ were measured and with the known thermal fractional population, a total depletion rate was determined. The resulting depletion rate constant is $k_{dep} = 7.6 \pm 1.7 \cdot 10^{-10}$ cm^3 molec^{-1} s^{-1} which is very close to the Lennard-Jones rate constant. The close match in the measured depletion rate and the LJ value indicates that the LJ model works well to describe the collision rate of hot pyrazine with NH_3. The factor of two difference in the rate constant for the V-RT channel, as compared with the total collision rate, indicates that the V-RT energy transfer pathway accounts for only about half of all energy-transfer collisions. This observation indicates that V-V energy transfer plays an important role in quenching collisions of vibrationally hot pyrazine with NH_3.

NH_3 has a bending vibrational mode with an energy $E_{vib} = 1140$ cm^{-1} and pyrazine has 8 vibrational modes with energies of $E_{vib} = 1000$ to 1300 cm^{-1}. The close energy match between the donor and acceptor mode frequencies is likely to enhance V-V energy transfer.

In addition, NH$_3$ vibrations are all IR-active, which enhances near-resonant long-range energy transfer.

3.3.4 Energy Transfer Probability Distribution Function (P(ΔE))

The granular information gleaned from state-specific measurements of energy transfer in the single collision regime can be compared to average energy transfer values measured by other techniques, by transforming the state-specific data to an energy transfer distribution function, P(ΔE). State-specific appearance rate constants and translational energy gain profiles of NH$_3$ were used in the determination of P(ΔE). For P(ΔE), an average post-collision translational temperature of T_{rel} = 590 K used for each NH$_3$ state. To compute the total P(ΔE), the Maxwell-Boltzmann kinetic energy distribution was determined for each NH$_3$(0000) product state, each with an integrated intensity based on the rotational energy gain distribution and the state-specific appearance rates. The state-specific distributions (for J =0 to 22 and the associated K values) are shown in Figure 3.8a. The initial ΔE value for each curve in Figure 3.8a is based on, $\Delta E_{rot} = E_{rot}^{J} - E_{rot}^{mp}$, the difference of the rotational energy of the J state probed and the most probable rotational energy of the pre-collision molecule. A sum over the state-specific curves gives the overall energy transfer distribution shown in Figure 3.8b. The distribution has an average energy transfer value of $\langle \Delta E \rangle$ = 490 cm^{-1} per collision.
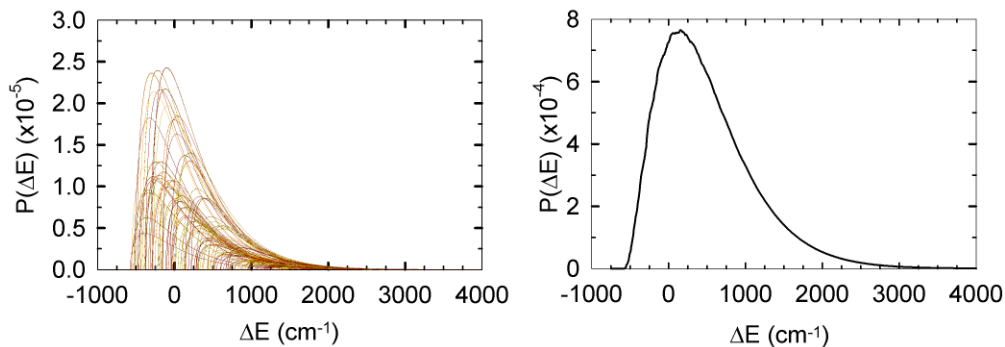
Figure 3.8. (a) The state-specific energy transfer distributions for $NH_3(J = 0$ to 22) and pyrazine. (b) The total energy transfer distribution determined by summing the state-specific distributions.

The resulting $P(\Delta E)$ distribution shows that most NH_3-pyrazine collisions have an energy transfer value less than $\Delta E \sim 2000$ cm^{-1}. This result places an upper limit on the amount of energy available in collisions that come from the vibrational modes of pyrazine and suggests that V-RT collisions with NH_3 are impulsive. Pyrazine has four vibrational modes with single quantum energy gaps near $E_{vib} \sim 3200$ cm^{-1}. However, most of pyrazine's vibrational modes have frequencies between 1000 and 1500 cm^{-1}. The observation of small amounts of rotational and translational energy indicate that NH_3-pyrazine collisions involve a small number of localized contact points that access only a small fraction of pyrazine's vibrational energy.

To compare the $P(\Delta E)$ data to IRF and KSCI studies on donor energy loss, two exponential decay fitting forms are used. A single exponential is the form used by Miller and Barker to fit IRF energy transfer data:[4]

$$P(\Delta E) = A \exp\left[-\left(\frac{\Delta E}{\alpha}\right)\right], \text{ for } \Delta E > 0 \tag{3.7}$$

Here, α is analogous to $-\langle \Delta E \rangle_{down}$, the average energy lost per collision, and A is the normalization constant. Extrapolation of Miller and Barker's data to a pyrazine donor

energy of 37900 cm⁻¹ yields $-\langle\Delta E\rangle_{down} \approx 750$ cm⁻¹. Fitting our state-resolved data to this

form gives $-\langle\Delta E\rangle_{down} = 771$ cm⁻¹, which is close to the value extrapolated from Miller

and Barker.

The introduction of a parametric exponent increases the goodness of fit and has

been used in KCSI studies.[43] The compressed exponential form is

$$P(\Delta E) = A \exp\left[-\left(\frac{\Delta E}{\alpha}\right)^Y\right], \text{ for } \Delta E > 0 \tag{3.8}$$

This functional form provides a better and more physically meaningful representation of

our collected data. The monoexponential decay would result from a sum of exponential

decays and a Y=2 would result from a sum of Gaussian functions.[44] As our P(ΔE) is a sum

of Boltzmann distributions, the resulting parametric exponent is between those two limits.

With this fit, the energy lost per collision is higher with a value of $-\langle\Delta E\rangle_{down} = 943$ cm⁻¹.

The resulting fit parameters and functions for exponential and compressed exponential

forms are shown in Figure 3.9, along with the experimental P(ΔE) data.
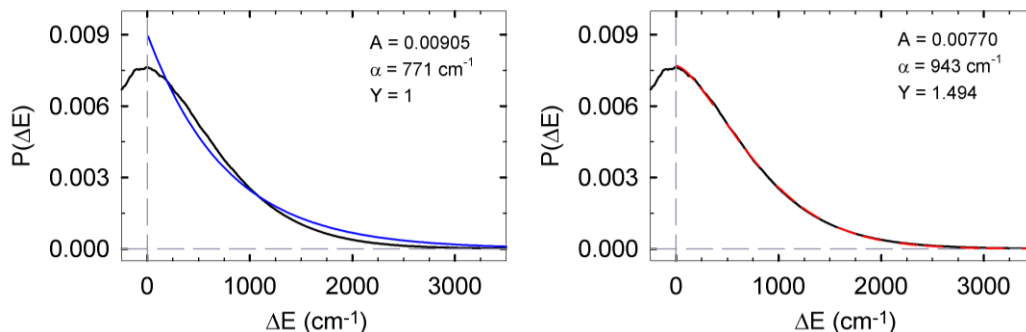
Figure 3.9. The observed P(ΔE) distribution for NH₃-pyrazine (E_{vib} = 37900 cm⁻¹) collisions was shifted such that P_{max} is at ΔE = 0. The results are fit to exponential (left) or compressed exponential (right) decay.

3.3.5 NH$_3$ Energy Transfer Distributions and Comparison to CO$_2$ and DCl

With the new results on ammonia collisions, it is now possible to compare rotational and translational energy distributions that arise from collisions with highly vibrationally excited pyrazine (E_{vib} = 37900 cm^{-1}) with a series of bath molecules: CO$_2$, DCl, and NH$_3$.[7,34] To compare these data, the change in translational energy for product states is determined using $\Delta E_{trans} = \frac{3}{2} k_B (T_{rel} - 296 \text{ K})$. To compare energy transferred for the total V-RT pathway, the change in translational energy is added to change in rotational energy. The energy dependences of the ΔE_{trans} and $(\Delta E_{trans} + \Delta E_{rot})$ are shown in Figure 3.10 as a function of the rotational energy of the NH$_3$, CO$_2$, and DCl.
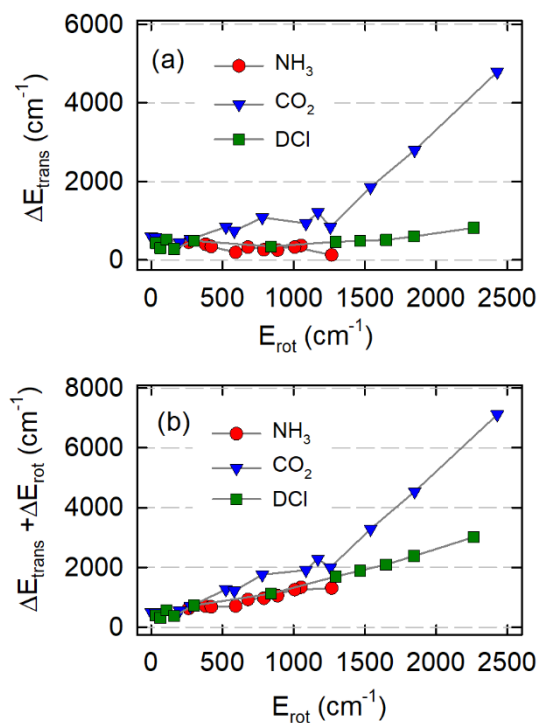
Figure 3.10. Comparison of energy transfer values for quenching collisions of pyrazine(E_{vib}) with three molecules, NH$_3$ (red circles), CO$_2$ (blue triangles), DCl (green squares). (a) Translational energy change as a function of the rotational energy of the state probed. (b) The change in total

energy (rotation and translation) as a function of the rotational energy of the state probed.

Figure 3.10 highlights a number of interesting features of collisions that quench highly vibrationally excited pyrazine. The first feature is that NH_3 gains significantly less rotational energy than either DCl or CO_2. The highest rotational energy found in the NH_3 collision products is near 1300 cm^{-1}, which is half that of either CO_2 or DCl. This observation is reflected in the rotational temperatures of the collision products. CO_2 has a bimodal distribution with a rotational temperature of $T_{rot} = 1145$ K for the strong collisions and DCl has a rotational temperature of $T_{rot} = 880$ K. NH_3 has a rotational temperature of only $T_{rot} = 480$ K.

The second feature of note in Figure 3.10 is that for a given product rotational energy, scattered CO_2, has more translational energy than either NH_3 or DCl. This behavior is present at low bath rotational energies where the NH_3 product states are observed, and at high bath rotational energies, where NH_3 products are not observed. At high rotational energies, the translational energy for CO_2 products increases sharply, as a result of chattering collisions that ultimately impart large amounts of both translational and rotational energies. DCl collisions also show this behavior, but to a lesser degree. NH_3 does not show this type of scattering behavior and has combined average ΔE values of 1100 cm^{-1} and less, consistent with the upper limit seen in the P(ΔE) data. It is likely that the structure of the bath molecules is in part responsible for these observations. CO_2 is a linear molecule with a nearly uniform mass distribution whereas NH_3 and DCl each only have one heavy atom. Limiting-case impulsive collisions that involve the heavy atoms in NH_3 and DCl are expected to impart translational, but little rotational energy, to the collision

41

products. On the other hand, if the light atoms are the points of contact during impulsive collisions, the product states will be rotationally but not translationally excited. The data in Figure 3.10a show that NH_3 scattering falls into this limiting behavior, with higher recoil values observed for the lower energy rotational states. Similarly, some DCl collisions lead to only moderate translational energy gains for the lower rotational states, whereas other DCl collisions lead to strong collisions with both rotational and translational energy. It is clear from the data in Figure 3.10 that V-RT quenching collisions of pyrazine with NH_3 involve smaller amounts of energy transfer than for DCl and CO_2 and that NH_3 does not exhibit chattering collisions.

The collision dynamics that are responsible for the observed energy distributions in the scattered molecules are influenced by the masses of the collision partners, the masses of the atoms involved in the collisions and the intermolecular forces. An additional influence on pyrazine quenching collisions is related to differences in the relative velocity of the collision partners. NH_3 is less massive than CO_2 and DCl. and it has a relative velocity that is approximately 35% higher than those for CO_2 and DCl for the same translational energy. These factors suggest that NH_3-pyrazine collisions are shorter lived by about 70% compared to CO_2 and DCl, which reduces the probability for subsequent chattering collisions that lead to large ΔE values.

Finally, we address the question of how effective NH_3 is as a quencher of highly vibrationally excited molecules. Miller and Barker reported that overall average energy transfers values are larger for NH_3 than for CO_2, with $\langle \Delta E \rangle = 460$ cm^{-1} for NH_3 and 173 cm^{-1} for CO_2, based on IRF energy loss measurements for pyrazine($E_{vib} = 24000$ cm^{-1}). From product state measurements of the V-RT pathway for pyrazine($E_{vib} = 37900$ cm^{-1}),

CO_2 has larger $\langle \Delta E \rangle$ values than NH_3, with $\langle \Delta E \rangle = 771$ cm^{-1} for NH_3 and 1042 cm^{-1} for CO_2, based on single exponential fitting of $P(\Delta E)$ measurements. Overall, the $\langle \Delta E \rangle$ values from IRF studies have lower values than those from the state-resolved probe IR experiments because the donor energy is smaller in the IRF experiments. A key result of this study is that the V-RT channel for collisions with NH_3 entails energy transfer in single collisions that with ΔE values that are less than 2000 cm^{-1}. Our rate measurements show that the V-RT pathway accounts for about half of all collisions, and that V-V energy transfer accounts for a significant fraction of the relaxation. We conclude that NH_3 is an effective quencher of highly excited pyrazine through a combination of V-RT and V-V energy transfer.

4.3 Conclusions

This Chapter presents nascent state-resolved energy gain profiles of NH_3 following collisions with highly vibrationally excited pyrazine ($E_{vib} = 37900$ cm^{-1}) using high-resolution transient IR absorption spectroscopy. Through measurements individual rotational states of the $NH_3(0000)$ we found that the V-RT energy transfer pathway involves relatively small amounts of rotational and translational energy imparted to NH_3 through collision. The translational energy gain decreases as a function of increasing rotational energy of the NH_3 products. The limited total energy observed for products indicates that the V-RT pathway involves short-lived impulsive collisions with NH_3. In contrast, V-RT quenching collisions with CO_2, and to a lesser extent with DCl, exhibit much larger ΔE values corresponding with long-lived chattering collisions involving multiple contacts with hot pyrazine during a collision.

The measured absolute rate constants for the appearance of $NH_3(0000)$ indicates there is significant contribution to the V-V energy pathway. The overall appearance rate constant for V-RT energy transfer was measured to be $k_{app} = 4.0 \cdot 10^{-10}$ cm^3 molec^{-1} s^{-1} which is about half the value of the collision rate constant. The total depletion rate constant was measured with a value of $k_{dep} = 7.6 \cdot 10^{-10}$ cm^3 molec^{-1} s^{-1}. The Lennard-Jones collision rate constant was calculated as $k_{LJ} = 7.2 \cdot 10^{-10}$ cm^3 molec^{-1} s^{-1}. The similarity of the depletion rate constant and the LJ value indicates that the LJ model is appropriate for NH_3-pyrazine collisions. However, the large difference between the depletion rate and the V-RT energy transfer rate indicates that V-V energy transfer is an important energy transfer pathway for NH_3 collisions and accounts for nearly half of collisions.

Chapter 4: Alkylation Effects on the Collision Dynamics of Highly Vibrationally Excited Pyridines and $CO_2(00^00, J)$

4.1 Introduction
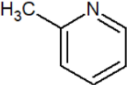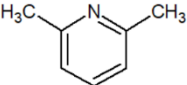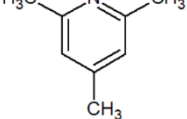
Activated molecules play a crucial role in the chemistry of molecules in extreme energy states and the interactions of these molecules dictate how energy is redistributed during collisions. Although much work has been done to determine the nature of energy transfer, a clear picture of molecular energy transfer has yet to emerge and many questions remain unanswered. The structure of the collision partners, vibrational state density, their van der Waals interactions, and potentially other variables affect how collisional energy transfer occurs.

Collisional energy transfer between molecules can be described by two limiting cases: strong and weak collisions.[2] Strong collisions are characterized by large amounts of energy transfer, deactivating activated molecules in one or a few collisions.[3] Weak collisions have low energy transfer values and many collisions are required to deactivate the donor. Here, we examine the strong collision case, probing acceptor molecules that have final rotational energies well above the 296 K average.

Aromatic molecules such as pyridine and its methylated derivatives have been the significant focus of collisional energy transfer studies. These donor molecules have many internal degrees of freedom, allowing the energy to be distributed across the vibrational modes of the donor. Appendix B lists the average energy per mode in the vibrationally excited molecules investigated here. These molecules can also frequently be excited to metastable states with energies on the magnitude of bond breaking and undergo dynamics

45

in these highly excited states before dissociation. The structures of these molecules are shown in Figure 4.1 along with their state densities when excited by 266 nm light. By successive methylation, the molecules can be modified to vary steric effects, long range forces, and the vibrational state density. For a given excitation energy, increasing state density lowers the average energy in each vibrational mode. In CO_2-pyridine van der Waals complexes, experiments have found that the strongest interaction is between the nitrogen (N) on the ring of the pyridine and the carbon (C) of CO_2.[16] Collisional energy transfer can be influenced by anisotropic interaction potentials. In interactions of CO_2 with 2,6-lutidine the interaction of the C atom with the N atom remains the strongest intermolecular attraction.[17] Computational studies of 2,6-lutidine show this attraction potential is weaker and over a longer distance than with pyridine.[18] The N-CO_2 interaction is present for the donor molecules presented in Table 4.1. If these forces are involved in the collisional energy transfer dynamics, it is likely that steric effects around the N atom will influence the partitioning of the transferred energy.

Table 4.1 Structure and State Densities of Donor Molecules Following λ=266 nm Excitation

	Pyridine	2-Picoline	2,6-Lutidine	2,4,6-Collidine
Formula	C_5H_5N	C_6H_7N	C_7H_9N	$C_8H_{11}N$
Structure				
Atoms	11	14	17	20
Modes	27	36	45	54
E_{vib} (cm^{-1})	37900	38300	38700	39100
State Density	$2.6 \cdot 10^{13}$	$1.7 \cdot 10^{18}$	$4.4 \cdot 10^{22}$	$1.7 \cdot 10^{27}$
<E/mode> (cm^{-1})	1403	1064	860	724

Previous work has explored the effect methylation and state density of the pyridine ring has on strong collisions.[19–21,45] Rotational state distributions of $CO_2(J \geq 60)$ following collisions with highly vibrationally excited (E_{vib} = 37900 to 38700 cm^{-1}) pyridine, 2-picoline, and 2,6-lutidine were measured with transient IR absorption.[20] It was found that methylation of the donor molecule reduces the amount of both translational and rotational energy imparted to CO_2. In addition, the high-J cross section scattered CO_2 molecules increased upon donor methylation. Similar results were found when H_2O was used as the energy acceptor, suggesting that the donor molecule plays an important role in the dynamics.[19] Some tunable photoexcitation studies on pyridine found that increasing the donor state density by a factor of 10 did not affect the V-RT pathway but did increase the high J cross section by an order of magnitude.[21] Other CO_2 scattering experiments showed that changing the internal energy of an azulene donor by a factor of two affected both the CO_2 product distributions and the strong collision rate constants. By studying 2,4,6-collidine, we further investigate the effect state density has on the collisional energy transfer and how the effect of state density compares to steric hindrance considerations related to attractive intermolecular forces.

In this work, we measure and report product state distributions of $CO_2(J$ = 58 to 78) from strong collisions of CO_2 with highly vibrationally excited 2,4,6-collidine (E_{vib} = 39100 cm^{-1}). Nascent rotational distributions are reported along with translational energy distributions based on transient Doppler profile measurements. This study investigates the effects of the vibrational state density and the structure of the interaction region of the donor molecule on energy transfer through impulsive collisions.

4.2 Experimental Methods

The state-resolved high-resolution transient IR absorption spectrometer for this experiment is described in Chapter 2. The key components of the spectrometer are presented here and shown in Fig. 4.1. The spectrometer features spatially overlapped UV-pump and IR-probe beams from a Nd:YAG-pumped optical parametric oscillator (OPO) and a single mode IR lead-salt diode laser. The two beams are guided through a 3 m flowing-gas collision cell. Active feedback control of the IR probe output is used for fine wavelength control. Flowing-gas pressures through the collision cell were kept at a total of ~10 mTorr with a 1:1 ratio of collidine to CO_2.
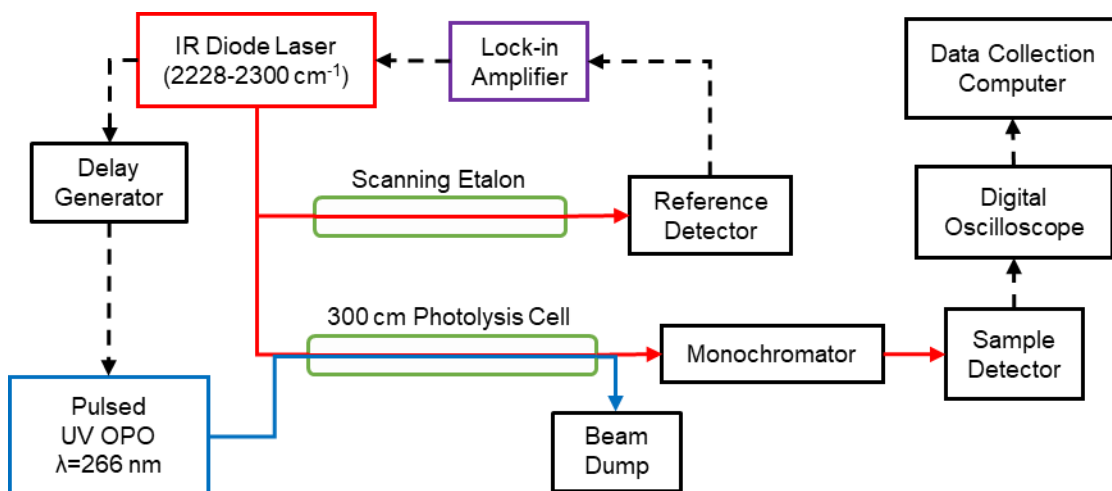
Figure 4.1 Schematic of the high-resolution transient IR absorption spectrometer. A pulsed OPO prepared the collidine in a highly vibrationally excited state using λ=266 nm light. The IR diode laser probed CO_2 collision product states using fractional absorption of the antisymmetric stretch mode.

The UV light source is an OPO system (Horizon, Continuum Lasers) with a spectral resolution of 10 cm^{-1} that is pumped by a Nd:YAG laser at a repetition rate of 10 Hz. The third harmonic ($\lambda = 355$ nm) of the Nd:YAG laser was used to pump the OPO system. A set of OPO crystals in conjunction with doubling crystals produced the 266 nm light used

in this experiment. The repetition rate of the OPO output was reduced to 1 Hz with a mechanical shutter. This set-up allowed the flowing gas cell to refresh the sample of collidine and CO_2 between laser pulses.

The Pd-salt diode laser used as the IR probe source is single-mode with high-resolution output at $\lambda \approx 4.4$ µm and a spectral resolution of $\Delta\nu_{IR} = 0.0003$ cm^{-1}. For wavelength locking, the IR light was modulated at a frequency of 1 kHz. IR light was used to probe individual rotational states of the ground vibrationless $CO_2(00^00)$ state with fundamental transitions to the $CO_2(00^01)$ antisymmetric stretch. Transient absorption signals were collected on an InSb detector (Teledyne-Judson) with a matched signal amplifier (Perry Amplifier) with a 300 ns rise time. For Doppler profiles, IR wavelength control was achieved by optically locking the IR modulation to a fringe of a tunable Fabry-Perot etalon with a lock-in-amplifier (Stanford Research Systems). For line-center measurements, the IR wavelength was locked to CO_2 absorption lines using a reference cell.

Transient fractional IR absorption signals for the CO_2 collision products were collected by measuring the absorption (ΔI) and (I_t) transmitted intensities of the IR light simultaneously on a quad-channel 200 MHz digital oscilloscope (LeCroy). The signals were averaged over 60 UV laser pulses on the digital oscilloscope and transferred to the data collection computer with LabVIEW code.

4.2.1 Photoexcitation and Preparation of the Vibrationally Hot Collidine

The 266 nm light from the OPO system was used to electronically excite the collidine from the ground S_0 state to the S_2 state. As with other pyridines, the main source of relaxation from the S_2 state is internal conversion to the electronic ground state, leading

to large amounts of vibrational energy in S_0. The excitation and internal conversion processes are

$$Col(S_0, \ 296 \text{ K}) + h\nu \ (\lambda = 266 \text{ nm}) \longrightarrow Col(S_2) \qquad (4.1)$$

and $$Col(S_2) \longrightarrow Col(S_0, \ E_{vib} = 39100 \text{ cm}^{-1}) \qquad (4.2)$$
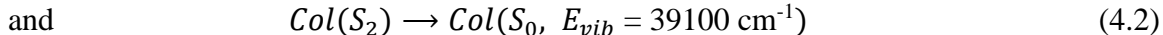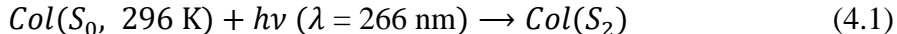
Here, *Col* represents the collidine and E_{vib} is the vibrational energy. Once excited to the S_2 state, the internal conversion has a quantum yield near unity, with other relaxation processes having quantum yields on the order of 10^{-5} as an upper limit. Other pyridine derivatives undergo internal conversion on a 3 ps timescale.[46,47] For excitation with 266 nm light, the S_2 state of collidine has a dissociation lifetime longer than 500 μs.[9] The number density of vibrationally hot collidine is determined by the UV absorption and the interaction volume in the cell. The amount of excited collidine is kept under 10% through a combination of pressure and UV power to reduce the probability of collisions between two vibrationally hot molecules.

4.2.2 Transient IR Probing of the $CO_2(00^00)$ Collision Products

The hot collidine undergoes collision with CO_2, at an ambient temperature of 296 K, and transfers energy from donor vibration into CO_2 rotation, translation, and/or vibration. This process in described by

$$Col(E_{vib}=39100 \text{ cm}^{-1}) + CO_2(296 \text{ K}) \xrightarrow{k_{app}^J} Col(E_{vib}') + CO_2(E_{vib}, J, vel) \qquad (4.3)$$
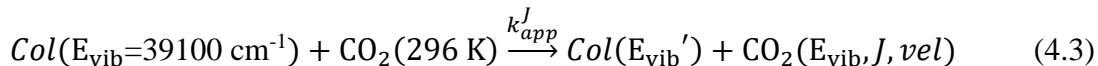
Here, J is the rotational quantum number, vel is the CO_2 velocity, and k_{app}^J is the state-specific rate constant. The CO_2 collision products were probed with transient absorption

spectroscopy using fundamental rovibrational transitions of the antisymmetric stretch. In this study, the CO_2 ground vibrationless state was probed

$$CO_2(00^00, J, vel) + h\nu(\lambda \approx 4.4 \text{ μm}) \longrightarrow CO_2(00^01, J\text{-}1, vel) \tag{4.4}$$
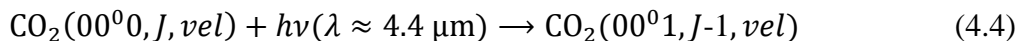
Here (00^00) and (00^01) represent the ground vibrationless state and the vibrationall excited state with one quanta in the antisymmetric stretch mode respectively. Frequencies for the transitions used in this study are from the HITRAN online database.[30,31]

Transient IR absorption signals and Doppler profiles for individual rotational states with $58 \leq J \leq 78$ were collected following collisions with vibrationally hot collidine. For Doppler profiles, the transient IR absorption signals are collected in discrete wavelength steps across a transition, allowing for the determination of a line width and therefore the translation temperature and average energy. Number densities of CO_2 in each rotational state probed were determined using IR absorption strengths from the HITRAN database and observed Doppler width.

4.3 Results & Discussion

4.3.1 Doppler-Broadened Line Profiles of Scattered CO_2 Molecules

Nascent Doppler profiles of CO_2 molecules following collisions with highly vibrationally excited 2,4,6-collidine were collected at several CO_2 rotational states. The line center transient IR absorption signal for $CO_2(J = 68)$ is shown in Fig 4.2a. The transient Doppler profile is based on signal intensities at $t = 1$ μs collected at discrete wavelength steps across the transition feature. The Doppler profile and Gaussian fit are shown in Fig. 4.2b.
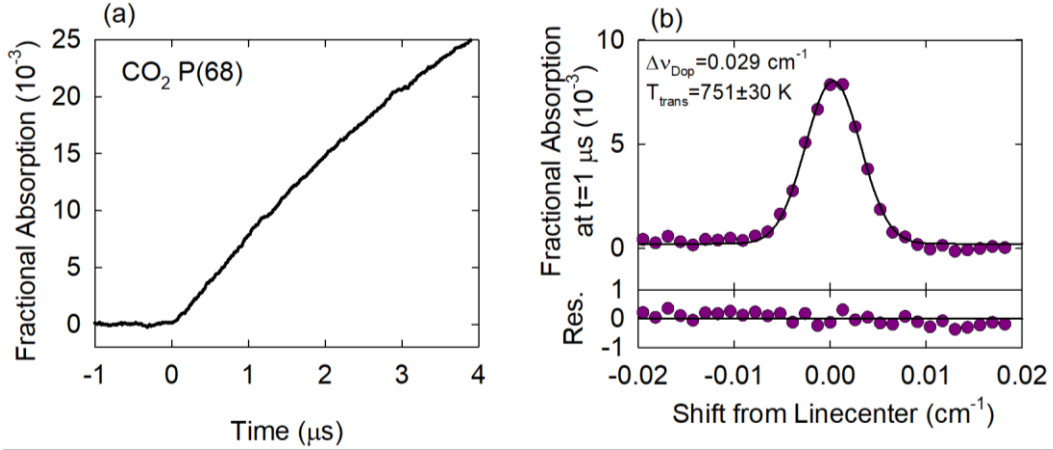
Figure 4.2 (a) Transient fractional IR absorption signal at linecenter of the CO_2 $J = 68$ state following the UV laser pulse. (b) The Doppler profile for the $J = 68$ state at 1 µs after the UV excitation pulse. Translational temperature is determined from the FWHM of the transition feature.

Profiles are fit to Gaussian curves to determine the observed Doppler width Δv_{obs}, the full width at half maximum (FWMH). The Doppler width is directly related to the translational temperature via

$$\Delta v_{obs} = v_0 \sqrt{\frac{8k_B T_{trans} \, ln2}{mc^2}} \qquad (4.5)$$

Here m is the mass of CO_2, v_0 is the linecenter frequency, k_B is the Boltzmann constant, and T_{trans} is the lab-frame translational temperature.

4.3.2 Translational and Rotational Energy Distributions of Scattered CO_2 Molecules

The CO_2 probe transitions, their transient Doppler linewidths, and translational temperature are listed in Table 4.2. The center-of-mass (COM) frame translational temperatures (T_{rel}) and T_{trans} values are also shown in Table 4.2. The determination of T_{rel} is

$$T_{rel} = T_{trans} + (T_{trans} - T_0) \cdot \left(\frac{m_{CO_2}}{m_{Col}}\right) \qquad (4.6)$$

Here T_0 is the initial temperature of the sample, 296 K, and m_{CO_2} and m_{Col} are mass of

CO_2 and 2,4,6-collidine, respectively.

Table 4.2 $CO_2(00^00)$ *J*-Dependent Doppler Widths and Translational Temperatures

J	E_{rot} (cm^{-1})	ν_0 (cm^{-1})	$\Delta\nu_{obs}$(cm^{-1})	T_{trans} (K)	T_{rel} (K)
58	1333.7679	2293.8109	0.0053	468 ± 37	530 ± 50
60	1426.4153	2291.5416	0.0059	566 ± 100	665 ± 137
68	1827.9724	2282.2267	0.0067	751 ± 30	916 ± 41
70	1936.0953	2279.8387	0.0064	684 ± 29	825 ± 39
74	2161.6091	2274.9919	0.0067	738 ± 30	899 ± 41
76	2278.9963	2272.5330	0.0075	930 ± 73	1160 ± 99
78	2399.4680	2270.0507	0.0074	889 ± 102	1105 ± 139

The translational temperatures of the collision products increase by a factor of 2 across the states probed here with the higher rotational states having more translational energy. Figure 4.3 shows the measured T_{rel} values for CO_2-collidine and compares the results with other pyridine-based donors. The 2,4,6-collidine measurements for this study are red triangles in both plots. Pyridine imparts the highest amount of translational energy to the CO_2 acceptor molecule for the range of rotational states probed. As methyl groups are added to the donor molecule, the translational energy drops. However, past the first methyl group added (2-picoline), the reduction in translational energies is much smaller. The T_{rel} values from the methylated donors have similar *J*-dependences, indicating that the energy transfer dynamics are similar. Overall, the larger donor molecules lead to smaller recoil energies from collisions. Structures, state densities, vibrational modes, and average energy per mode are compared for the molecules in Table 4.1.
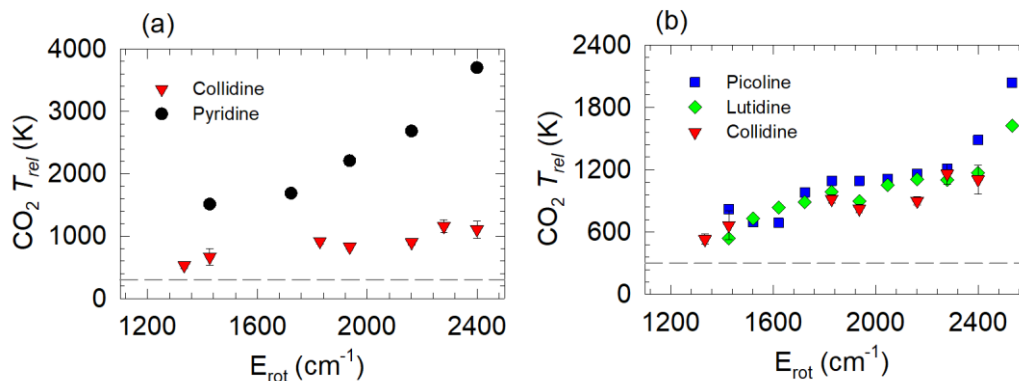
Figure 4.3. T_{rel} values of donor-CO_2 collisions. Results for hot collidine collisions compared to those for (a) pyridine and (b) picoline and lutidine.

Relative populations in a number of $CO_2(J)$ states were determined by measuring line-center intensities and integrating over individual the line profiles. Figure 4.4 shows the rotational distribution measured for this study, along with previously measured distributions for other pyridine donors. Overall, the comparison shows that adding methyl groups to the donor leads to less rotational energy imparted to CO_2 through collisions with the vibrationally hot donor molecules. However, the rotational temperature from collidine collisions is nearly identical to that for 2,6-lutidine collisions.
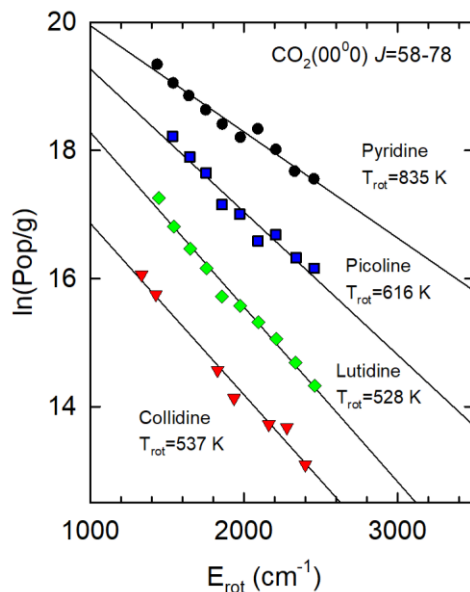
Figure 4.4 Rotational distributions for $CO_2(00^00)$ following collisions with various pyridine donor molecules. The result of collisions with collidine are shown in red triangles.

Here we consider two aspects of the donor molecules that impact energy transfer dynamics. First, the structure and steric hinderance of the methylated donor molecules will affect the interaction geometries that can be accessed in the collisions. Steric crowding lowers the probability of accessing parts of the donor molecules, which can change how the energy is imparted through collisions. It is clear from the structures given in Table 4.1 that collidine is sterically similar to the 2,6-lutidine. The similarity of their scattering dynamics indicates that attractive intermolecular forces are involved in the energy transfer processes.

The second aspect to consider is the state density and average energy per vibrational mode of the donor molecule. The vibrational mode frequencies for each molecule were calculated using Gaussian 9 and used as input to the Beyer-Swinehart algorithm to obtain a direct count of the state density.[48] A higher state density of the donor molecule

corresponds to a lower average vibrational energy per mode. The difference in the average energy per mode becomes smaller as methyl groups are added sequentially to the pyridine ring. The difference in this value for pyridine and 2-picoline is 340 cm^{-1} and for picoline and 2,6-lutidine it is 203 cm^{-1}. For 2,6-lutidine and 2,4,6-collidine, the difference is only 136 cm^{-1}.

The data presented here show that the amounts of energy transferred in the V-R pathway is affected substantially by the molecular structure of the donor molecule. The translational temperatures show a large drop going from pyridine to 2-picoline, for which the strongest interaction site is sterically hindered by the addition of one methyl group. Addition of more methyl groups leads to increased state densities but does not substantially reduce the translational energy imparted to the collision products. Figure 4.5 shows the average rotational energy gain over thermal for the CO_2 high J states. The change in rotational energy is defined as $<\Delta E_{rot}> = k_B(T_{rot} - 296\ K)$. The rotational energy of the scattered CO_2 drops as the N on the pyridine ring is surrounded with methyl groups. The addition of the third methyl group in 2,4,6-collidine does not change the outcome of the collisions when compared to 2,6-lutidine.
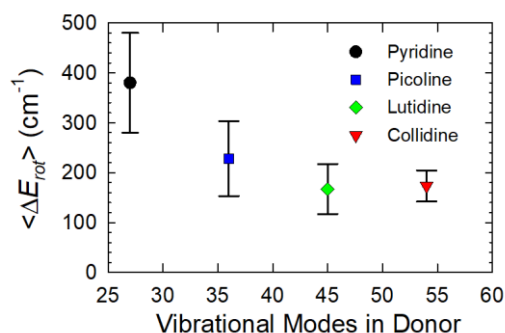
Figure 4.5 The average change in rotational energy, $<\Delta E_{rot}>$ as a function of number of vibrational modes in the donor molecule.

56

4.3.3 State-Specific Appearance Rate Constants for Strong Collisions

Appearance rate constants for $J = 60$ to 78 were measured and compared to molecules scattered into these states by other pyridine derivatives. The method of initial rates was used to measure the absolute appearance rate constant for scattered CO_2 molecules into the $J = 74$ state. Equation 4.3 defines the rate constant k_{app}^J and Equation 4.7 shows how initial rates were determined. The absolute number density of CO_2 $J = 74$ was determined with repeated line-center fractional absorption measurements and the transient Doppler linewidths.

$$\frac{\Delta[CO_2(J=74)]_t}{\Delta t} = k_{app}^J [CO_2]_0 [Col(E_{vib})]_0 \tag{4.7}$$

Here, $[CO_2]_0$ and $[Col(E_{vib})]_0$ are the initial number densities of the CO_2, 2,4,6-collidine measured with the UV-pump beam absorption through the cell, and k_{app}^J is the state-specific appearance rate constant. State-specific rate constants for the other rotational states are determined by scaling the rotational temperature to the absolute rate measured for $CO_2(J = 74)$. The rate measurements for CO_2-collidine collisions are compared to rate constants for other pyridine donors in Fig 4.6.
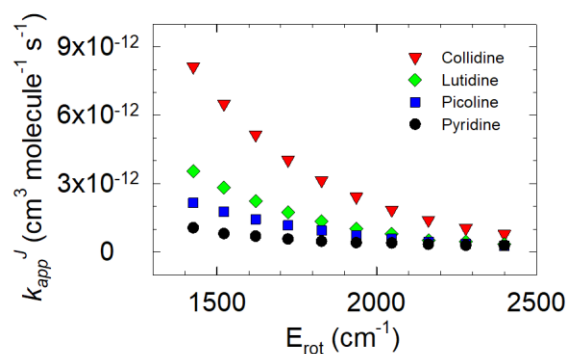
Figure 4.6 State-specific appearance rate constants for CO_2 $J = 60$ to 78. The collidine measurements are in red triangles. Previously reported rate constants for lutidine, picoline, and pyridine are in green diamonds, blue squares, and black circles.

The state-specific rate constants increase as the number of donor methyl groups increase for the states probed. This result indicates that in the strong collision regime, CO_2 is more effective at quenching the vibrational energy of donor molecules that have higher state density. Collidine transfers smaller amounts of energy to CO_2 based on the translational and rotational distributions reported here, but the energy is transferred more often.

To describe the strong collision pathway, and compare to the other donor molecules, we define an integrated rate constant over the high J states by

$$k^{int} = \sum_{J=60}^{78} k_{app}^J \tag{4.8}$$

Figure 4.7 shows the comparison of these integrated rate constants.

58
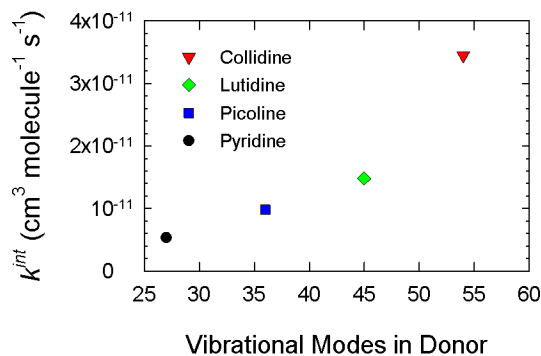
Figure 4.7 The integrated rate constants for high-J CO_2(J = 60 to 78) are compared for the 4 donor molecules. The appearance rate constant for CO_2 from strong collisions increases as the donor state density increases.

In comparing the integrated rate constants, the appearance of CO_2 from strong collisions is greatly increased for 2,4,6-collidine. For the four molecules compared, an increase of state density leads to a higher rate constant.

The overall Lennard-Jones (LJ) collision rate constants for CO_2 with 2-picoline is $k_{Pic}^{LJ} = 7.38 \cdot 10^{-10}$ and 2,6-lutidine is $k_{Lut}^{LJ} = 7.94 \cdot 10^{-10}$ in units of cm³ molec⁻¹ s⁻¹ at 296 K.[20] The method described in Appendix A was used to determine a LJ rate constant for CO_2-collidine collisions. The LJ rate constant is defined

$$k^{LJ} = \pi \left(\frac{1}{2}\left(\sigma_{donor} + \sigma_{CO_2}\right)\xi^{-1/8}\right)^2 \sqrt{\frac{8k_BT}{\pi\mu}} \left(\frac{2\xi^2\left(\varepsilon_{donor}\varepsilon_{CO_2}\right)}{k_BT}\right)^{1/3} \Gamma(2/3) \qquad (4.8)$$

Here μ is the reduced mass of the CO_2-donor pair and σ, ε, and ξ are Lennard-Jones parameters. We estimated values for CO_2-collidine parameters based on a polynomial fit of the parameters for the other pyridines and the number of vibrational modes. Extrapolation with this method gives a CO_2-collidine collision rate of $k_{Col}^{LJ} = 8.83 \cdot 10^{-10}$ cm³ molec⁻¹ s⁻¹. The LJ collision rates are relatively constant and do not account for the striking donor dependence in the appearance rates.

59

We have characterized the energy distributions of $CO_2(J = 58$ to $78)$ molecules scattered from strong collisions with vibrationally hot 2,4,6-collidine and compared the results with previous studies. The addition of these measurements to the previous work clearly shows how the state density and structure of the molecules under investigation influence strong collision dynamics of highly vibrationally excited molecules.

Our measurements of the Doppler-broadened line profiles show low amounts of translational energy released by CO_2-collidine collisions, consistent with the collision dynamics for 2-picoline and 2,6-lutidine. Despite orders of magnitude difference in state density between 2,6-lutidine and 2,4,6-collidine, the similar translational and rotational temperatures indicate that structure and associated steric hinderance around the strongly interacting region of the donor molecules have an important impact on the extent of translational energy imparted through collisions. The rotational energy gains in the CO_2 collision partner also appear to be affected more by the structure of the interaction region than the state density. Nascent rotational temperatures show a marked decrease as methyl groups are added adjacent to the N on the pyridine ring. When comparing 2,6-lutidine and 2,4,6-collidine, the state density of collidine is 4 orders of magnitude higher and the rotational temperatures are nearly the same within experimental uncertainty. For both donors, the N is flanked by methyl groups on either side making the steric hinderance to the strongest interaction region the same.

Integrated collision rate constants for high-J CO_2 show a strong dependence on donor molecule size and therefore state density. This result is similar to experiments that change measure the state density dependence on CO_2-pyrazine collisions using tunable UV

excitation.[21]   There is a dramatic increase in appearance rate constants for molecules resulting from strong collisions; the integrated rate constant increased by 2.5 from $k_{Lut}^{int} = 1.48 \cdot 10^{-11}$ cm^3 molec^{-1} s^{-1} for 2,6-lutidine to $k_{Col}^{int} = 3.45 \cdot 10^{-11}$ cm^3 molec^{-1} s^{-1} for 2,4,6-collidine. The lutidine and collidine have the same structure around the strongest point of interaction, showing the rate increase is from the size and state density increase of the donor molecule. With more vibrational modes populated, there is an increased probability of rotational energy gained by the CO_2 molecule from collision with the vibrationally hot donor.

Chapter 5: Photodissociation of Sulfur Dioxide

5.1 Introduction

Sulfur dioxide, SO_2, is an important species in the atmospheres of Earth and other planets, and it has been detected in the interstellar medium. The discovery of sulfur mass-independent fractionation (S-MIF) in the early Earth rock record has led to a renewed interest in the UV photochemistry of SO_2. In particular, the UV photodissociation of SO_2 may be important in sudden changes in sulfur isotope concentrations that took place 2500 million years ago, when the Earth's atmosphere became oxygenated and blocked UV light from the sun. [49–51] It is known that the $SO_2(\tilde{C}^1B_2)$ state undergoes predissociation with λ = 165 to 220 nm light and it could be that isotopic differences in the predissociation explain isotope differences in the early Earth rock record. A number of recent photochemistry studies have addressed this question but a full understanding of the S-MIF source is incomplete.[52–54]

Photoexcitation to the $SO_2(\tilde{C}^1B_2)$ state has discrete vibronic bands, beginning at λ = 240 nm and continuing to λ = 165 nm.[22–25,55] At 296 K, the onset of predissociation is near 220 nm, where a sharp drop in fluorescence intensity was first reported by Okabe.[56] The photodissociation products are $SO(X\,^3\Sigma^-) + O(\,^3P_J)$, which must be generated through non-adiabatic crossings, because the $\tilde{C}$ state correlates diabatically the higher energy $SO(\tilde{a}^1\Delta) + O(\,^1D)$ product states. Possible coupling mechanisms include internal conversion to the $\tilde{X}^1A_1$ state, intersystem crossing to the repulsive $2\,^3A'$ state, and non-adiabatic coupling with the repulsive $\tilde{D}^1A'$ state at higher energies.

The spectroscopy of the $\tilde{C}^1B_2 \leftarrow \tilde{X}^1A_1$ band and its dissociation dynamics have been studied with a number of experimental approaches. These studies show that the

photochemistry varies with excitation wavelength. The vibrational distribution for the SO products becomes inverted as the photolysis wavelength is tuned from 207 nm to 202 nm.[57] Other studies with 193 nm excitation report inverted and bimodal vibrational distributions with varying amounts of rotational excitation.[57–60] The SO rotational states and O atom electronic states are split by spin-rotation and spin-orbit coupling, respectively, and spin-polarized SO products have been observed at threshold and at 193 nm excitation, although with different polarization ordering. The O atom products are spin-polarized for excitation at 217 nm but statistical at 193 nm.[61,62]

The work presented here is the part of a joint experimental and theoretical project to investigate the wavelength-dependent dynamics of SO_2 photodissociation. Figure 5.1 presents potential energy curves describing $SO_2(\widetilde{C})$ state that is coupled to a repulsive $\widetilde{D}$ singlet state. These data were calculated by collaborators using multireference configuration interactions calculations with single and double excitations with the Davidson correction (MRCI-F12+Q) at a fixed Jacobian bond angle of 104.3°.[29,63] The relevant photolysis energies used in the experiments are highlighted in gray. The excitation energies shown have been scaled to the calculated $\widetilde{C}$ state minimum (at bent geometry) by adding 780 cm^{-1} for the $\widetilde{C}$ state zero-point energy and the known excitation energy within the $\widetilde{C}$ state. Figure 5.1 shows that the excitation energies used here are not sufficient to overcome the $\widetilde{C}$ state barrier caused by coupling to the D state, when the bond angle is fixed. The dissociation barrier is expected to change as a function of the bending angle and the state (or states) involved in the electronic coupling. The repulsive $2(^3A')$ triplet state is also shown in Figure 5.1 and is a candidate for dissociative coupling at lower photon energies. Additional repulsive states are predicted to interact with the $\widetilde{C}$ state at higher

energies, corresponding to higher dissociation barriers. Spin-orbit coupling strengths and the bending angle are also expected to affect the barrier height.
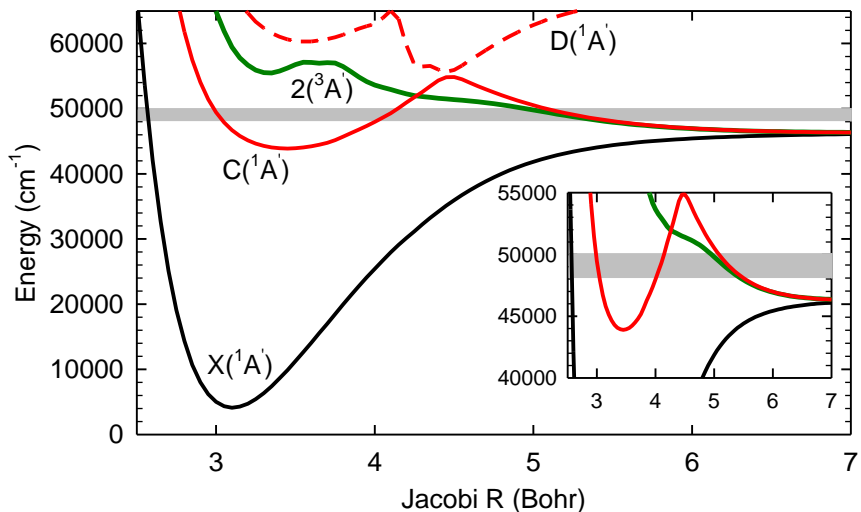
Figure 5.1 Potential energy curves for SO_2 at a fixed Jacobi angle of 104.3°. The $SO_2(\widetilde{X})$ state is shown in black. The $\widetilde{C}$ ($^1A'$) and $\widetilde{D}$ ($^1A'$) states couple near R=4.4 Bohr to form a metastable, predissociative state. The repulsive $2(^3A')$ crosses the $\widetilde{C}$ state at lower energy and could be responsible for dissociation at lower photon energies, as shown in the inset.

Dissociation from the $\widetilde{C}$ state is not prompt; the lifetime of this state near threshold is 45 ns, and it drops to 10 ps at 193 nm.[55,64,65] Photofragment measurements report anisotropy values of $\beta = 0$ for photolysis at 193 nm and between 202 nm and 207 nm, consistent with a long-lived dissociative state. [57,62,66,67] The $\widetilde{C}$ state has a number of interesting features. Based on previous spectroscopic measurements and recent theoretical work, the ν_3 antisymmetric stretch has an unusually low frequency near 220 cm^{-1}, with large anharmonicity and a double well potential along the ν_3 mode.[26–29] The $\widetilde{C}$ state absorption spectrum does not have regular vibronic band progressions and dispersed emission intensities vary with the vibrational symmetry and photolysis wavelength.[68]

The extent to which the $\widetilde{C}$ state energy is randomized prior to dissociation will depend on the Franck-Condon-active modes and the extent to which those modes are coupled in the $\widetilde{C}$ state. When triatomic molecules predissociate via long-lived complexes, the product rotational distributions are influenced by the vibrational structure, molecular geometry, coupling of the metastable state, and by dynamical effects in the exit channel arising from anisotropy of the potential energy surface.[69] By measuring the SO product state distributions as a function of $\widetilde{C}$ state internal energy, we seek to gain insight into the coupling mechanisms that lead to SO_2 dissociation near threshold and the dynamics of metastable electronic states.

For these experiments, we couple a pulsed UV light source with an output that can be tuned from 212 nm to 220 nm with a high-resolution transient IR absorption spectrometer and use this instrument to measure the nascent SO(v=0) and SO(v=1) products as a function of photolysis wavelength. Here we focus on dissociation of the main $^{32}S^{16}O_2$ isotopologue. Five photolysis wavelengths are used in this study, corresponding to peak absorption features in SO_2 absorption at 296 K. The energy-dependent measurements start near the dissociation threshold at $\lambda = 220$ nm and extend through 5000 cm^{-1} of internal energy in the $\widetilde{C}$ state.

Here, we report the nascent rotational distributions for SO(v=0) and (v=1) products. The total product energies range from 266 cm^{-1} to 2270 cm^{-1} for these photolysis wavelengths used. We first measure nascent Doppler profiles for individual SO(v=0) product states to determine the initial vibrational energy of SO_2, based on the product velocity distributions and conservation of energy. Then, we measure energy-dependent rotational distributions for the three spin-rotation manifolds of SO(v=0). The energy

partitioning between rotation and translation is determined from these measurements. Potential energy curves for SO_2 dissociation are presented and used to discuss implications on the dissociative coupling mechanism. The energy-dependent appearance of individual $SO(v=0)$ product states is further investigated by measuring action spectra over the full photolysis wavelength range used here and scanning through the threshold for the $SO(v=1)$ product channel. Finally, the onset of the $SO(v=1)$ product channel, and its nascent energy distribution are reported.

5.2 Experimental

5.2.1 High-Resolution Transient IR Spectrometer for SO_2 Photodissociation

The experiments were performed using a high-resolution transient IR absorption spectrometer coupled to a tunable, pulsed UV light source, shown schematically in Figure 5.2. The key components are a Nd:YAG-pumped optical parametric oscillator (OPO), a single-mode IR lead-salt diode laser with high-resolution output at $\lambda \approx 4.4$ μm, and a 300-cm long Pyrex photolysis cell. The OPO provides tunable, pulsed UV light for SO_2 photolysis; for this study, we used the wavelength range 212 nm to 220 nmf. The SO ($v=0$) and ($v=1$) products were detected with state-resolved transient IR overtone absorption probing. Light from the OPO and the IR laser were propagated collinearly through the photolysis cell. Both light sources are linearly polarized. The SO_2 pressure was 20 mTorr at 296 K under constant flow conditions and the average time between SO/SO_2 collisions was approximately 3 μs. Transient SO signals were averaged $t = 0.5$ to 0.7 μs following UV pulses. $SO_2(\widetilde{X} \leftarrow \widetilde{C})$ fluorescence was collected with a photodiode adjacent to the photolysis cell.
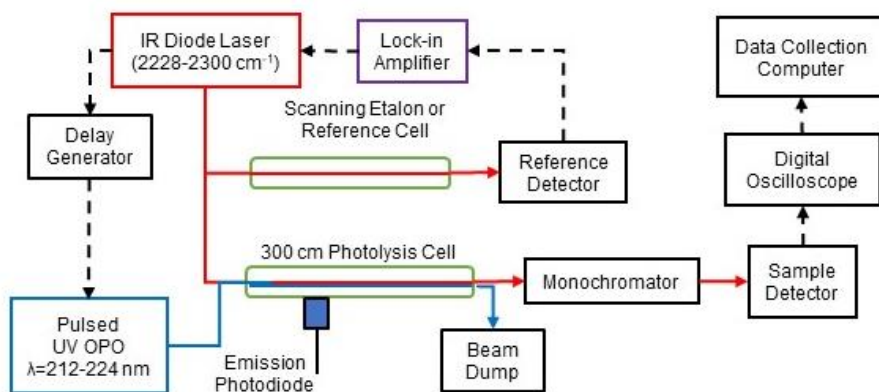
Figure 5.2. Schematic of the tunable UV high-resolution transient IR absorption spectrometer. A pulsed OPO initiated SO_2 predissociation using tunable light (λ = 212 to 220 nm). The IR diode laser probed nascent SO states with IR overtone absorption.

The OPO (Continuum Horizon) was pumped at 10 Hz by the third harmonic (355 nm) of a Nd:YAG laser (Continuum Powerlite DLS). The OPO has a tunable output from 193 nm to 2700 nm with a pulse width of 5 to 7 ns. For the wavelength range used here (212 nm to 220 nm), the spectral resolution was $\Delta\lambda_{UV}$ = 0.05 nm ($\Delta\nu_{UV} \approx 10$ cm^{-1}) and the pulse energy was between 3 and 5 mJ. A mechanical shutter reduced the UV repetition rate to 1 Hz to allow the sample cell to refresh between UV pulses.

The IR diode laser (Laser Components) was used to detect nascent SO products with state-resolved IR overtone transitions. The diode laser has tunable output near $\lambda \sim$ 4.4 μm and a spectral resolution of $\Delta\nu_{IR}$ = 0.0003 cm^{-1}. Transient absorption signals were collected on an InSb detector (Teledyne-Judson Technologies) with a 300-ns-rise-time amplifier (Perry Amplifier). IR wavelength control was achieved by modulating the IR light at 1 kHz and locking the IR wavelength to a fringe of a tunable Fabry-Perot etalon

with a lock-in amplifier (Stanford Research Systems). Known CO_2 and N_2O transitions were used for locating SO IR probe transitions.

Transient fractional IR absorption signals for the SO products were collected by simultaneously measuring IR absorption (ΔI) and transmitted (I_t) intensities on a 4-channel 200 MHz digital oscilloscope (LeCroy) and averaging over 100 UV laser pulses. The signals were transferred to a data acquisition computer using LabVIEW code. The fractional IR absorption was obtained from signal ratios ($R = \Delta I / I_t$) using $\Delta I / I_0 = R/(R + 1)$.

5.2.2 Initiating SO_2 Photodissociation and Probing Nascent $SO(v)$ Products

At 296 K, SO_2 has a structured UV absorption spectrum from 165 nm to 240 nm that includes hot band transitions that originate from the 518 cm^{-1} bend of SO_2 (010).[24] Photolysis of SO_2 $\left(\tilde{C}\ ^1B_2\right)$ was initiated with tunable UV light with wavelengths between 212 nm and 220 nm.

$$SO_2\left(\tilde{X}\ ^1A_1, 296\ K\right) + h\nu\ (\lambda = 212 - 220\ nm) \longrightarrow SO_2\left(\tilde{C}\ ^1B_2\right) \tag{5.1}$$
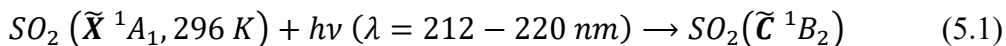
The dissociation products are $SO(\ ^3\Sigma^-)$ and $O(\ ^3P_J)$.

$$SO_2\left(\tilde{C}\ ^1B_2\right) \longrightarrow SO\left(\ ^3\Sigma^-, v, N, J, vel\right) + O\left(\ ^3P_J\right) \tag{5.2}$$
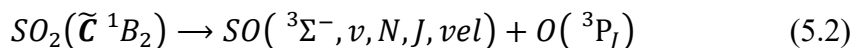
Here, v is the vibrational quantum number, N and J are the rotational and angular momentum quantum numbers, respectively, and vel is the fragment velocity. The appearance of $SO(v=0)$ and $(v=1)$ product states was measured in these experiments. The onset of the $SO(v=1)$ product channel at 296 K occurs at $\lambda = 214.8$ nm for vibrationless SO_2 (000) and at $\lambda = 217.1$ nm for SO_2 (010) hot band absorption.

The SO (v=0) and (v=1) product states were measured by absorption of IR overtone transitions

$$SO\left({}^3\Sigma^-, v, N, J, vel\right) + h\nu \ (\lambda \approx 4.4 \ \mu m) \longrightarrow SO\left({}^3\Sigma^-, v+2, N \pm 1, J \pm 1, vel\right) \quad (5.3)$$
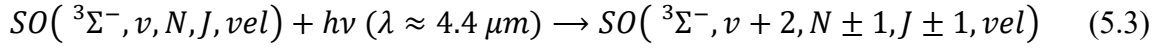
Figure 5.3a illustrates three P-branch transitions for the N=18 rotational sublevels of SO(v). Each SO rotational state N is split into three J states by spin-rotation coupling, with $J = N + 1$, N, and $N - 1$ corresponding to the F_1, F_2, and F_3 spin manifolds, respectively. Frequencies for state-resolved SO$\left({}^3\Sigma^-, v\right)$ overtone transitions with $N \leq 32$ were reported previously by Burkholder et al.[70] Transition frequencies were determined for states up to N=36 based on their spectral constants. The IR overtone transitions centered at 2260 cm^{-1} are a factor of 18 weaker than the fundamental transitions at 1140 cm^{-1}, but the amplifiers for InSb detectors used for overtone detection have advantages for fractional absorption measurements. The list of overtone transitions was augmented with published microwave data and is provided in Appendix C.
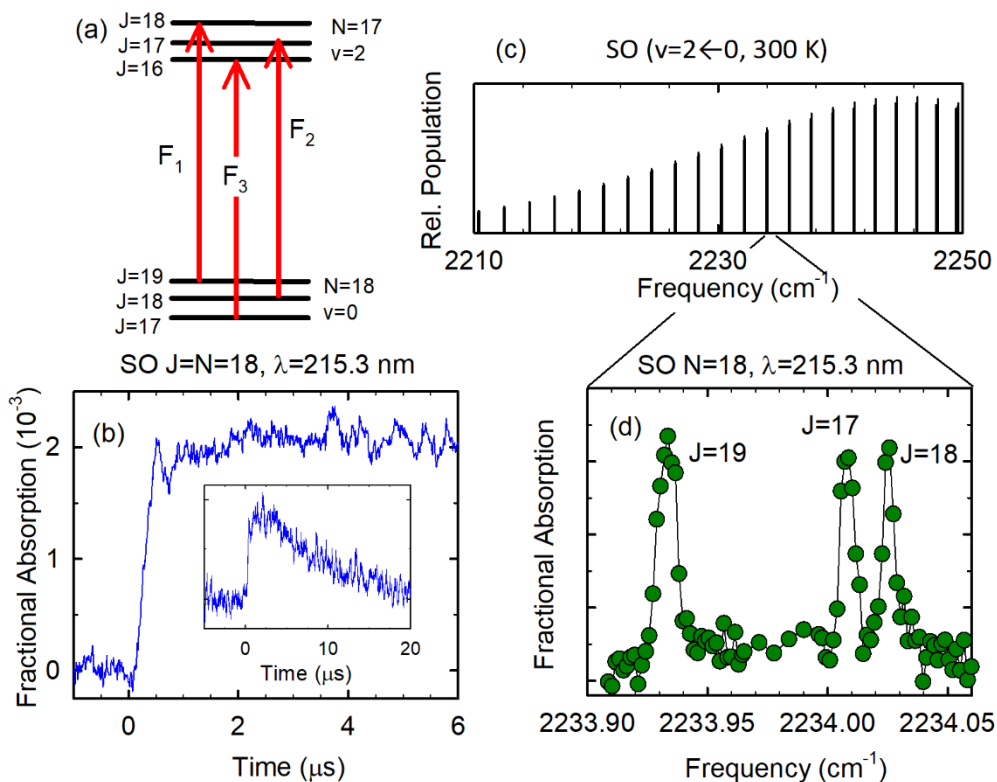
Figure 5.3. (a) Energy levels and transitions involved in probing SO($v=0$) products (not drawn to scale). (b) Transient IR absorption signal for SO($v=0$) $J = N = 18$ following SO$_2$ photolysis at 215.3 nm. The inset shows the long-time decay. (c) The F_2 component of the P-branch SO($v=0$) overtone absorption spectrum at 296 K. (d) Transient IR absorption spectrum (at $t = 0.5$ μs) for the $N = 18$ spin-rotation states of SO($v=0$) products following SO$_2$ dissociation at 215.3 nm.

Transient IR absorption signals for individual SO($v=0$) spin-rotation states with 6 $\leq N \leq 36$ were collected following SO$_2$ photolysis. Figure 5.3b shows the fractional transient IR absorption (at line center) for SO($v=0$) $J = N = 18$ products of 215.3 nm photolysis. The transient signals are prompt relative to the 300 ns detector response time and remain constant for several μs before the photoproducts undergo collisional relaxation, subsequent reactions, and/or diffusion. Figure 5.3c shows the P-branch overtone stick spectrum at 296 K. Figure 5.3d shows the transient IR spectrum (at $t = 0.5$ μs) of SO($v=0$)

N=18 (for SO$_2$ photolysis at 215.3 nm), where the F_1, F_2, and F_3 spin components are clearly resolved. Number densities of SO(v) products were determined using IR absorption strengths based on calculated Einstein A coefficients.

5.3 Results & Discussion

The SO(v) product state distributions and energy partitioning were measured as a function of internal energy in the SO$_2(\widetilde{C})$ state at five UV wavelengths. Figure 5.4 shows the absorption and fluorescence excitation spectra at 296 K for the SO$_2(\widetilde{C} \leftarrow \widetilde{X})$ band excitation between 212 nm and 224 nm. The onset of predissociation is identified by the reduced emission intensity near 220 nm.[56] The photolysis was measured at five UV wavelengths corresponding to SO$_2$ absorption peaks, shown as vertical lines in Figure 5.4a, at $\lambda = 212.0, 213.7, 215.3, 217.2,$ and 218.9 nm.
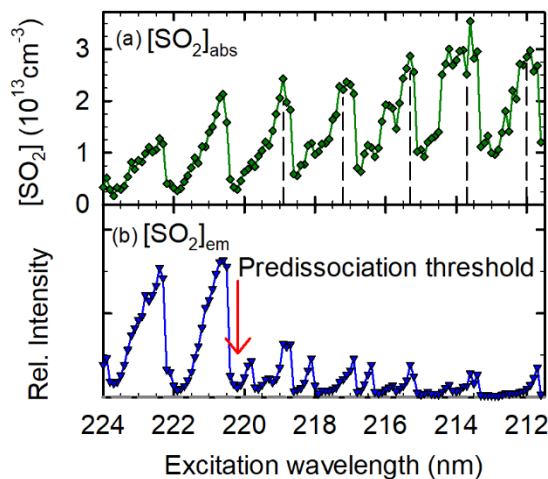
Figure 5.4. (a) Number density of excited SO$_2$ based on UV absorption measurements. (b) SO$_2$ fluorescence excitation spectrum. Vertical lines in indicate UV wavelengths used for discrete energy-dependent SO measurements.

Energy conservation determines the total energy of the photolysis products, E_{pr}:

$$E_{pr} = E_{rot}(SO_2) + E_{vib}(SO_2) + E(hv) - D_0 = E_{int}(SO) + E_{so}(O) + E_{tr} \quad (5.4)$$

At 296 K, the average SO$_2$ rotational energy $E_{rot}(SO_2) = 308$ cm^{-1}. The SO$_2$ vibrational energy $E_{vib}(SO_2)$ is either 0 or 518 cm^{-1}, depending on whether the UV absorption involves a hot band. The UV photon energy is $E(hv)$ and the dissociation energy $D_0 = 45725.3$ cm^{-1}.[71] The combined rotational and vibrational energy of SO is $E_{int}(SO)$, the O-atom spin-orbit energy is $E_{int}(O)$, and the fragment center-of-mass (COM) kinetic energy is E_{tr}. The $O(^3P_J)$ energies are 0, 158, and 227 cm^{-1} for J = 2, 1, and 0, respectively.[72] Elsewhere, (2+1) REMPI studies report that the J=2 ground state is the dominant product, accounting for 91% when the total product energy is E_{pr} = 345 cm^{-1} and 83% when the energy is E_{pr} = 740 cm^{-1}.[71]

In this study, we first establish the total product energy and the O-atom energy by measuring transient Doppler profiles for SO(v=0) products at five photolysis wavelengths. Analysis of the Doppler profiles establishes values of $E_{vib}(SO_2)$, $E_{int}(O)$, and E_{pr}, as defined in Equation 5.4. Then, nascent distributions of SO(v=0) rotational states are reported as a function of internal energy in the SO$_2$($\tilde{C}$) state. From these measurements, we determine the product branching ratios for the spin-rotation manifolds and the rotation-translation branching ratios. UV action spectra were obtained by collecting transient IR absorption measurements for individual SO(v=0) states as the photolysis wavelength was tuned in small wavelength steps over the 212 nm to 220 nm range. Finally, SO(v=1) product states were measured for photolysis at 213.7 nm to estimate the vibrational branching ratio.

5.3.1 Transient Doppler and SO_2 Dissociation Energies

Transient IR Doppler profiles were measured for either the SO($v=0$) F_2 $N = 8$ or 18 state at five photolysis wavelengths to determine the initial $SO_2(\widetilde{X})$ vibrational energy and the spin-orbit energy of the O-atom products. The UV-dependent transient Doppler profiles (at $t = 0.5$ μs) are shown in Figure 5.5. The shapes of the Doppler profiles depend on the experimental geometry, angular distribution of the photoproducts, parent velocity distribution and product relative velocities, as described initially by Zare and Herschbach[32,73] and subsequently used by other groups.[74,75] The photolysis studied here involves a parallel electronic transition, with the IR propagation vector perpendicular to the UV polarization and an isotropic angular distribution of photoproducts. The SO Doppler profiles for these conditions were fit using Equation 2.16 with six possible product velocities, corresponding to $SO_2(\widetilde{X})$ molecules initially in either the (000) or (010) state and the oxygen products in one of the three possible spin-orbit states. The only reasonable fitting results came from assuming that the ground electronic state of the O-atom products with $E_{int}(O)=0$.

a) 218.9 nm, SO (v=0,*N*=8)
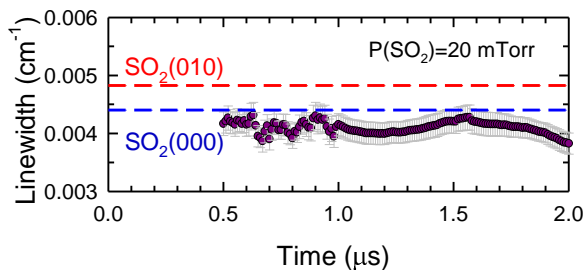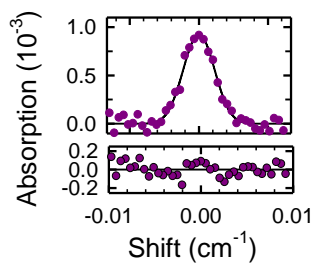
b) 217.2 nm, SO (v=0,*N*=18)
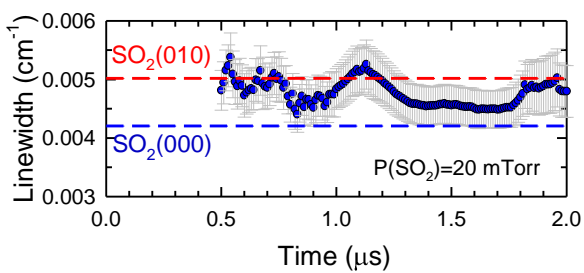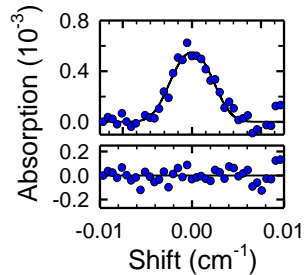
c) 215.3 nm, SO(v=0,*N*=18)
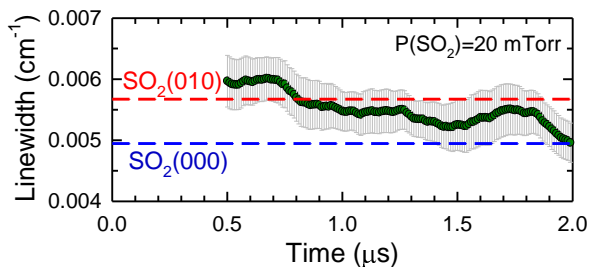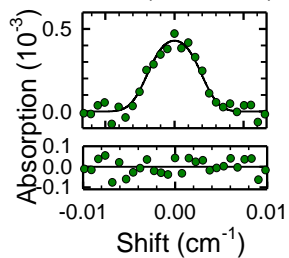
d) 213.7 nm, SO(v=0,*N*=18)
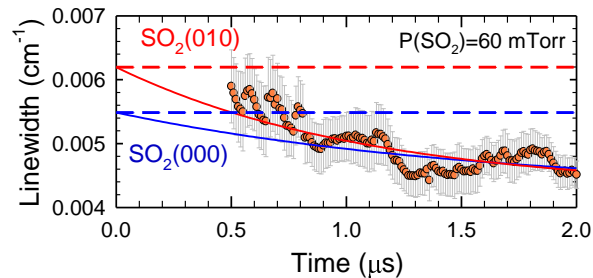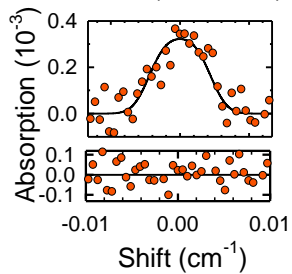
e) 212.0 nm, SO(v=0,*N*=18)
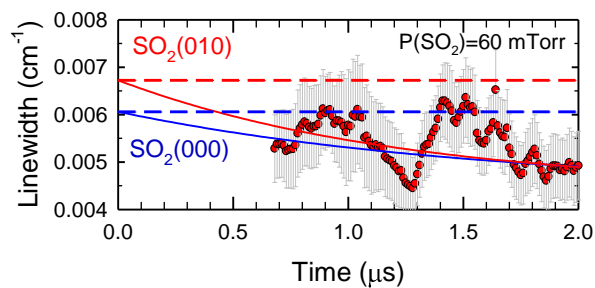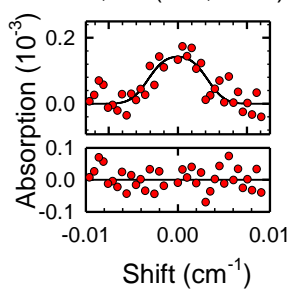
Figure 5.5. Analysis of transient IR Doppler widths for F_2 states of SO(v=0) to determine the initial $SO_2(\widetilde{X})$ vibrational state at five photolysis wavelengths. Data for the three longest UV wavelengths were collected at 20 mTorr under collision-free conditions. Red and blue lines indicate line widths resulting from SO_2 hot band absorption and ground state absorption, respectively. Data for the two shortest UV wavelengths were collected at 60 mTorr and include collisional relaxation decay. Exponential decay fits for collisional relaxation are shown for both SO_2 initial vibrational states.

For three excitation wavelengths, 218.9 nm, 217.2 nm, and 215.3 nm, low-pressure (20 mTorr) collision-free line-profile measurements were performed. The resulting line widths over time are shown as a function of time on the right hand side of Figure 4. Red lines indicate the calculated widths if SO_2 was excited from the (010) state; blue lines show the width for SO_2 excited from the ground vibrationless (000) state. It is clear from Figure 5.5 that 218.9 nm excitation is from the (000) state, and that excitation at 217.2 nm and 215.3 nm involves hot band transitions. Transient absorption signals at 213.7 nm and 212.0 nm were too small to be measured at 20 mTorr. The pressure was increased to 60 mTorr for the line profiles at these excitation wavelengths. The resulting profile widths are shown as a function of time, with an exponential decay corresponding to collisional relaxation of the SO(v=0) collision products. Each time-dependent set of data was fit to two exponential decay functions, corresponding to initial excitation from the SO_2 (000) or (010) state. This analysis shows that the 213.7 nm data come from SO_2 hot band excitation. The analysis of the 212.0 nm data is less clear, given the scatter in the line profile data. However, the fit using the (010) initial SO_2 state is slightly better than that for the (000) state, and we tentatively assign the 212.0 nm data to hot band absorption. It is possible that there are contributions from both the (000) and the (010) states for this data set. The impact of this

assumption will be addressed in later sections. The widths are shown in Figure 5.5 and the resulting energies are listed in Table 5.1.

Table 5.1. Energies (in cm^{-1}) for SO_2 Photodissociation

Excitation (nm)	$E(h\nu)$	$E_{vib}(SO_2)^a$	E_C	$E_{pr}{}^b$
218.9	45683	0	3418	266
217.2	46040	518	4294	1141
215.3	46447	518	4700	1547
213.7	46816	518	5047	1895
212.0	47170	518	5422	2270

[a] Based on fitting transient IR Doppler widths over time.
[b] Using E_{int}(O)=0 based on Doppler fitting results.

The Doppler profiles show that four photolysis wavelengths involve hot band transitions that increase the SO_2 $\widetilde{C}$ state energy by $E_{int}(SO_2) = 518$ cm^{-1}. The $\widetilde{C}$ state internal energy, E_C, is the difference between the excitation energy $\left(E(h\nu) + E_{int}(SO_2)\right)$ and the $\widetilde{X}$-$\widetilde{C}$ term energy of 42573 cm^{-1}.[24] Table 5.1 lists the relevant energies for the wavelength-dependent product state measurements.

5.3.2 SO(ν=0) rotational energy distributions and spin-rotation branching ratios

Nascent SO(ν=0) rotational distributions from SO_2 photolysis were measured as a function of UV wavelength, shown in Figure 5.6 as semi-log plots. Each distribution was measured at least three times. Nascent populations for a number of rotational states between N = 6 and 36 in each spin-rotation manifold were determined from SO(ν=0) transient IR absorption signals (at t = 0.5 μs). The populations include integration over Doppler line profiles. Figure 5.6 also lists the photolysis wavelengths, internal energies in

the $\widetilde{C}$ state (E_C), and total product energies (E_{pr}). At low photolysis energies, the SO(v=0) products are limited to low rotational states by the small values of E_{pr} but as the $\widetilde{C}$ state energy increases, the SO(v=0) products are formed in higher rotational states and the distributions broaden.
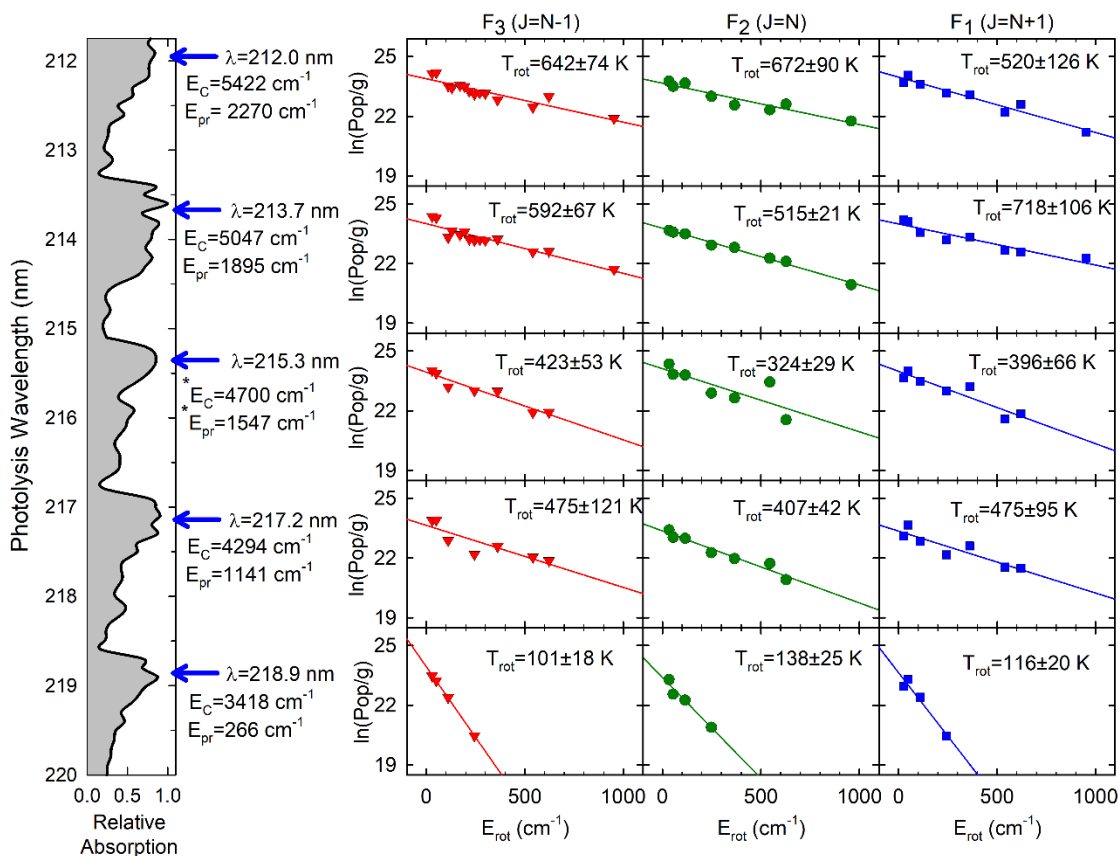
Figure 5.6. Nascent rotational distributions of SO(v=0) F_1, F_2, and F_3 states from SO$_2$ $\widetilde{C}$ state photolysis at five UV wavelengths. The SO$_2$ absorption spectrum is shown on the left, with the excitation wavelengths, internal energy in the $\widetilde{C}$ state (E_C) and the total product energy (E_{pr}).

The rotational distributions in Figure 5.6 were used to determine nascent rotational temperatures T_{rot} for the SO(v=0) products. Figure 5.7a compares the nascent rotational temperatures for the spin-rotation manifolds as a function the total product energy. No

77

substantial differences are seen among the spin-rotational manifolds at a given photolysis energy. The rotational temperatures generally increase as a function of the total product energy, with the exception of the data at E_{pr} = 1547 cm^{-1} which is lower than those at E_{pr} = 1141 cm^{-1}. Each of the three spin-rotation manifolds shows this behavior.
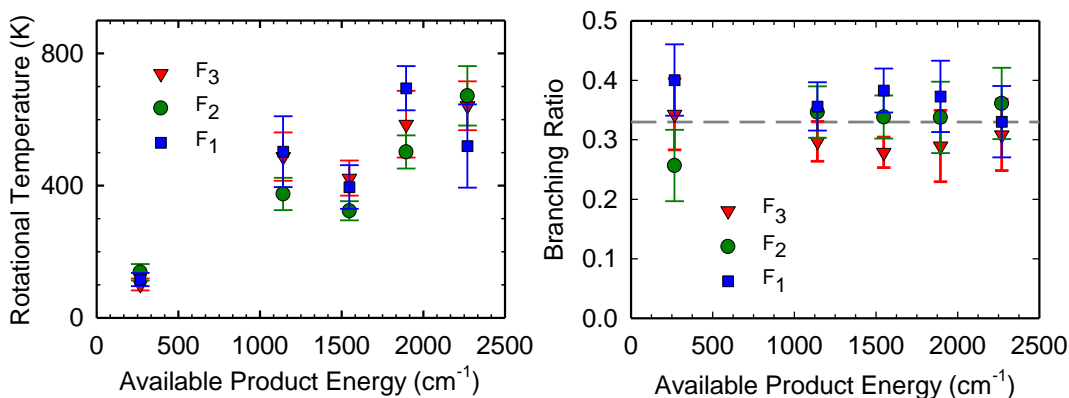
Figure 5.7 (a) Nascent rotational temperatures of SO(v=0) products, based on rotational distributions shown in Figure 5.6. (b) Branching ratios for the SO(v=0) spin-rotation manifolds.

The branching ratios for the SO(v=0) spin-rotation manifolds were determined using the rotational temperatures and absolute number density measurements of a reference state for each spin-manifold. The energy dependence of the product branching ratios is shown in Figure 5.7b. Within experimental uncertainty, the branching ratios are nearly one-third, indicating that the F_1, F_2, and F_3 manifolds are formed with roughly equal probability. In addition, no clear preference is observed for any single spin-rotation manifold. Other studies have reported spin-polarized SO product states for photolysis at λ=193 nm and attributed this observation to coupling of the $\tilde{C}$ state to a repulsive triplet state.[58] However, for SO$_2$ photolysis wavelengths between 212 nm and 220 nm, no clear

differences are seen in the branching ratios of the integrated SO spin component populations or in their energy dependence.

5.3.3 Product Energy Partitioning

Here we consider how the product energy in the SO($v=0$) state is partitioned between rotation and translation and how the energy partitioning depends on the total product energy. The total SO($v=0$) rotational energy is determined using the rotational distributions, based on

$$E_{rot}^{tot} = \sum_J \left(N_J/N_{tot}\right)E_{rot,J} = \sum_J \left(g_J e^{-E_{rot,J}/k_B T_{rot}}/Q_{rot}\right)E_{rot,J} \tag{5.5}$$

where g_J is the degeneracy of the J rotational state, $E_{rot,J}$ is the energy of the J state, k_B is the Boltzmann constant, T_{rot} is the nascent rotational temperature and Q_{rot} is the rotational partition function at T_{rot}. The total translational energy is determined using

$$E_{tr}^{tot} = E_{pr} - E_{rot}^{tot} \tag{5.6}$$

Figure 5.8a shows the rotational and translational energy partitioning for the SO($v=0$) products as a function of E_{pr} for the three spin-rotation manifolds. The total rotation and translation energies increase with E_{pr}. The slopes of E_{rot}^{tot} values as a function of E_{pr} for the three manifolds are 0.16 for F_1, 0.17 for F_2, and 0.18 for F_3, indicating that, on average, 16-18% of the available product energy is in rotation and 82-84% is in translation, for the range of E_{pr} values investigated. Assigning the 212.0 nm excitation to the ground state SO$_2$ absorption changes the percentages slightly to 21% and 79%.
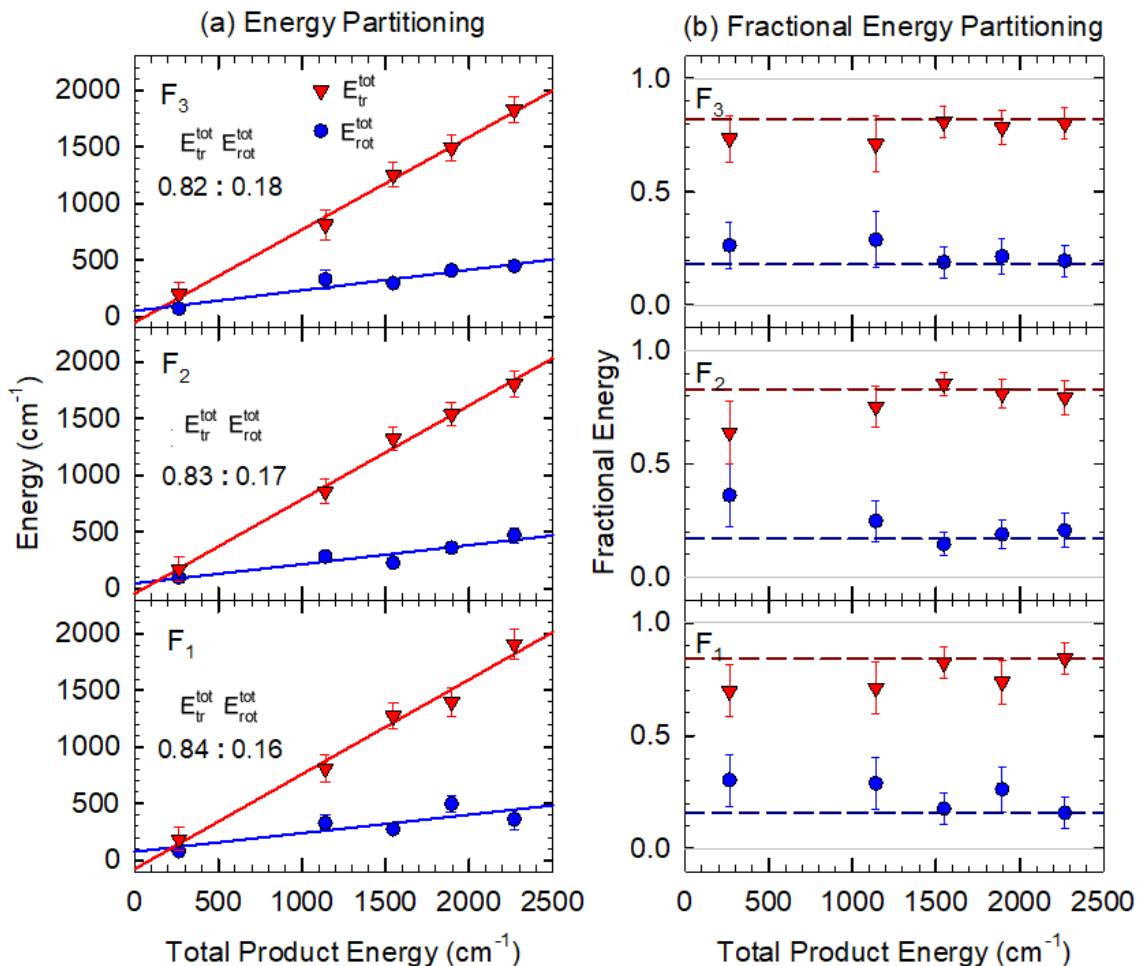
Figure 5.8 Energy partitioning of the SO(v=0) spin manifolds as a function of total product energy. (a) Total rotational (blue circles) and translational energies (red triangles) show that approximately 17% of the product energy is rotation and 83% is translation. (b) The fractional energy partitioning at specific E_{pr} values along with the average values.

The predominance of translational energy in the SO(v=0) products indicates that SO$_2$ stretching modes are important in the predissociation dynamics at the photolysis wavelengths in this study. If SO$_2$ bending modes were significantly populated in the $\widetilde{C}$ prior to dissociation, the SO products are expected to have a significantly larger fraction of rotational energy than is observed. Our results are consistent with recent theoretical calculations that find the UV absorption features at 218.9 nm, 217.2 nm, and 215.3 nm

correspond to $\widetilde{C}$ state vibrational states with quanta in the (symmetric stretch, bend, antisymmetric stretch) modes of (1,1,4), (0,1,8), and (2,0,4), respectively. The corresponding values of E_{pr} are 266, 1141, and 1547 cm^{-1}. Assignments are not reported for the higher energy absorption features.

The overall similarity in energy partitioning for the three spin-rotation manifolds of SO indicates that the electronic coupling matrix elements for predissociation are not strongly dependent on the SO spin-rotation coupling. This finding is consistent with our observation that branching ratios of the spin-rotation manifolds are near one-third, as reported in the previous section. The predominance of product translational energy over rotation highlights the impulsive forces present in the dissociation transition state, and points to a repulsive state as a likely candidate for the non-adiabatic coupling that leads to dissociation.

Figure 5.9a shows the $\widetilde{C}$ state minimum energy path along the Jacobi R coordinate, based on MRCI calculations of potential energy surfaces that are minimized with respect to the Jacobi angle. The bottom plot of Figure 5.9a shows that the SO$_2$ bond angle goes to a linear configuration at the SO$-$O Jacobi distance R corresponding to the dissociation barrier. Figure 5.9b shows the potentials and coupling as described in Figure 5.1 but at a fixed linear geometry. The repulsive triplet state (shown in green) crosses with the $\widetilde{C}$ state near threshold energy for dissociation. Coupling to a repulsive state with a linear geometry is consistent with product translational energy being preferred in a 4:1 ratio of rotational energy.
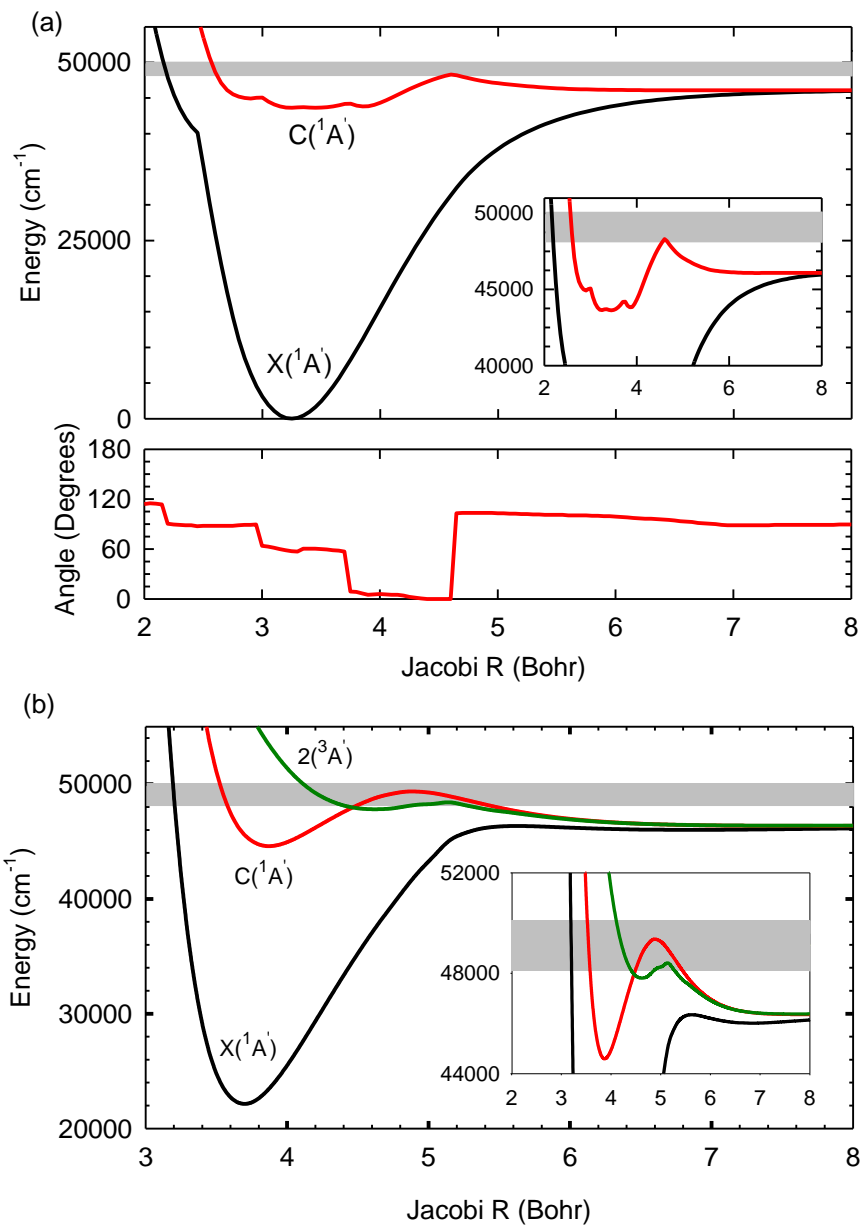
Figure 5.9 (a) The minimum energy curve for the $SO_2(\widetilde{C})$ state dissociation. based on the nonadiabatic coupling described in Figure 5.1. The excitation energy range in shown in gray. The lower plot shows the SO_2 bond angle as function of the distance R for the minimum energy curve. The SO_2 is bent at the bottom of the $\widetilde{C}$ state and linear at the barrier. The grey band indicates the experimental excitation energies. (b) The potential curves at a fixed near-linear geometry with coupling described in Figure 5.1. The repulsive triplet state (in green) crosses the $\widetilde{C}$ state near the dissociation threshold.

82

5.3.4 UV Wavelength-Dependent Action Spectra

To investigate the energy dependence of SO_2 predissociation further, we measured dissociation action spectra for $SO(\nu=0)$ product states as a function of UV wavelength to identify if rotational states and spin-rotation manifolds show any differences and to characterize the onset of the $SO(\nu=1)$ product channel. For a 296 K SO_2 sample, the threshold wavelength for the $SO(\nu=1)$ product channel is 214.8 nm if the absorption starts with $SO_2(000)$; if hot band absorption from $SO_2(010)$ is involved, the threshold is 217.1 nm. Action spectra were collected by measuring transient IR absorption signals for individual $SO(\nu=0)$ product states as the UV wavelength was tuned quasi-continuously in steps of $\Delta\lambda = 0.1$ nm from 211.5 nm to 221 nm. The action spectra are compared to the number density of dissociating SO_2 molecules at each wavelength. Additionally, the appearance of several $SO(\nu=1)$ product states was measured with transient IR probing following 213.7 nm excitation of SO_2, providing a measure of the branching ratio for the $SO(\nu=0)$ and $(\nu=1)$ product states and the energy partitioning in the $SO(\nu=1)$ state.

The energy-dependent number density of SO_2 molecules that dissociate at specific UV wavelengths was determined by the UV absorption spectrum and the dissociation quantum yield Φ_d. Wavelength-dependent values of Φ_d were determined using the absorption and fluorescence excitation spectra shown in Figure 5.4 in conjunction with

$$\Phi_d = 1 - \frac{[SO_2]_{em}}{[SO_2]_{abs}} = 1 - \gamma \frac{I_{em}}{[SO_2]_{abs}} \tag{5.7}$$

Here, $[SO_2]_{abs}$ is the number density of SO_2 molecules that are excited, $[SO_2]_{em}$ is the number density of molecules that fluoresce, and γ is a scaling factor that relates the relative

emission intensity I_{em} to $[SO_2]_{em}$. The value of γ was determined using our data in Figure 5.4 and the quantum yield of Φ_d=0.13 at 222.4 nm reported by Abu-Bajeh, et al.[76] The dissociation quantum yields for λ=212-220 nm are shown in Figure 5.10a. Our values are within 3% of those of Hui and Rice at λ=215.2, 216.9 and 218.8 nm.[64] The number density of dissociating SO_2, $[SO_2]_d$, was determined using $[SO_2]_d = \Phi_d[SO_2]_{abs}$. The UV dependence of $[SO_2]_d$ is also shown in Figure 5.10a.
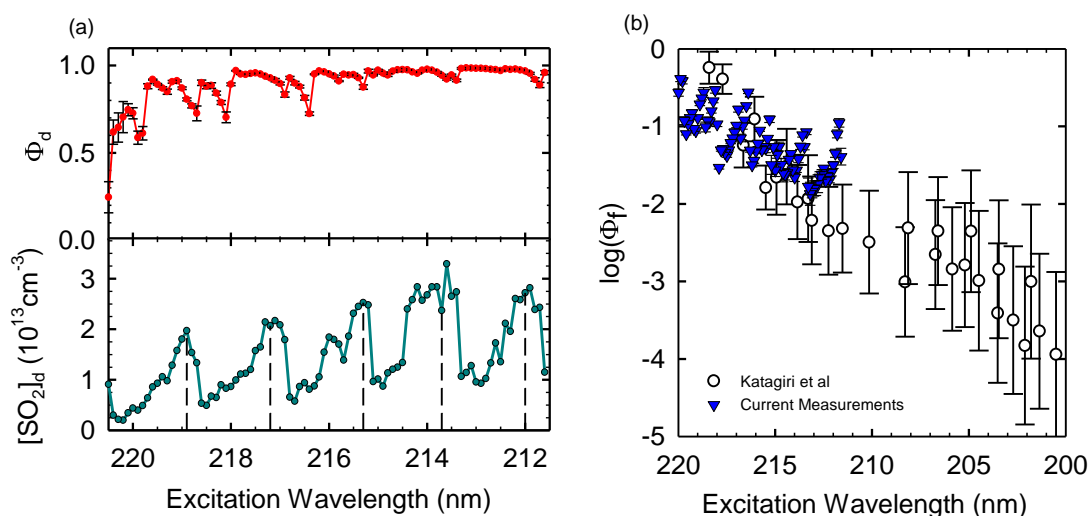
Figure 5.10. (a) Quantum yield Φ_d for SO_2 dissociation at 296 K is in red, based on absorption data, scaled fluorescence data, and the published quantum yield at 222.4 nm. Number density of dissociating SO_2 as a function of UV wavelength is in teal. Vertical lines correspond to the UV wavelengths used in Figure 5.6. (b) The $\log_{10}$ of our fluorescence quantum yield (blue) is compared to previous measurements by Katagiri et al (white).

The structure in the dissociation quantum yield spectrum shown in Figure 5.10a is reflective of the vibronic structure of the $SO_2(\tilde{C})$ state. The calculated minimum energy curves shown in Figure 5.9 show the likely dissociation transition state near the

dissociation threshold is linear. Individual vibronic modes of the $SO_2(\widetilde{C})$ will have varying average geometries which will affect the likelihood of dissociation vs fluorescence. Vibronic modes that are less linear will not as readily dissociate and therefore have more contribution from fluorescence relaxation. In Figure 5.10b, our measured fluorescence quantum yields are compared to previous work by Katagiri et al[65] and find they are in good agreement. The dramatic change in fluorescence quantum yield at 205 nm is consistent with other tunable measurements in that wavelength regime. Cosofret et al measured product vibrational levels from 202 nm to 207 nm and found a dramatic change in relative populations at 205 nm.[57]

Action spectra were collected near dissociation threshold to determine if there are any significant deviations between the products seen and the parent number density at the threshold for SO(v=1) product states. Action spectra for SO(v=0) F_2 rotational states with $N = 6$, 12, and 18 are shown in Figure 5.11. The action spectra intensities were scaled to the parent number density for comparison purposed using the SO_2 absorption feature at 215 nm. The relative parent number density is shown in grey and the calculated spectrum from Kumar et al is shown in black.[29] Figure 5.11 shows that the $N = 6$, 12, and 18 product states generally track the number density of the parent SO_2. At low photolysis energies near threshold, the IR signals are reduced or missing for the $N = 12$ and $N = 18$ states because of insufficient energy, in agreement with the low rotational temperatures observed at low photolysis energies.
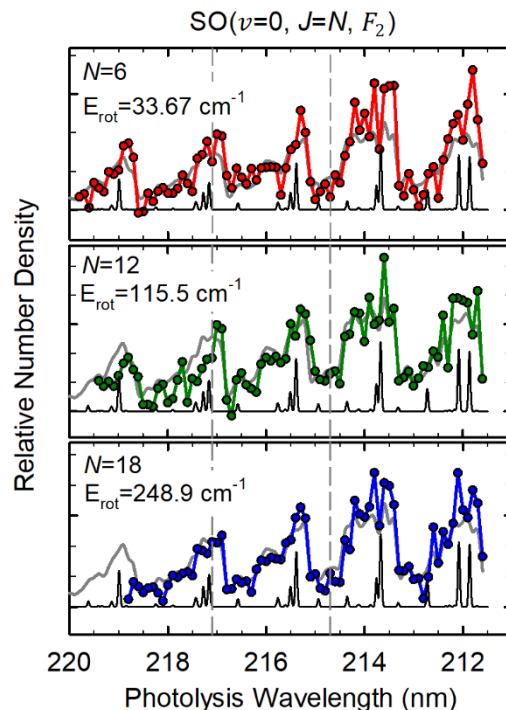
Figure 5.11. Transient IR action spectra (circles) measured at $t = 0.5$ μs for SO(v=0) F_2 product states resulting from SO_2 dissociation. The grey curve is the relative number density of dissociating SO_2. The theoretical SO_2 vibronic transitions from Kumar et al are shown in black.

The spectra in Figure 5.11 do not show significant population changes at the SO(v=1) threshold wavelength(s), indicating that SO(v=1) is a minor product channel over this wavelength range. To check for the presence of SO(v=1) products, transient IR overtone absorption probing was used to measure several SO(v=1) states following SO_2 excitation at 213.7 nm. Figure 5.12a shows the transient absorption signal of SO(v=1) $J = N = 4$. Absorption intensities for the (v=1) state are smaller than those for the (v=0) state by approximately two orders of magnitude. Number densities for SO(v=1) product states with $N = 2$ to 14 were determined at $t = 0.5$ μs and the nascent rotational temperature for the SO(v=1) products is $T_{rot} = 165$ K, based on the semi-log plot shown in Figure 5.12b. The integrated number density of the SO(v=1) products shows that the SO(v=1) channel

86

accounts for only 2% of the dissociation products following excitation with 213.7 nm. Furthermore, the energy partitioning for the SO(v=1) product channel includes a vibrational energy of E_{vib}^{tot}=1138 cm^{-1} with approximate rotational and translational values of E_{rot}^{tot}=120 cm^{-1} and E_{tr}^{tot}=640 cm^{-1}. The SO(v=1) products also have substantially more translational than rotational energy.
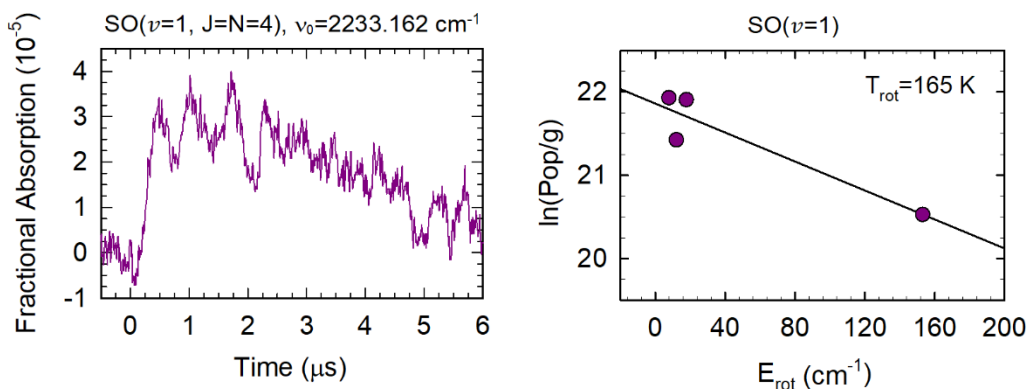
Figure 5.12. (a) Transient IR absorption signal of SO(v=1) $J = N = 4$ products following SO$_2$ photolysis at 213.7 nm. (b) Nascent populations at $t = 0.5$ μs for SO(v=1) states with $J = N = 2, 3, 4$, and 14 have a rotational temperature of $T_{rot} = 165$ K.

Action spectra were additionally collected for the spin-rotation manifolds of SO(v=0) products. Action spectra for the $N = 6$ and 12 states of the F_1, F_2, and F_3 manifolds are shown in Figure 5.13, along with the scaled parent number density. The action spectra generally track the parent number density and the only significant deviations are seen at the lowest photolysis energies for the F_1 states that have slightly higher energies than the related F_2 and F_3 states. These data show that the SO(v=1) product channel has relatively small yield for all three spin-rotation manifolds.
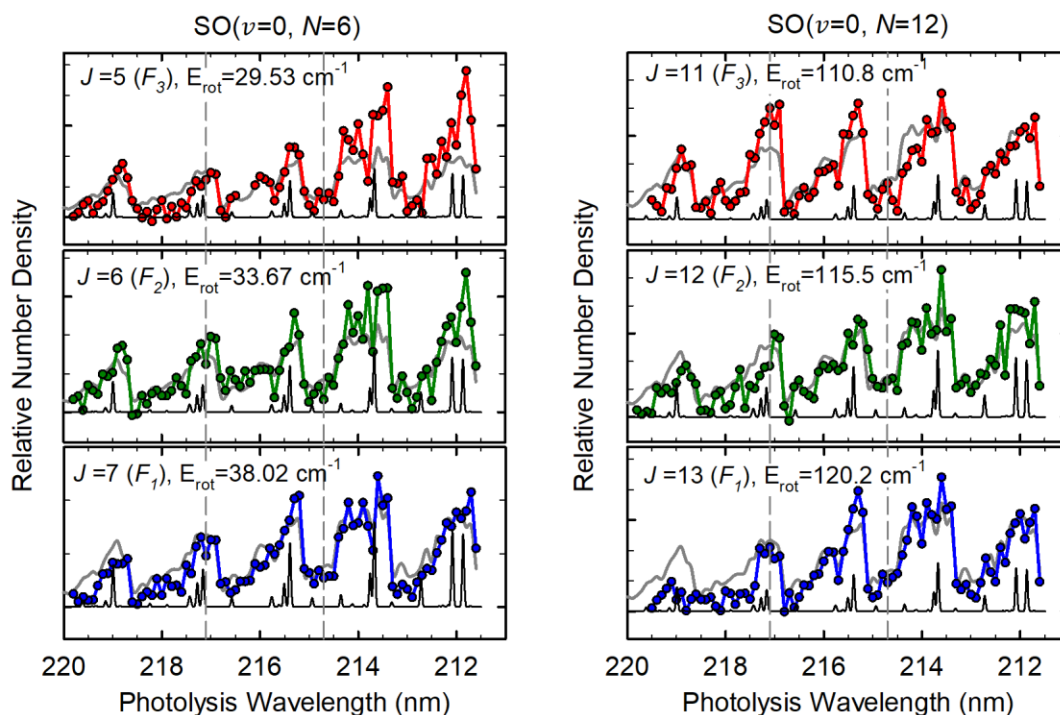
Figure 5.13. Transient IR action spectra at $t = 0.5$ μs for the F_1, F_2, and F_3 components of the SO(v=0) N = 6 and 12 states as a function of UV wavelength collected in steps of $\Delta\lambda = 0.1$ nm. The relative number density of dissociating SO_2 molecules is shown in grey and the theoretical absorption spectrum is shown in black.

Across this wavelength regime, there is no major shift in product state or energy distributions. As shown in Figure 5.9a, the minimum dissociation energy path of the electronic $\widetilde{C}$ state is in a colinear geometry, consistent with our data showing a clear preference for translational product energy in both the SO(v=0) and SO(v=1) product channels.

5.4 Conclusions

High-resolution transient IR absorption spectroscopy was used to investigate the energy-dependence of SO_2 predissociation between 212 and 220 nm by measuring the spin-resolved SO(v=0) and SO(v=1) product state distributions. This range of photolysis

energies yields product energies of the SO diradical up to 2270 cm^{-1}. The energies studied here are just above the dissociation threshold, and calculations of the potential energy curves indicate that the dissociation transition state is linear for these energies. In addition, the $2(^3A')$ repulsive triplet state crosses the $SO_2(\widetilde{C})$ state near threshold.[63]

The rotational distributions show equal partitioning of products into the three F spin-rotation manifolds of $SO(v=0)$. The rotational distributions and analysis of Doppler profiles show that product energy in translation is preferred over rotation with translational energies on average 4 times higher than the total product rotational energy. This preference for translation is observed for the entire range of photolysis wavelengths used and indicates coupling to a repulsive electronic surface immediately prior to dissociation. When the $\widetilde{C}$ state is excited at 215.3 nm ($E_{pr} = 1547$ cm^{-1}), the ratio of translational to rotational product energy increases to value of 6, showing that impulsive forces are particularly strong at this wavelength, suggesting that SO_2 has significant quanta of the stretching mode prior to dissociation.

The photodissociation and fluorescence quantum yield from the $SO_2(\widetilde{C})$ state show a structured spectrum, corresponding to the vibronic structure of the state. Individual SO_2 vibrational state in the $\widetilde{C}$ state will access different regions of the predissociative surface, changing the likelihood of being in a linear geometry that is needed to access the energy barrier at lower excitation energies than for a bent geometry.[65] In addition, our fluorescence quantum yield is in good agreement with other measurements. Both Cosofret et al[57] and Katagiri et al[65] show a dramatic change in their data close to 205 nm excitation, indicating the onset of another dissociation mechanism via coupling to a different repulsive state.

Action spectra were collected for several spin-rotation states of $SO(v=0)$ from 220 to 212 nm. The spectra show no clear preference for any spin-rotation manifold and the signal intensities track with the number density of predissociative SO_2. In addition, there is no significant deviation in signal intensity when $SO(v=1)$ becomes energetically accessible. Exploration of several $SO(v=1)$ states in the F_2 manifold show this channel is 2% of the photodissociation products and there is 5 times the translational energy than rotational energy.

The large preference for translation is found in both $SO(v=0)$ and $SO(v=1)$ product states and there is no preference in the product state spin-rotation manifold. Three mechanisms have been proposed for the photodissociation of SO_2 from the $\widetilde{C}$ state: triplet coupling, singlet coupling, and internal conversion to the $\widetilde{X}$ state. Our data in conjunction with calculated potential energy curves[63] show that $SO_2(\widetilde{C})$ near threshold most likely couples to a repulsive triplet state to photodissociate at excitation energies near the dissociation threshold.

Chapter 6: Conclusions and Future Studies

The work presented in this thesis explores what happens to molecules when they are put in extreme energy states. The studies here fall into two categories. The first set of experiments presented explore how aromatic molecules that are prepared with extreme amounts of vibrational energy ($E_{vib} \sim 40000$ cm^{-1}) relax through collisions with thermal molecules. The second focuses on the photodissociation of SO_2 following electronic excitation with tunable UV light.

All of the work utilizes state-resolved high-resolution transient IR absorption spectroscopy. For the results presented in Chapters 4 and 5 a new spectrometer was constructed with a Pb-salt diode probe laser, a pulsed OPO with tunable UV output, and a 3-m flowing-gas cell. This state-resolved technique allows for the measurement of nascent collision and dissociation product state distributions.

In Chapter 3, product state distributions of NH_3(0000) after collisions with vibrationally hot pyrazine ($E_{vib} = 37900$ cm^{-1}) are reported. The translational energies of the products decrease as J increases, which shows there is a limit on the energy going into the V-RT pathway. NH_3 gains little rotational energy and the rotational temperature was found to be $T_{rot} = 480\pm80$ K. Small gains of limited energy in V-RT indicates NH_3-pyrazine collisions are impulsive. In comparison, CO_2-pyrazine collisions were previously found to involve multiple contacts during each collision, gaining energy with each contact. Measurement of total appearance ($k_{app} = 4.0 \cdot 10^{-10}$ cm^3 molec^{-1} s^{-1}) and depletion ($k_{dep} = 7.6 \cdot 10^{-10}$ cm^3 molec^{-1} s^{-1}) rate constants imply there is significant contribution from the V-V pathway. There is a factor of two difference between the appearance and depletion rate

constants which means about half of the molecules are scattered through collisions in the V-V pathway.

From the collisional energy transfer results presented in Chapter 3, potential studies to further probe deactivation of pyrazine arise. The NH_3-pyrazine(E_{vib} = 37900 cm^{-1}) results clearly show significant contribution from the V-V pathway. State resolved measurement of the NH_3(0100) collision products would answer how the energy is partitioned within the V-V pathway: would the same energy constraint be seen, and what type of collisions result in vibrational energy gain? Other bath molecules with hot pyrazine provide clues as to how properties of the energy acceptor affect collisional energy transfer. The impulsive nature of NH_3-pyrazine collisions may be due to ammonia's lighter mass compared to other molecules studied. CO_2 is much heavier and was found to collide with pyrazine through chattering, multiple-contact collisions thereby gaining more energy. Experiments with SO_2-pyrazine collisions would provide insight into how dipole moment, near resonant vibrational modes, and mass affect the V-RT and V-V pathways. SO_2 has a similar dipole moment to NH_3 and vibrational modes close to those found in pyrazine, both of which might contribute to enhancement of the V-V pathway. [77,78] However, it is more massive than CO_2. The slower velocity would allow for a longer interaction time and chattering collisions as seen with CO_2 collisions, potentially increasing the V-RT energy pathway.

In Chapter 4, nascent CO_2 product state distributions were measured following strong collisions with highly vibrationally excited 2,4,6-trimethylpyridine (collidine). The results are compared to previous work measuring CO_2 scattered from collisions with pyridine, 2-methylpyridine (lutidine), and 2,6-dimethylpyridine (picoline). When put into

context, the work presented in this thesis compare how steric hindrance and vibrational state density affect the energy transfer process. Two interesting results are reported. One, the steric hindrance around the point of interaction lowers the translational and rotational energy imparted through collision. Doppler profiles of the CO_2 scattered from 2,4,6-collidine show little translational energy gain, which is similar to 2,6-lutidine despite large differences in state density. The rotational temperatures of the CO_2 scattered from 2,4,6-collidine is $T_{rot} = 537 \pm 31$ K and 2,6-lutidine is $T_{rot} = 528$ K, which are within error. Two, the high-J integrated rate constant greatly increases as the size of the donor molecule increases. Compared to translational and rotational energy gains, the rate constants are less dependent on steric hindrance. The high-J integrated rate for 2,4,6-collidine is 2.5 times that of 2,6-lutidine. Complete characterization of the V-RT pathway of CO_2-collidine collisions by measurement of the low-J CO_2 translational and rotational energy gain would provide insight into how overall size of the donor molecule affects collisions. Tunable UV allows for fine control of the state density and total vibrational energy of the donor. Use of tunable UV to probe a range of vibrational energies of 2,6-lutidine and 2,4,6-collidine would give more clues as to how state density and steric hindrance affect collisional energy transfer.

In Chapter 5, the dissociation dynamics of the $SO_2(\widetilde{C})$ state are explored near the dissociation threshold. Tunable UV (λ = 212 to 220 nm) is used to excite SO_2 to the $\widetilde{C}$ state and the products are probed with SO(v=2←0) and SO(v=3←1) overtone transitions. Nascent product state distributions of the SO(v=0) diradical photoproducts are measured for five discrete photolysis wavelengths. Doppler profiles were used to determine the total product energy and show that the translational energy is a much larger component than

rotational energy for the SO(v=0) products. More energy into translation indicates that the surface of the $\widetilde{C}$ state prior to dissociation is repulsive in nature. There are equal one-third fractional populations of products in each F spin-rotation manifold. Action spectra signal intensity track with the number density of photodissociating SO_2. There is no apparent difference in F spin-rotation manifold population and at the onset of the SO(v=1) there is no significant change in SO(v=0) signal. Exploration of the SO(v=1) products reveal that this product pathway accounts for 2% of the dissociation. A rotational distribution of states reveals that the translational energy component is larger than rotation for the SO(v=1) products as well. More translational energy, low amounts of SO(v=1) products, and equal partitioning of F sublevel population indicate $SO_2(\widetilde{C})$ couples to a repulsive triplet to dissociate.

More fully characterizing the SO(v=1) products would provide a clearer picture of the branching ratios and dissociation pathway. These also studies focused on the SO products near photodissociation threshold with λ = 212 to 220 nm light. Little work has explored excitation wavelengths between 200 nm and 210 nm and there are more accessible vibrational modes of the SO products. The photodissociation mechanism changes with wavelength and the product state distributions would provide interesting results to compare with other methods. For these studies, fundamental SO(v=2←1) transitions would likely have to be employed which would necessitate new detectors and IR sources for that regime.

Appendix A: Calculation of Lennard-Jones Collision Rate Constants

The Lennard-Jones appearance rate constants presented in this thesis were calculated using the form from Ref. 20.

$$k_{LJ} = \pi \left(\tfrac{1}{2}(\sigma_1 + \sigma_1)\xi^{-1/8} \right)^2 \sqrt{\frac{8k_B T}{\pi\mu}} \left(\frac{2\xi^2(\varepsilon_1\varepsilon_2)}{k_B T} \right)^{1/3} \Gamma(2/3) \qquad (A.1)$$

Here μ is the reduced mass and σ, ε, and ξ are LJ parameters. The parameters used in this thesis are found in Table A.1.[20,77,81]

Molecule	σ (nm)	ε (K/J)
NH_3	0.290	558
CO_2	0.450	190
Pyrazine	0.535	435
Pyridine	0.601	494.6
Picoline	0.558	466
Lutidine	0.589	468
Collidine	0.616	471

Table A.1 Lennard-Jones Parameters for Selected Molecules

We estimated values for CO_2-collidine parameters based on a polynomial fit of the parameters for the other pyridines and the number of vibrational modes. Extrapolation with this method gives the parameters in the last row of the table. Table A.2 shows the LJ collision rate constants for the systems examined in this thesis.

Table A.2 Lennard-Jones Combined Parameters and Collision Rate Constants

System	σ (nm²)	ε (K²/J²)	ξ	k_{LJ} (cm³ molec⁻¹ s⁻¹)
NH_3-pyrazine	0.825	558	1.001	$7.2 \cdot 10^{-10}$
CO_2-pyridine	1.051	190	1.0043	$7.04 \cdot 10^{-10}$
CO_2-picoline	1.008	435	1.0025	$7.38 \cdot 10^{-10}$
CO_2-lutidine	1.039	494.6	1.0017	$7.94 \cdot 10^{-10}$
CO_2-collidine	1.066	466	1	$8.83 \cdot 10^{-10}$

Appendix B: Calculating Average Energy Per Vibrational Mode

For the aromatic molecules compared in Chapter 3, the average vibrational energy per mode, $< E_{vib} >_i$, following excitation with 266 nm light was calculated. The average vibrational energy per modes allows for the comparison of how the internal energy of the vibrationally hot donor molecules is distributed. The mode frequencies for each molecule were calculated using Gaussian 9. To determine the total vibrational energy available, the photo energy was added to the thermal vibrational energy for each molecule, calculated via

$$E_{vib}(296\ K) = \sum_{i=1}^{DOF}\left(\sum_{v=0}^{\infty} E_{v,i}\ \frac{e^{-E_{v,i}/k_b T}}{Q_{vib,i}} \right) \tag{B.1}$$

Here, v is the vibrational quantum number, i is the index over the vibrational degrees of freedom, and $E_{v,i}$ is the energy for a particular quantum, v, in the vibrational mode, i. $E_{v,i}$ is multiplied by the fractional population in that state to and the resulting energies are added over all quanta of that vibrational state. The resulting energies in each vibrational mode are summed to give the total average thermal vibrational energy. The total energy available was the thermal vibrational energy added to the photon energy of a 266 nm photon. The energies for the various molecules are shown in Table B.1.

Table B.1 Vibrational Energies for Selected Aromatic Molecules

Molecule	$E_{vib}(296\ K)$ (cm^{-1})	$E_{vib}(266\ nm)$ (cm^{-1})
Pyrazine	283	37900
Pyridine	296	37900
Picoline	692	38300
Lutidine	1089	38700
Collidine	1507	39100

The average energy per mode of vibration after excitation was calculated using[15,82]

$$< E_{vib} >_i = \frac{hv_i \sum_{i=1}^{max} v_i\, \rho_{s-1}(E - v_i hv_i)}{\rho_s(E)} \tag{B.2}$$

Here, $\rho_s(E)$ is the state density over all s vibrational modes, $\rho_{s-1}(E - v_i hv_i)$ is that density without the ith mode and energy, v_i is the vibrational quantum number of the particular mode up to the maximum allowed value max, max= E/hv_i. The resulting average energy per vibrational mode for pyridine, picoline, lutidine, and collidine are shown in Figure B.1.
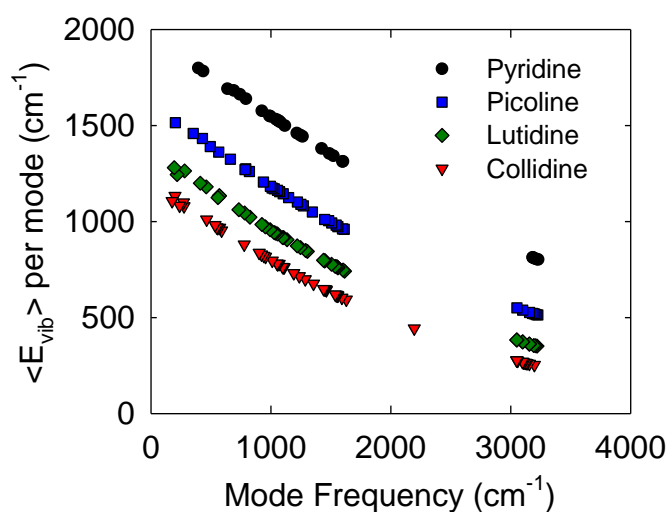
Figure B.1 The average energy per vibrational mode as a function of the particular mode frequency is shown for four molecules, pyridine, picoline, lutidine, and collidine.

97

Appendix C: SO Overtone Spectral Lines

Information on spectral line intensities, Einstein A coefficients, and transition frequencies for SO overtone absorption measurements is given here. The spectral line intensities were determined using calculated Einstein A coefficients based on ab initio electronic structure calculations. The IR overtone transition frequencies originally published Burkholder et al. are expanded to include initial states up to $J = 39$. Values are summarized in tabular form.

A.1 Spectral Line Intensities for SO(v=2←0) Overtone Transitions

The spectral line intensities S were determined using Equation A.1, based on the HITRAN definitions.[30]

$$S = I_a \frac{A}{8\pi c \nu^2} \frac{g' e^{(-E_{rot}/k_B T)}}{Q_{rot} Q_{vib}} \left(1 - e^{(-\nu/k_B T)}\right) \tag{C.1}$$

Here, I_a is the isotopic abundance ($I_a = 0.945687$ for $^{32}S^{16}O$), A is the Einstein coefficient (in s^{-1}), c is the speed of light (in cm s^{-1}) and ν is the transition frequency (in cm^{-1}). The Einstein A coefficients were calculated and provided by collaborators. The upper level degeneracy is g', E_{rot} is the rotational energy for the lower state, and $k_B T$ is thermal energy at 296 K. At 296 K, the rotational partition function is $Q_{rot} = 844$ and the vibrational partition function is $Q_{vib} = 1.004$.

A.2 IR SO(v=2←0) Overtone Transitions

IR transition frequencies for SO(v=0) overtone transitions (up to J = 31) and spectral fitting parameters were reported previously by Burkholder and coworkers.[70] We used their spectral parameters and analytic expressions to calculate SO(v=0) rotational energies and overtone transition frequencies up to N = 39. The calculated transition frequencies have a root-mean square deviation from the observed frequencies of 10^{-3} cm^{-1} or better. Some error was introduced in the low energy states from using the fitting parameters instead of the observed transitions; in this case, the state energies were established using microwave data.[79,80] The A coefficients, rotational energy, degeneracy, line-center transition frequency, and state-specific line intensities are presented in Table C.1 for P-branch and Table C.2 for R-branch.

Table C.1. P-branch Transitions of SO($^3\Sigma^-$, v=2←0): Einstein A Coefficients, Frequencies, and Intensities

v′	J′	N′	v″	J″	N″	A (s^{-1})	E'' (cm^{-1})	g′	ν (cm^{-1})	S (10^{-23} cm/molecule)
2	40	39	0	41	40	0.1601	1182.8031	79	2188.2596	1.22
2	38	39	0	39	40	0.1602	1173.0325	79	2188.2771	1.28
2	39	39	0	40	40	0.1601	1177.9267	79	2188.3340	1.25
2	39	38	0	40	39	0.1606	1125.6589	77	2190.5678	1.58
2	37	38	0	38	39	0.1607	1115.8851	77	2190.5860	1.65
2	38	38	0	39	39	0.1607	1120.7801	77	2190.6426	1.61
2	38	37	0	39	38	0.1612	1069.9293	75	2192.8542	2.02
2	36	37	0	37	38	0.1613	1060.1527	75	2192.8729	2.12
2	37	37	0	38	38	0.1612	1065.0482	75	2192.9294	2.07
2	37	36	0	38	37	0.1617	1015.6151	73	2195.1187	2.56
2	35	36	0	36	37	0.1619	1005.8362	73	2195.1380	2.69
2	36	36	0	37	37	0.1618	1010.7321	73	2195.1942	2.63
2	36	35	0	37	36	0.1623	962.7175	71	2197.3612	3.23
2	34	35	0	35	36	0.1624	952.9368	71	2197.3812	3.39
2	35	35	0	36	36	0.1624	957.8328	71	2197.4371	3.31
2	35	34	0	36	35	0.1628	911.2374	69	2199.5817	4.04
2	33	34	0	34	35	0.1630	901.4554	69	2199.6025	4.24
2	34	34	0	35	35	0.1629	906.3513	69	2199.6581	4.14
2	34	33	0	35	34	0.1634	861.1758	67	2201.7802	5.02
2	32	33	0	33	34	0.1636	851.3932	67	2201.8019	5.27
2	33	33	0	34	34	0.1635	856.2886	67	2201.8571	5.14
2	33	32	0	34	33	0.1640	812.5335	65	2203.9566	6.18
2	31	32	0	32	33	0.1641	802.7509	65	2203.9793	6.49
2	32	32	0	33	33	0.1641	807.6456	65	2204.0341	6.33
2	32	31	0	33	32	0.1645	765.3116	63	2206.1110	7.55
2	30	31	0	31	32	0.1647	755.5297	63	2206.1347	7.93
2	31	31	0	32	32	0.1646	760.4233	63	2206.1890	7.74
2	31	30	0	32	31	0.1651	719.5108	61	2208.2432	9.15
2	29	30	0	30	31	0.1653	709.7305	61	2208.2680	9.61
2	30	30	0	31	31	0.1652	714.6225	61	2208.3219	9.38
2	30	29	0	31	30	0.1656	675.1321	59	2210.3533	11.01
2	28	29	0	29	30	0.1658	665.3541	59	2210.3794	11.56
2	29	29	0	30	30	0.1657	670.2442	59	2210.4327	11.28
2	29	28	0	30	29	0.1662	632.1761	57	2212.4413	13.13
2	27	28	0	28	29	0.1664	622.4014	57	2212.4687	13.79
2	28	28	0	29	29	0.1663	627.2892	57	2212.5214	13.46

100

v′	J′	N′	v″	J″	N″	A (s⁻¹)	E″ (cm⁻¹)	g′	ν (cm⁻¹)	S (10⁻²³ cm/molecule)
2	28	27	0	29	28	0.1668	590.6437	55	2214.5070	15.54
2	26	27	0	27	28	0.1670	580.8734	55	2214.5360	16.32
2	27	27	0	28	28	0.1669	585.7582	55	2214.5880	15.93
2	27	26	0	28	27	0.1673	550.5356	53	2216.5504	18.24
2	25	26	0	26	27	0.1676	540.7708	53	2216.5811	19.16
2	26	26	0	27	27	0.1675	545.6521	53	2216.6324	18.69
2	26	25	0	27	26	0.1679	511.8525	51	2218.5716	21.23
2	24	25	0	25	26	0.1682	502.0945	51	2218.6042	22.30
2	25	25	0	26	26	0.1681	506.9716	51	2218.6547	21.76
2	25	24	0	26	25	0.1685	474.5951	49	2220.5705	24.50
2	23	24	0	24	25	0.1688	464.8453	49	2220.6052	25.74
2	24	24	0	25	25	0.1686	469.7175	49	2220.6547	25.11
2	24	23	0	25	24	0.1691	438.7640	47	2222.5469	28.04
2	22	23	0	23	24	0.1694	429.0239	47	2222.5840	29.45
2	23	23	0	24	24	0.1692	433.8905	47	2222.6324	28.74
2	23	22	0	24	23	0.1697	404.3598	45	2224.5010	31.80
2	21	22	0	22	23	0.1700	394.6313	45	2224.5408	33.41
2	22	22	0	23	23	0.1698	399.4913	45	2224.5879	32.60
2	22	21	0	23	22	0.1703	371.3831	43	2226.4326	35.76
2	20	21	0	21	22	0.1706	361.6682	43	2226.4754	37.57
2	21	21	0	22	22	0.1705	366.5204	43	2226.5211	36.65
2	21	20	0	22	21	0.1709	339.8343	41	2228.3416	39.84
2	19	20	0	20	21	0.1713	330.1353	41	2228.3879	41.87
2	20	20	0	21	21	0.1711	334.9786	41	2228.4320	40.84
2	20	19	0	21	20	0.1715	309.7139	39	2230.2281	43.98
2	18	19	0	19	20	0.1720	300.0335	39	2230.2784	46.22
2	19	19	0	20	20	0.1717	304.8664	39	2230.3205	45.08
2	19	18	0	20	19	0.1722	281.0223	37	2232.0919	48.09
2	17	18	0	18	19	0.1727	271.3634	37	2232.1467	50.55
2	18	18	0	19	19	0.1724	276.1844	37	2232.1867	49.30
2	18	17	0	19	18	0.1728	253.7599	35	2233.9330	52.07
2	16	17	0	17	18	0.1734	244.1261	35	2233.9931	54.75
2	17	17	0	18	18	0.1731	248.9332	35	2234.0304	53.39
2	17	16	0	18	17	0.1735	227.9268	33	2235.7512	55.81
2	15	16	0	16	17	0.1741	218.3222	33	2235.8175	58.70
2	16	16	0	17	17	0.1738	223.1132	33	2235.8518	57.24
2	16	15	0	17	16	0.1742	203.5234	31	2237.5465	59.20

Table S2 *Continued*

v′	J′	N′	v″	J″	N″	A (s⁻¹)	E″ (cm⁻¹)	g′	ν (cm⁻¹)	S (10⁻²³ cm/molecule)
2	15	14	0	16	15	0.1750	180.5496	29	2239.3187	62.12
2	14	15	0	15	16	0.1749	193.9528	31	2237.6200	62.29
2	15	15	0	16	16	0.1746	198.7249	31	2237.6506	60.72
2	13	14	0	14	15	0.1758	171.0189	29	2239.4009	65.38
2	14	14	0	15	15	0.1754	175.7689	29	2239.4270	63.72
2	14	13	0	15	14	0.1758	159.0055	27	2241.0676	64.43
2	12	13	0	13	14	0.1767	149.5215	27	2241.1602	67.84
2	13	13	0	14	14	0.1762	154.2455	27	2241.1809	66.11
2	13	12	0	14	13	0.1766	138.8908	25	2242.7930	66.02
2	11	12	0	12	13	0.1777	129.4619	25	2242.8983	69.56
2	12	12	0	13	13	0.1771	134.1552	25	2242.9122	67.76
2	12	11	0	13	12	0.1775	120.2052	23	2244.4946	66.77
2	10	11	0	11	12	0.1788	110.8418	23	2244.6156	70.41
2	11	11	0	12	12	0.1781	115.4983	23	2244.6210	68.56
2	11	10	0	12	11	0.1785	102.9481	21	2246.1721	66.59
2	10	10	0	11	11	0.1792	98.2752	21	2246.3072	68.40
2	9	10	0	10	11	0.1801	93.6632	21	2246.3127	70.30
2	10	9	0	11	10	0.1796	87.1184	19	2247.8248	65.39
2	9	9	0	10	10	0.1805	82.4862	19	2247.9708	67.21
2	8	9	0	9	10	0.1816	77.9285	19	2247.9907	69.13
2	9	8	0	10	9	0.1809	72.7148	17	2249.4520	63.11
2	8	8	0	9	9	0.1820	68.1316	17	2249.6117	64.92
2	7	8	0	8	9	0.1833	63.6414	17	2249.6510	66.86
2	8	7	0	9	8	0.1823	59.7351	15	2251.0525	59.72
2	7	7	0	8	8	0.1837	55.2117	15	2251.2299	61.51
2	6	7	0	7	8	0.1855	50.8068	15	2251.2961	63.45
2	7	6	0	8	7	0.1841	48.1761	13	2252.6246	55.20
2	6	6	0	7	7	0.1859	43.7267	13	2252.8255	56.96
2	5	6	0	6	7	0.1883	39.4321	13	2252.9305	58.93
2	6	5	0	7	6	0.1862	38.0331	11	2254.1657	49.58
2	5	5	0	6	6	0.1887	33.6769	11	2254.3983	51.31
2	4	5	0	5	6	0.1922	29.5290	11	2254.5618	53.34
2	5	4	0	6	5	0.1890	29.2989	9	2255.6714	42.91
2	4	4	0	5	5	0.1926	25.0624	9	2255.9484	44.63
2	3	4	0	4	5	0.1982	21.1167	9	2256.2049	46.80
2	4	3	0	5	4	0.1929	21.9621	7	2257.1343	35.26
2	3	3	0	4	4	0.1985	17.8834	7	2257.4757	37.00

v'	J'	N'	v"	J"	N"	A (s⁻¹)	E" (cm⁻¹)	g'	ν (cm⁻¹)	S (10⁻²³ cm/molecule)
2	2	3	0	3	4	0.2085	14.2296	7	2257.8919	39.56
2	3	2	0	4	3	0.1988	16.0045	5	2258.5424	26.68
2	2	2	0	3	3	0.2088	12.1401	5	2258.9802	28.56
2	1	2	0	2	3	0.2322	8.9342	5	2259.7215	32.24
2	2	1	0	3	2	0.2091	11.3953	3	2259.8753	17.20
2	1	1	0	2	2	0.2325	7.8325	3	2260.4618	19.45
2	1	0	0	2	1	0.2327	8.0829	1	2261.1045	6.48
2	0	1	0	1	2	0.3449	5.3958	3	2262.9209	29.14

Table C.2. R-branch Transitions of SO($^3\Sigma^-$, v=2←0): Einstein *A* Coefficients, Frequencies, and Intensities

v'	J'	N'	v"	J"	N"	A (s⁻¹)	E" (cm⁻¹)	g'	ν (cm⁻¹)	S (10⁻²³ cm/molecule)
2	2	1	0	1	0	0.1404	4.9830	3	2265.2869	16.70
2	1	2	0	0	1	0.1184	5.9837	5	2263.6727	11.80
2	2	2	0	1	1	0.1406	4.9607	5	2266.1596	19.78
2	3	2	0	2	1	0.1507	8.0829	5	2266.4639	20.87
2	2	3	0	1	2	0.1407	5.3958	7	2266.7258	27.64
2	3	3	0	2	2	0.1509	7.8325	7	2267.5266	29.27
2	4	3	0	3	2	0.1565	11.3953	7	2267.7012	29.84
2	3	4	0	2	3	0.1510	8.9342	9	2268.3874	37.45
2	4	4	0	3	3	0.1567	12.1401	9	2268.8707	38.24
2	5	4	0	4	3	0.1603	16.0045	9	2268.9658	38.38
2	4	5	0	3	4	0.1569	14.2296	11	2269.8611	46.29
2	5	5	0	4	4	0.1606	17.8834	11	2270.1918	46.51
2	6	5	0	5	4	0.1631	21.9621	11	2270.2367	46.30
2	5	6	0	4	5	0.1608	21.1167	13	2271.2458	54.13
2	6	6	0	5	5	0.1633	25.0624	13	2271.4898	53.92
2	7	6	0	6	5	0.1651	29.2989	13	2271.5019	53.41
2	6	7	0	5	6	0.1636	29.5290	15	2272.5739	60.91
2	8	7	0	7	6	0.1668	38.0331	15	2272.7545	59.59
2	7	7	0	6	6	0.1654	33.6769	15	2272.7647	60.36
2	7	8	0	6	7	0.1657	39.4321	17	2273.8603	66.55
2	9	8	0	8	7	0.1682	48.1761	17	2273.9907	64.73
2	8	8	0	7	7	0.1671	43.7267	17	2274.0165	65.72
2	8	9	0	7	8	0.1673	50.8068	19	2275.1124	70.99

v′	J′	N′	v″	J″	N″	A (s⁻¹)	E″ (cm⁻¹)	g′	ν (cm⁻¹)	S (10⁻²³ cm/molecule)
2	10	9	0	9	8	0.1693	59.7351	19	2275.2081	68.78
2	9	9	0	8	8	0.1685	55.2117	19	2275.2452	69.94
2	9	10	0	8	9	0.1687	63.6414	21	2276.3345	74.23
2	11	10	0	10	9	0.1704	72.7148	21	2276.4053	71.70
2	10	10	0	9	9	0.1696	68.1316	21	2276.4508	73.01
2	10	11	0	9	10	0.1699	77.9285	23	2277.5289	76.27
2	12	11	0	11	10	0.1712	87.1184	23	2277.5814	73.51
2	11	11	0	10	10	0.1706	82.4862	23	2277.6331	74.92
2	11	12	0	10	11	0.1709	93.6632	25	2278.6971	77.15
2	13	12	0	12	11	0.1720	102.9481	25	2278.7357	74.23
2	12	12	0	11	11	0.1715	98.2752	25	2278.7922	75.71
2	12	13	0	11	12	0.1717	110.8418	27	2279.8398	76.95
2	14	13	0	13	12	0.1727	120.2052	27	2279.8678	73.93
2	13	13	0	12	12	0.1723	115.4983	27	2279.9281	75.45
2	13	14	0	12	13	0.1725	129.4619	29	2280.9578	75.74
2	15	14	0	14	13	0.1734	138.8908	29	2280.9774	72.70
2	14	14	0	13	13	0.1730	134.1552	29	2281.0407	74.23
2	14	15	0	13	14	0.1732	149.5215	31	2282.0514	73.65
2	16	15	0	15	14	0.1740	159.0055	31	2282.0644	70.62
2	15	15	0	14	14	0.1737	154.2455	31	2282.1300	72.14
2	15	16	0	14	15	0.1739	171.0189	33	2283.1209	70.79
2	17	16	0	16	15	0.1745	180.5496	33	2283.1284	67.84
2	16	16	0	15	15	0.1742	175.7689	33	2283.1960	69.31
2	16	17	0	15	16	0.1745	193.9528	35	2284.1663	67.31
2	18	17	0	17	16	0.1751	203.5234	35	2284.1695	64.45
2	17	17	0	16	16	0.1748	198.7249	35	2284.2387	65.88
2	19	18	0	18	17	0.1755	227.9268	37	2285.1874	60.61
2	17	18	0	16	17	0.1750	218.3222	37	2285.1879	63.32
2	18	18	0	17	17	0.1753	223.1132	37	2285.2579	61.96
2	20	19	0	19	18	0.1760	253.7599	39	2286.1821	56.42
2	18	19	0	17	18	0.1755	244.1261	39	2286.1857	58.97
2	19	19	0	18	18	0.1758	248.9332	39	2286.2538	57.69
2	21	20	0	20	19	0.1764	281.0223	41	2287.1536	52.01
2	19	20	0	18	19	0.1760	271.3634	41	2287.1598	54.39
2	20	20	0	19	19	0.1762	276.1844	41	2287.2262	53.19
2	22	21	0	21	20	0.1768	309.7139	43	2288.1018	47.49
2	20	21	0	19	20	0.1764	300.0335	43	2288.1101	49.68

v′	J′	N′	v″	J″	N″	A (s⁻¹)	E″ (cm⁻¹)	g′	ν (cm⁻¹)	S (10⁻²³ cm/molecule)
2	21	21	0	20	20	0.1767	304.8664	43	2288.1751	48.58
2	23	22	0	22	21	0.1772	339.8343	45	2289.0265	42.97
2	21	22	0	20	21	0.1769	330.1353	45	2289.0368	44.96
2	22	22	0	21	21	0.1771	334.9786	45	2289.1006	43.96
2	24	23	0	23	22	0.1776	371.3831	47	2289.9279	38.53
2	22	23	0	21	22	0.1773	361.6682	47	2289.9398	40.33
2	23	23	0	22	22	0.1774	366.5204	47	2290.0025	39.42
2	25	24	0	24	23	0.1779	404.3598	49	2290.8057	34.24
2	23	24	0	22	23	0.1776	394.6313	49	2290.8191	35.85
2	24	24	0	23	23	0.1778	399.4913	49	2290.8809	35.04
2	26	25	0	25	24	0.1783	438.7640	51	2291.6601	30.17
2	24	25	0	23	24	0.1780	429.0239	51	2291.6747	31.59
2	25	25	0	24	24	0.1782	433.8905	51	2291.7358	30.87
2	27	26	0	26	25	0.1786	474.5951	53	2292.4909	26.36
2	25	26	0	24	25	0.1783	464.8453	53	2292.5067	27.60
2	26	26	0	25	25	0.1785	469.7175	53	2292.5670	26.97
2	28	27	0	27	26	0.1789	511.8525	55	2293.2981	22.83
2	26	27	0	25	26	0.1787	502.0945	55	2293.3149	23.91
2	27	27	0	26	26	0.1788	506.9716	55	2293.3746	23.36
2	29	28	0	28	27	0.1792	550.5356	57	2294.0817	19.61
2	27	28	0	26	27	0.1790	540.7708	57	2294.0994	20.54
2	28	28	0	27	27	0.1791	545.6521	57	2294.1585	20.07
2	30	29	0	29	28	0.1795	590.6437	59	2294.8417	16.71
2	28	29	0	27	28	0.1793	580.8734	59	2294.8601	17.50
2	29	29	0	28	28	0.1794	585.7582	59	2294.9188	17.10
2	31	30	0	30	29	0.1797	632.1761	61	2295.5780	14.12
2	29	30	0	28	29	0.1795	622.4014	61	2295.5971	14.79
2	30	30	0	29	29	0.1797	627.2892	61	2295.6553	14.45
2	32	31	0	31	30	0.1800	675.1321	63	2296.2905	11.84
2	30	31	0	29	30	0.1798	665.3541	63	2296.3103	12.40
2	31	31	0	30	30	0.1799	670.2442	63	2296.3681	12.12
2	33	32	0	32	31	0.1802	719.5108	65	2296.9793	9.84
2	31	32	0	30	31	0.1801	709.7305	65	2296.9997	10.31
2	32	32	0	31	31	0.1802	714.6225	65	2297.0571	10.08
2	34	33	0	33	32	0.1805	765.3116	67	2297.6443	8.12
2	32	33	0	31	32	0.1803	755.5297	67	2297.6653	8.51
2	33	33	0	32	32	0.1804	760.4233	67	2297.7224	8.31

v′	J′	N′	v″	J″	N″	A (s⁻¹)	E″ (cm⁻¹)	g′	ν (cm⁻¹)	S (10⁻²³ cm/molecule)
2	35	34	0	34	33	0.1807	812.5335	69	2298.2855	6.65
2	33	34	0	32	33	0.1805	802.7509	69	2298.3070	6.97
2	34	34	0	33	33	0.1806	807.6456	69	2298.3638	6.80
2	36	35	0	35	34	0.1809	861.1758	71	2298.9029	5.40
2	34	35	0	33	34	0.1808	851.3932	71	2298.9249	5.66
2	35	35	0	34	34	0.1809	856.2886	71	2298.9813	5.53
2	37	36	0	36	35	0.1811	911.2374	73	2299.4964	4.35
2	38	37	0	37	36	0.1813	962.7175	75	2299.4964	3.48
2	39	38	0	38	37	0.1815	1015.6151	77	2299.4964	2.76
2	35	36	0	34	35	0.1810	901.4554	73	2299.5188	4.56
2	36	36	0	35	35	0.1811	906.3513	73	2299.5750	4.45
2	36	37	0	35	36	0.1812	952.9368	75	2300.0888	3.65
2	37	37	0	36	36	0.1813	957.8328	75	2300.1448	3.56
2	37	38	0	36	37	0.1814	1005.8362	77	2300.6349	2.90
2	38	38	0	37	37	0.1815	1010.7321	77	2300.6906	2.83
2	40	39	0	39	38	0.1817	1069.9293	79	2301.1334	2.18
2	38	39	0	37	38	0.1816	1060.1527	79	2301.1570	2.28
2	39	39	0	38	38	0.1816	1065.0482	79	2301.2125	2.23
2	41	40	0	40	39	0.1819	1125.6589	81	2301.6311	1.70
2	39	40	0	38	39	0.1817	1115.8851	81	2301.6551	1.78
2	40	40	0	39	39	0.1818	1120.7801	81	2301.7104	1.74

Bibliography

(1)   Hinshelwood, C. N. On the Theory of Unimolecular Reactions. *Proc. R. Soc. A Math. Phys. Eng. Sci.* **1926**, *113* (763), 230–233. https://doi.org/10.1098/rspa.1926.0149.

(2)   Troe, J. Theory of Thermal Unimolecular Reactions at Low Pressures. II. Strong Collision Rate Constants. Applications. *J. Chem. Phys.* **1977**, *66* (11), 4758–4775. https://doi.org/10.1063/1.433838.

(3)   Hippler, H.; Lindemann, L.; Troe, J. Collisional Energy Transfer of Vibrationally Highly Excited Molecules. V. UV Absorption Study of Azulene. *J. Chem. Phys.* **1985**, *83* (8), 3906–3912. https://doi.org/10.1063/1.449843.

(4)   Miller, L. A.; Barker, J. R. Collisional Deactivation of Highly Vibrationally Excited Pyrazine. *J. Chem. Phys.* **1996**, *105* (4), 1383–1391. https://doi.org/10.1063/1.471996.

(5)   Havey, D. K.; Liu, Q.; Li, Z.; Elioff, M.; Fang, M.; Neudel, J.; Mullin, A. S. Direct Determination of Collision Rates beyond the Lennard-Jones Model through State-Resolved Measurements of Strong and Weak Collisions. *J. Phys. Chem. A* **2007**, *111* (13), 2458–2460. https://doi.org/10.1021/jp0712497.

(6)   Havey, D. K.; Liu, Q.; Li, Z.; Elioff, M.; Mullin, A. S. Collisions of Highly Vibrationally Excited Pyrazine (E_{Vib} = 37 900 cm^{-1}) with HOD: State-Resolved Probing of Strong and Weak Collisions. *J. Phys. Chem. A* **2007**, *111* (51), 13321–13329. https://doi.org/10.1021/jp076023i.

(7)   Havey, D. K.; Du, J.; Liu, Q.; Mullin, A. S. Full State-Resolved Energy Gain Profiles of CO_2 (J = 2−80) from Collisions of Highly Vibrationally Excited Molecules. 1. Relaxation of Pyrazine (E = 37900 cm^{-1})†. *J. Phys. Chem. A* **2010**, *114* (3), 1569–1580. https://doi.org/10.1021/jp908934j.

(8)   Du, J.; Sassin, N. A.; Havey, D. K.; Hsu, K.; Mullin, A. S. Full State-Resolved Energy Gain Profiles of CO_2 from Collisions with Highly Vibrationally Excited Molecules. II. Energy-Dependent Pyrazine (E = 32 700 and 37 900 cm^{-1}) Relaxation. *J. Phys. Chem. A* **2013**, *117* (46), 12104–12115. https://doi.org/10.1021/jp404939s.

(9)   Lin, M. F.; Dyakov, Y. A.; Tseng, C. M.; Mebel, A. M.; Lin, S. H.; Lee, Y. T.; Ni, C. K. Photodissociation Dynamics of Pyridine. *J. Chem. Phys.* **2005**, *123* (5), 054309. https://doi.org/10.1063/1.1994849.

(10)   Sevy, E. T.; Muyskens, M. A.; Rubin, S. M.; Flynn, G. W.; Muckerman, J. T. Competition between Photochemistry and Energy Transfer in Ultraviolet-Excited Diazabenzenes. I. Photofragmentation Studies of Pyrazine at 248 nm and 266 nm. *J. Chem. Phys.* **2000**, *112* (13), 5829–5843. https://doi.org/10.1063/1.481157.

(11)   Lendvay, G.; Schatz, G. C. Choice of Gas Kinetic Rate Coefficients in the Vibrational Relaxation of Highly Excited Polyatomic Molecules. *J. Phys. Chem.* **1992**, *96* (9), 3752–3756. https://doi.org/10.1021/j100188a035.

(12)   Miller, J. A.; Klippenstein, S. J. Master Equation Methods in Gas Phase Chemical Kinetics. *J. Phys. Chem. A* **2006**, *110* (36), 10528–10544. https://doi.org/10.1021/jp062693x.

(13)   Clarke, D. L.; Thompson, K. C.; Gilbert, R. G. Supercollision Events in Weak Collisional Energy Transfer of Highly Excited Species. *Chem. Phys. Lett.* **1991**, *182* (3–4), 357–362. https://doi.org/10.1016/0009-2614(91)80229-Q.

(14)   Yerram, M. L.; Brenner, J. D.; King, K. D.; Barker, J. R. Collisional Deactivation of Highly Vibrationally Excited Benzene Pumped at 248 nm. *J. Phys. Chem.* **1990**, *94* (16), 6341–6350. https://doi.org/10.1021/j100379a036.

(15)   Toselli, B. M.; Barker, J. R. Isotope Effects in the Vibrational Deactivation of Large Molecules. *J. Chem. Phys.* **1992**, *97* (3), 1809–1817. https://doi.org/10.1063/1.463168.

(16)   Doran, J. L.; Hon, B.; Leopold, K. R. Rotational Spectrum and Structure of the Pyridine-CO_2 van Der Waals Complex. *J. Mol. Struct.* **2012**, *1019*, 191–195. https://doi.org/10.1016/j.molstruc.2012.03.039.

(17)   Lee, J. D.; Wallwork, S. C. The Crystal Structure of the 1:1 Complex Formed by 2,6-Lutidine and Urea. *Acta Crystallogr.* **1965**, *19* (3), 311–313. https://doi.org/10.1107/s0365110x65003377.

(18)   Wu, D.; Jia, D.; Liu, L.; Zhang, L.; Guo, J. Reactivity of 2,6-Lutidine/BR_3 and Pyridine/BR_3 Lewis Pairs (R = F, Me, C_6F_5): A Density Functional Study. *J. Phys. Chem. A* **2010**, *114* (43), 11738–11745. https://doi.org/10.1021/jp105000x.

(19)   Elioff, M. S.; Fang, M.; Mullin, A. S. Methylation Effects in State Resolved Quenching of Highly Vibrationally Excited Azabenzenes ($E_{vib} \sim 38500$ cm^{-1}). I. Collisions with Water. *J. Chem. Phys.* **2001**, *115* (15), 6990–7001. https://doi.org/10.1063/1.1400782.

(20)   Park, J.; Shum, L.; Lemoff, A. S.; Werner, K.; Mullin, A. S. Methylation Effects in State-Resolved Quenching of Highly Vibrationally Excited Azabenzenes ($E_{vib} \sim 38500$ cm^{-1}) - II. Collisions with Carbon Dioxide. *J. Chem. Phys.* **2002**, *117* (11), 5221–5233. https://doi.org/10.1063/1.1499720.

(21)   Wall, M. C.; Lemoff, A. E.; Mullin, A. S. Unraveling the Energy Dependence in Large $\Delta E(V \rightarrow RT)$ Energy Transfer: Separation of ΔE and Probability in the Collisional Relaxation of Highly Vibrationally Excited Pyrazine ($E_{vib} = 36\,000$ to $41\,000$ cm^{-1}) by CO_2. *J. Chem. Phys.* **1999**, *111* (16), 7373–7382. https://doi.org/10.1063/1.480060.

(22)   Warneck, P.; Sullivan, J. O.; Marmo, F. F. Ultraviolet Absorption of SO_2 - Dissociation Energies of SO_2 + SO. *J. Chem. Phys.* **1964**, *40* (4), 1132-. https://doi.org/10.1063/1.1725260.

(23)   Yang, T. S.; Myers, A. B. Resonance Raman-Spectra of the $S_3 \leftarrow S_0$ Transition of SO_2-Electronic, Vibrational, and Rotational-Dynamics in Solution. *J. Chem. Phys.* **1991**, *95* (9), 6207–6217. https://doi.org/10.1063/1.461566.

(24)   Danielache, S. O.; Eskebjerg, C.; Johnson, M. S.; Ueno, Y.; Yoshida, N. High-Precision Spectroscopy of ^{32}S, ^{33}S, and ^{34}S Sulfur Dioxide: Ultraviolet Absorption Cross Sections and Isotope Effects. *J. Geophys. Res.* **2008**, *113* (D17), 14. https://doi.org/10.1029/2007jd009695.

(25)   Ivanco, M.; Hager, J.; Sharfin, W.; Wallace, S. C. Quantum Interference Phenomena in the Radiative Decay of the $\tilde{C}$ ($^1B_2$) State of SO_2. *J. Chem. Phys.* **1983**, *78* (11), 6531–6540. https://doi.org/10.1063/1.444692.

(26)   Park, G. B.; Jiang, J.; Saladrigas, C. A.; Field, R. W. Observation of B_2 Symmetry Vibrational Levels of the SO2 ($\tilde{C}$) $^1B_2$ State: Vibrational Level Staggering, Coriolis Interactions, and Rotation-Vibration Constants. *J. Chem. Phys.* **2016**, *144* (14), 13. https://doi.org/10.1063/1.4944924.

(27)   Jiang, J.; Park, G. B.; Field, R. W. The Rotation-Vibration Structure of the SO_2 ($\tilde{C}$)

$^1B_2$ State Explained by a New Internal Coordinate Force Field. *J. Chem. Phys.* **2016**, *144* (14), 20. https://doi.org/10.1063/1.4945621.

(28) Park, G. B.; Womack, C. C.; Whitehill, A. R.; Jiang, J.; Ono, S.; Field, R. W. Millimeter-Wave Optical Double Resonance Schemes for Rapid Assignment of Perturbed Spectra, with Applications to the ($\tilde{C}$) $^1B_2$ State of SO_2. *J. Chem. Phys.* **2015**, *142* (14), 12. https://doi.org/10.1063/1.4916908.

(29) Kumar, P.; Jiang, B.; Guo, H.; Kłos, J.; Alexander, M. H.; Poirier, B. Photoabsorption Assignments for the $\tilde{C}^1B_2 \leftarrow \tilde{X}^1A_1$ Vibronic Transitions of SO_2, Using New Ab Initio Potential Energy and Transition Dipole Surfaces. *J. Phys. Chem. A* **2017**, *121* (5), 1012–1021. https://doi.org/10.1021/acs.jpca.6b12958.

(30) Gordon, I. E.; Rothman, L. S.; Hill, C.; Kochanov, R. V.; Tan, Y.; Bernath, P. F.; Birk, M.; Boudon, V.; Campargue, A.; Chance, K. V.; Drouin, B. J.; Flaud, J. M.; Gamache, R. R.; Hodges, J. T.; Jacquemart, D.; Perevalov, V. I.; Perrin, A.; Shine, K. P.; Smith, M. A. H.; Tennyson, J.; Toon, G. C.; Tran, H.; Tyuterev, V. G.; Barbe, A.; Császár, A. G.; Devi, V. M.; Furtenbacher, T.; Harrison, J. J.; Hartmann, J. M.; Jolly, A.; Johnson, T. J.; Karman, T.; Kleiner, I.; Kyuberis, A. A.; Loos, J.; Lyulin, O. M.; Massie, S. T.; Mikhailenko, S. N.; Moazzen-Ahmadi, N.; Müller, H. S. P.; Naumenko, O. V.; Nikitin, A. V.; Polyansky, O. L.; Rey, M.; Rotger, M.; Sharpe, S. W.; Sung, K.; Starikova, E.; Tashkun, S. A.; Auwera, J. Vander; Wagner, G.; Wilzewski, J.; Wcisło, P.; Yu, S.; Zak, E. J. The HITRAN2016 Molecular Spectroscopic Database. *J. Quant. Spectrosc. Radiat. Transf.* **2017**, *203*, 3–69. https://doi.org/10.1016/j.jqsrt.2017.06.038.

(31) Hill, C.; Gordon, I. E.; Kochanov, R. V.; Barrett, L.; Wilzewski, J. S.; Rothman, L. S. HITRANonline: An Online Interface and the Flexible Representation of Spectroscopic Data in the HITRAN Database. *J. Quant. Spectrosc. Radiat. Transf.* **2016**, *177*, 4–14. https://doi.org/10.1016/j.jqsrt.2015.12.012.

(32) Zare, R. N.; Herschbach, D. R. Doppler Line Shape of Atomic Fluorescence Excited by Molecular Photodissociation. *Proc. Ieee* **1963**, *51* (1), 173-+. https://doi.org/10.1109/proc.1963.1676.

(33) Troe, J. Theory of Thermal Unimolecular Reactions at Low Pressures. I. Solutions of the Master Equation. *J. Chem. Phys.* **1977**, *66* (11), 4745–4757. https://doi.org/10.1063/1.433837.

(34) Du, J.; Yuan, L.; Hsieh, S.; Lin, F.; Mullin, A. S. Dynamics of Weak and Strong Collisions: Highly Vibrationally Excited Pyrazine ($E = 37900$ cm^{-1}) with DCl†. *J. Phys. Chem. A* **2008**, *112* (39), 9396–9404. https://doi.org/10.1021/jp802421f.

(35) Jasper, A. W.; Oana, C. M.; Miller, J. A. "Third-Body" Collision Efficiencies for Combustion Modeling: Hydrocarbons in Atomic and Diatomic Baths. *Proc. Combust. Inst.* **2015**, *35* (1), 197–204. https://doi.org/10.1016/j.proci.2014.05.105.

(36) Hippler, H.; Troe, J.; Wendelken, H. J. Collisional Deactivation of Vibrationally Highly Excited Polyatomic Molecules. II. Direct Observations for Excited Toluene. *J. Chem. Phys.* **1983**, *78* (11), 6709–6717. https://doi.org/10.1063/1.444670.

(37) Elioff, M. S.; Sansom, R. L.; Mullin, A. S. Vibrational Energy Gain in the ν_2 Bending Mode of Water via Collisions with Ho Pyrazine ($E_{vib} = 37900$ cm^{-1}): Insights into the Dynamics of Energy Flow †. *J. Phys. Chem. A* **2000**, *104* (45), 10304–10311. https://doi.org/10.1021/jp001425a.

(38)   Johnson, J. A.; Duffin, A. M.; Hom, B. J.; Jackson, K. E.; Sevy, E. T. Quenching of Highly Vibrationally Excited Pyrimidine by Collisions with CO_2. *J. Chem. Phys.* **2008**, *128* (5). https://doi.org/10.1063/1.2825599.

(39)   Sałdyka, M.; Mielke, Z.; Haupa, K. Structural and Spectroscopic Characterization of DMF Complexes with Nitrogen, Carbon Dioxide, Ammonia and Water. Infrared Matrix Isolation and Theoretical Studies. *Spectrochim. Acta - Part A Mol. Biomol. Spectrosc.* **2018**, *190*, 423–432. https://doi.org/10.1016/j.saa.2017.09.046.

(40)   Wanna, J.; Menapace, J. A.; Bernstein, E. R. Hydrogen Bonded and Non-Hydrogen Bonded van Der Waals Clusters: Comparison between Clusters of Pyrazine, Pyrimidine, and Benzene with Various Solvents. *J. Chem. Phys.* **1986**, *85* (4), 1795–1805. https://doi.org/10.1063/1.451181.

(41)   Gosling, M. P.; Cockett, M. C. R. Hydrogen-Bonding in the Pyrimidine$\cdots NH_3$ van Der Waals Complex: Experiment and Theory. *Phys. Chem. Chem. Phys.* **2014**, *16* (27), 14195–14205. https://doi.org/10.1039/c4cp01472c.

(42)   Echebiri, G. O.; Smarte, M. D.; Walters, W. W.; Mullin, A. S. Performance of a High-Resolution Mid-IR Optical-Parametric-Oscillator Transient Absorption Spectrometer. *Opt. Express* **2014**, *22* (12), 14885. https://doi.org/10.1364/oe.22.014885.

(43)   Grigoleit, U.; Lenzer, T.; Luther, K.; Mützel, M.; Takahara, A. Collisional Energy Transfer of Highly Vibrationally Excited Toluene and Pyrazine: Transition Probabilities and Relaxation Pathways from KCSI Experiments and Trajectory Calculations. *Phys. Chem. Chem. Phys.* **2001**, *3* (12), 2191–2202. https://doi.org/10.1039/b100151p.

(44)   Hansen, E. W.; Gong, X.; Chen, Q. Compressed Exponential Response Function Arising From a Continuous Distribution of Gaussian Decays - Distribution Characteristics. *Macromol. Chem. Phys.* **2013**, *214* (7), 844–852. https://doi.org/10.1002/macp.201200715.

(45)   Elioff, M. S.; Wall, M. C.; Lemoff, A. S.; Mullin, A. S. Observation of an Energy Threshold for Large ΔE Collisional Relaxation of Highly Vibrationally Excited Pyrazine (E_{vib}= 31000 - 41000 cm^{-1}) by CO_2. *J. Chem. Phys.* **1999**, *110* (12), 5578–5588. https://doi.org/10.1063/1.478456.

(46)   Thompson, J. O. F.; Livingstone, R. A.; Townsend, D. Following the Relaxation Dynamics of Photoexcited Aniline in the 273-266 nm Region Using Time-Resolved Photoelectron Imaging. *J. Chem. Phys.* **2013**, *139* (3), 034316. https://doi.org/10.1063/1.4813005.

(47)   Abulimiti, B.; Zhu, R.; Long, J.; Xu, Y.; Liu, Y.; Ghazal, A. Y.; Yang, M.; Zhang, B. Study of Ultrafast Dynamics of 2-Picoline by Time-Resolved Photoelectron Imaging. *J. Chem. Phys.* **2011**, *134* (23), 234301. https://doi.org/10.1063/1.3600334.

(48)   Beyer, T.; Swinehart, D. F. Algorithm 448: Number of Multiply-Restricted Partitions. *Commun. ACM* **1973**, *16* (6), 379. https://doi.org/10.1145/362248.362275.

(49)   Masterson, A. L.; Farquhar, J.; Wing, B. A. Sulfur Mass-Independent Fractionation Patterns in the Broadband UV Photolysis of Sulfur Dioxide: Pressure and Third Body Effects. *Earth Planet. Sci. Lett.* **2011**, *306* (3–4), 253–260. https://doi.org/10.1016/j.epsl.2011.04.004.

(50)   Farquhar, J.; Peters, M.; Johnston, D. T.; Strauss, H.; Masterson, A.; Wiechert, U.;
       Kaufman, A. J. Isotopic Evidence for Mesoarchaean Anoxia and Changing
       Atmospheric Sulphur Chemistry. *Nature* **2007**, *449* (7163), 706-U5.
       https://doi.org/10.1038/nature06202.

(51)   Farquhar, J.; Savarino, J.; Airieau, S.; Thiemens, M. H. Observation of
       Wavelength-Sensitive Mass-Independent Sulfur Isotope Effects during SO_2
       Photolysis: Implications for the Early Atmosphere. *J. Geophys. Res. E Planets*
       2001, *106* (E12), 32829–32839. https://doi.org/10.1029/2000JE001437.

(52)   Lyons, J. R. Mass-Independent Fractionation of Sulfur Isotopes by Isotope-
       Selective Photodissociation of SO_2. *Geophys. Res. Lett.* **2007**, *34* (22), L22811.
       https://doi.org/10.1029/2007GL031031.

(53)   Lyons, J. R. Chapter 5 Photolysis of Long-Lived Predissociative Molecules as a
       Source of Mass-Independent Isotope Fractionation: The Example of SO_2.
       Advances in Quantum Chemistry. Academic Press January 1, 2008, pp 57–74.
       https://doi.org/10.1016/S0065-3276(07)00205-5.

(54)   Ono, S.; Whitehill, A. R.; Lyons, J. R. Contribution of Isotopologue Self-Shielding
       to Sulfur Mass-Independent Fractionation during Sulfur Dioxide Photolysis. *J.
       Geophys. Res. Atmos.* **2013**, *118* (5), 2444–2454.
       https://doi.org/10.1002/jgrd.50183.

(55)   Brand, J. C. D.; Chiu, P. H.; Hoy, A. R.; Bist, H. D. Sulfur-Dioxide - Rotational
       Constants and Asymmetric Structure of C̃-$^1B_2$ State. *J. Mol. Spectrosc.* **1976**, *60*
       (1–3), 43–56. https://doi.org/10.1016/0022-2852(76)90114-4.

(56)   Okabe, H. Fluorescence and Predissociation of Sulfur Dioxide. *J. Am. Chem. Soc.*
       1971, *93* (25), 7095-. https://doi.org/10.1021/ja00754a072.

(57)   Cosofret, B. R.; Dylewski, S. M.; Houston, P. L. Changes in the Vibrational
       Population of $SO(^3\Sigma^-)$ from the Photodissociation of $SO2$ between 202 and 207
       Nm. *J. Phys. Chem. A* **2000**, *104* (45), 10240–10246.
       https://doi.org/10.1021/jp001276w.

(58)   Kanamori, H.; Butler, J. E.; Kawaguchi, K.; Yamada, C.; Hirota, E. Spin
       Polarization in so Photochemically Generated from SO_2. *J. Chem. Phys.* **1985**, *83*
       (2), 611–615. https://doi.org/10.1063/1.449528.

(59)   Felder, P.; Effenhauser, C. S.; Haas, B. M.; Huber, J. R. Photodissociation of
       Sulfur Dioxide at 193 nm. *Chem. Phys. Lett.* **1988**, *148* (5), 417–422.
       https://doi.org/10.1016/0009-2614(88)87198-7.

(60)   Ma, J. Q.; Wilhelm, M. J.; Smith, J. M.; Dai, H. L. Photolysis (193 nm) of SO_2:
       Nascent Product Energy Distribution Examined through IR Emission. *J. Phys.
       Chem. A* **2012**, *116* (1), 166–173. https://doi.org/10.1021/jp2061943.

(61)   Huang, Y. L.; Gordon, R. J. The Multiplet State Distribution of $O(^3P_J)$ Produced in
       the 193 nm Photodissociation of SO_2. *The Journal of Chemical Physics*. American
       Institute of Physics July 4, 1990, pp 868–869. https://doi.org/10.1063/1.459462.

(62)   Brouard, M.; Cireasa, R.; Clark, A. P.; Preston, T. J.; Vallance, C.; Groenenboorn,
       G. C.; Vasyutinskii, O. S. $O(^3P_J)$ Alignment from the Photodissociation of SO_2 at
       193 nm. *J. Phys. Chem. A* **2004**, *108* (39), 7965–7976.
       https://doi.org/10.1021/jp049328v.

(63)   Kłos, J.; Alexander, M. H. *Preliminary Potential Energy Curves of SO_2
       Photodissociation*; 2020.

(64)   Hui, M. H.; Rice, S. A. Decay of Fluorescence from Single Vibronic States of SO_2. *Chem. Phys. Lett.* **1972**, *17* (4), 474–478. https://doi.org/10.1016/0009-2614(72)85083-8.

(65)   Katagiri, H.; Sako, T.; Hishikawa, A.; Yazaki, T.; Onda, K.; Yamanouchi, K.; Yoshino, K. Experimental and Theoretical Exploration of Photodissociation of SO_2 via the $(\tilde{C})^1B_2$ State: Identification of the Dissociation Pathway. *J. Mol. Struct.* **1997**, *413*, 589–614. https://doi.org/10.1016/s0022-2860(97)00199-3.

(66)   Freedman, A.; Yang, S. C.; Bersohn, R. Translational Energy Distribution of the Photofragments of SO_2 at 193 nm. *J. Chem. Phys.* **1979**, *70* (11), 5313–5314. https://doi.org/10.1063/1.437327.

(67)   Kawasaki, M.; Sato, H. Photodissociation of Molecular-Beams of SO_2 at 193 nm. *Chem. Phys. Lett.* **1987**, *139* (6), 585–588. https://doi.org/10.1016/0009-2614(87)87347-5.

(68)   Ray, P. C.; Arendt, M. F.; Butler, L. J. Resonance Emission Spectroscopy of Predissociating SO_2 $(\tilde{C})(^1B_2)$: Coupling with a Repulsive $^1A_1$ State near 200 nm. *J. Chem. Phys.* **1998**, *109* (13), 5221–5230. https://doi.org/10.1063/1.477139.

(69)   Schinke, R. *Photodissociation Dynamics : Spectroscopy and Fragmentation of Small Polyatomic Molecules*; Cambridge University Press, 1993.

(70)   Burkholder, J. B.; Lovejoy, E. R.; Hammer, P. D.; Howard, C. J.; Mizushima, M. High-Resolution Infrared Fourier-Transform Spectroscopy of SO in the $X^3\Sigma^-$ and $A_1\Delta$ Electronic States. *J. Mol. Spectrosc.* **1987**, *124* (2), 379–392. https://doi.org/10.1016/0022-2852(87)90148-2.

(71)   Becker, S.; Braatz, C.; Lindner, J.; Tiemann, E. Investigation of the Predissociation of SO_2 - State-Selective Detection of the SO-Fragment and O-Fragment. *Chem. Phys.* **1995**, *196* (1–2), 275–291. https://doi.org/10.1016/0301-0104(95)00114-4.

(72)   Moore, C. E. *CRC Series in Evaluated Data in Atomic Physics*; Gallagher, J. W., Ed.; CRC Press, 1993.

(73)   Greene, C. H.; Zare, R. N. Photofragment Alignment and Orientation. *Annu. Rev. Phys. Chem.* **1982**, *33* (1), 119–150. https://doi.org/10.1146/annurev.pc.33.100182.001003.

(74)   Kinsey, J. L. Fourier Transform Doppler Spectroscopy: A New Means of Obtaining Velocity-angle Distributions in Scattering Experiments. *J. Chem. Phys.* **1977**, *66* (6), 2560–2565. https://doi.org/10.1063/1.434252.

(75)   Nadler, I.; Mahgerefteh, D.; Reisler, H.; Wittig, C. The 266 Nm Photolysis of ICN- Recoil Velocity Anisotropies And Nascent E,V,R,T Excitations For The CN + I($^2P_{3/2}$) And CN + I($^2P_{1/2}$) Channels. *J. Chem. Phys.* **1985**, *82* (9), 3885–3893. https://doi.org/10.1063/1.448879.

(76)   Abu-Bajeh, M.; Cameron, M.; Jung, K. H.; Kappel, C.; Lauter, A.; Lee, K. S.; Upadhyaya, H. P.; Vatsa, R. K.; Volpp, H. R. Absolute Quantum Yield Measurements for the Formation of Oxygen Atoms after UV Laser Excitation of SO_2 at 222.4 nm. *Proc. Indian Acad. Sci. Sci.* **2002**, *114* (6), 675–686.

(77)   Atkins, P. W. (Peter W.; De Paula, J. *Physical Chemistry*, 9th Editio.; 2009.

(78)   Patel, D.; Margolese, D.; Dyke, T. R. Electric Dipole Moment of SO_2 in Ground and Excited Vibrational States. *J. Chem. Phys.* **1979**, *70* (6), 2740–2747. https://doi.org/10.1063/1.437860.

(79) Amano, T.; Hirota, E.; Morino, Y. Microwave Spectrum of the SO Radical. Equilibrium S-O Distance, Electric Quadrupole Coupling Constant and Magnetic Hyperfine Structure Constants. *J. Phys. Soc. Japan* **1967**, *22* (2), 399–412. https://doi.org/10.1143/jpsj.22.399.

(80) Powell, F. X.; Lide, D. R. Microwave Spectrum of the SO Radical. *J. Chem. Phys.* **1964**, *41* (5), 1413–1419. https://doi.org/10.1063/1.1726082.

(81) Liu, Q.; Havey, D. K.; Li, Z.; Mullin, A. S. Effects of Alkylation on Deviations from Lennard−Jones Collision Rates for Highly Excited Aromatic Molecules: Collisions of Methylated Pyridines with HOD [†]. *J. Phys. Chem. A* **2009**, *113* (16), 4387–4396. https://doi.org/10.1021/jp811077p.

(82) Durana, J. F.; McDonald, J. D. Infrared Chemiluminescence Studies of Chlorine Substitution Reactions with Brominated Unsaturated Hydrocarbons. *J. Chem. Phys.* **1976**, *64* (6), 2518–2527. https://doi.org/10.1063/1.432501.